NTNU
Norwegian University of
Science and Technology

# Mechanical Properties after Welding and Post Weld Heat Treatment of a 6082 Aluminium Alloy

**Sondre Borg Gjertsen**

Materials Technology (MIMT)
Submission date: June 2018
Supervisor: Trond Furu, IMA
Co-supervisor: Ole Runar Myhr, Hydro / IKT (NTNU)

Norwegian University of Science and Technology
Department of Materials Science and Engineering

NTNU

Norwegian University of
Science and Technology

# ABSTRACT

Lightweight materials are currently gaining popularity and are sought for by the construction and transportation industries. The heat-treatable 6xxxx series aluminium alloys are popular in lightweight products by combining good formability in the solution treated and natural aged state (T4) and high in-service strength in the artificial aged temper (T6). Arc welding is an industrial technique used for joining aluminium structures, but welded joints of the 6xxx-series lose a significant percentage of their strength in the heat affected zone (HAZ).

The aim of this study has been to improve the strength for a welded component by manipulating the HAZ geometry with a laser. The idea of manipulating the HAZ geometry is to generate a more complex geometric shape of the HAZ in order to increase the global strength of the welded component. The potential of applying post weld laser heat treatment if successful is large since the softest part of a weldment of EN AW-6082-T6 is the HAZ. Increasing the strength and understanding the limitations of the HAZ are important to minimize weight for new structural designs.

In the process a laser heat distribution has been studied and a heat distribution model based on the "*Medium thick plate solution"* after Rosenthal [1] is created. The model is used to study efficiency factor ($\eta$) and the impact of changing laser parameters to establish optimal parameters. The laser treatment has been conducted on an extruded profile of EN AW-6082-T6, which have been welded with metal inert gas (MIG) welding. A test setup is established where four specimens have been laser heat treated, tested and compared to an untreated specimen. Cross-weld tensile testing, hardness measurements and microscopy of the weld have been performed, analysed and reported in this thesis. The strength has not been increased by the laser treatment conducted in thesis as the parameters used created locally too high temperature. However, ductility and fracture resistance have been improved. A set of laser parameters which is anticipated to generate a positive laser heat treatment have been generated.

# SAMMENDRAG

Populariteten til lettvekts materialer er for tiden økende og de er etterspurte av transport og byggebransjen. De utherdbare aluminiumslegeringene i 6xxx-serien er populære for produkter med lav vekt ved å kombinere god formbarhet i innherdet og kaldutherdet tilstand (T4) med muligheten til å øke styrken etterpå i varmutherdet tilstand (T6). Buesveising er en industrialisert teknikk som brukes for sammenføyning av strukturer i aluminium, men sveisede sammenføyninger i 6xxx-serien taper en betydelig prosentandel av styrken i varmepåvirket sone (HAZ).

Denne oppgaven har som mål å forbedre styrken til en sveiset komponent ved å bruke laser til manipulasjon av geometrien til HAZ. Ideen bak å manipulere geometrien til HAZ er å introdusere en mer komplisert form på HAZ for å øke den sveisede komponentens globale styrke. Potensialet av å ta i bruk en slik teknikk etter sveising er stort ettersom HAZ er den svakeste sonen på en sveis av EN AW-6082-T6. Økt styrke i HAZ og forståelse av begrensningene her er viktig for å unngå overdimensjonering for nye design av strukturer i aluminium. Dette vil være positivt med hensyn til å utvikle og produsere kjøretøy og konstruksjoner hvor lav vekt er viktig.

Experimentell testing med termoelementer er blitt utført og en modell, basert på Rosenthal's «Medium thick plate solution», er blitt brukt til å identifisere laserens termiske forløp. Laserbehandling er blitt gjort på en ekstrudert profil av type EN AW-6082-T6, som er blitt sveiset med metall inertgass (MIG) sveising. Et oppsett bestående av fire prøver med påført laserbehandling er testet og sammenlignet med en ubehandlet prøve. Strekktesting på tvers av sveisen, hardhetsmålinger og mikroskopi av sveiseprøvene er blitt utført, analysert og rapportert i denne avhandlingen. Laserbehandling gjennomført i denne oppgaven har ikke gitt økt styrke da det lokalt er tilført for stor varme, men duktilitet og motstanden mot brudd er forbedret. Det er etablert laser parametere som forventes å kunne medføre positiv effekt av laser varmebehandling i HAZ.

# PREFACE

This master thesis has been compiled as the final stage of the 2 years master's degree program in Materials Technology at the Norwegian University of Science and Technology (NTNU). It has been a part of a collaboration between NTNU, Norsk Hydro, SINTEF Raufoss manufacturing, IFE and the new NAPIC center. The work was carried out the spring of 2018 at the Department of Materials Science and Engineering at NTNU.

Sondre Borg Gjertsen

Trondheim, June 2018

# ACKNOWLEDGMENTS

I would like to extend my gratitude to supervisor Dr. Trond Furu[1] and co-supervisor Dr. Ole Runar Myhr[2] for their encouragement and guidance throughout this study. My trips to SINTEF Raufoss Manufacturing has been very appreciated. I am very grateful for the technical guidance and support provided by Senior Research Scientist Rune Østhus[3]. Thanks to Nordic Additive Manufacturing for letting me use their laser for my study.

Furthermore, Morten Høgseth Danielsen[4] deserve a big gratitude for guidance and sharing his expertise on welding. I would like to thank Engineer Tore Andre Kristensen[4] for his help with tensile testing and post processing with digital image correlation (DIC).

Finally, I would like to thank Chief Engineer Pål Skaret[5] and Senior Engineer Trygve Schanche[5] for their guidance and for their attitude towards helping me and other students in every possible situation encountered at NTNU's workshops and laboratories.

---

[1] Norsk Hydro, Sunndalsøra

[2] Norsk Hydro, Raufoss

[3] SINTEF Raufoss Manufacturing

[4] SINTEF Materials and Chemistry

[5] NTNU, Trondheim.

# TABLE OF CONTENT

---

# ABBREVIATIONS

$\beta$ - Equilibrium phase (Mg2Si)

$\beta'$ - Hardening precipitate in AlMgSi alloys (semi-coherent rods)

$\beta''$ - Hardening precipitate in AlMgSi alloys (semi-coherent needles)

$\eta$ - Heat source efficiency factor

$\phi$ - Laser spot size

$A_{gt}$ - The elongation at maximum stress

Al - Aluminium

Al-Mg-Si - Aluminium-Magnesium-Silicon

BM - Base metal

$b_{HAZ}$ - Extent of heat affected zone

Cr - Chromium

DIC - Digital image correlation

GP-zones - Meta-stable Guinier–Preston zones prior to precipitation of $\beta''$

HAZ - Heat affected zone

I - Welding current

IFE - Institute of Energy Technology

Mg - Magnesium

MIG - Metal inert gas

Mn - Manganese

NTNU - Norwegian University of Science and Technology

P - Load-bearing capacity

$P_{max}$ - Maximum pressure during extrusion

PWHT - Post weld heat treatment

$R_{p0,2}$ - Engineering yield stress

$R_m$ - Engineering ultimate tensile stress

$R_{min}$ - Minimum engineering yield stress

RT - Room temperature

Sc - Scandium

SEM - Scanning electron microscope

Si - Silicon

SSSS - Supersaturated solid solution

$T_0$ - Initial body temperature

$T_{Billet}$ - Billet temperature in billet loader

$T_{eq}$ - Temperature of equilibrium solvus

$T_{max}$ - Peak temperature of the thermal cycle

T4 - Alloy solution-treated and naturally aged at room temperature

T6 - Alloy solution-treated and artificially aged to peak strength

TIG - Tungsten inert gas

THTB - Tailored Heat-Treated Blanks

TM - Transition metals

PWHT - Post weld heat treatment

U - Welding voltage

$U_T$ - Toughness

v - heat source moving speed

$v_{avg}$ - Average ram speed (extrusion)

$v_{max}$ - Maximum ram speed (extrusion)

Zr - zirconium

# 1 INTRODUCTION

Aluminium structures of the 6xxx-series experience severe softening by welding in the zone called heat affected zone (HAZ) [2, 3]. The 6xxx-series is also called aluminium-magnesium-silicon (Al-Mg-Si) alloys. These alloys obtain desirable properties for use in low weight structures used for transportation and constructions. Due to precipitation of very small needle shaped β''($Mg_5Si_6$) particles, the alloys may obtain tensile strength up to 350 MPa in artificial aged (T6) condition [2]. High strength combined with low density and good corrosion resistance makes Al-Mg-Si alloys attractive for structural components in a marked with increasing focus on light weight products.

Fusion welding is widely used for assembling structures by aluminium [4]. The thermal cycle of the fusion welding process influences the age hardening of an Al-Mg-Si alloy, resulting in deterioration of mechanical properties in the HAZ [2]. The design standard Eurocode 9 [5] states that for EN AW-6082-T6 extruded profiles a reduction factor of 0.60 to 0.66 for tensile strength should be applied to the deteriorated HAZ compared to unwelded material. Hence, aluminium designs are built with increased dimension. These local reduction factors are considered too conservative, but they are frequently applied for the whole structure in the design process likely resulting in a significant weight penalty.

When welding Al-Mg-Si alloys, HAZ is the weakest zone of the weldment. Hence, fracture will most likely occur in this area during tensile testing. Welding strings are often deployed in straight lines in conventional welding, leaving a HAZ parallel to the weld stretching until 35 mm out from the weld [5]. Finite element modelling has found that the linear transition line between unaffected base material and the HAZ may not be optimal for tensile strength. A more complex geometry of the HAZ could have the potential to increase global strength of a welded component [6].

## OBJECTIVE OF THESIS

Improving the knowledge and tools to predict strength in aluminium weldments is important to develop optimisation of both weld and HAZ design to maximize mechanical properties of welded structures of Al-Mg-Si alloys. The overall aim of this thesis has been to develop a method for strengthening a welded EN AW-6082 aluminium alloy with post weld heat treatment (PWHT). A concept study has indicated that manipulating the HAZ geometry may improve strength. This has been the basis for this thesis, and a laser has been used for PWHT.

# 2 THEORETICAL BACKGROUND

This chapter provides a brief introduction to properties and typical production route for the 6xxx-series aluminium alloys. In addition, a background on fusion welding with focus on metal inert gas (MIG) welding, which is used in this thesis, has been given. Weakening mechanisms by welding for the 6xxx-series is explained. A brief presentation of the concept study conducted by Fjær [6], about increased strength for a bulged HAZ compared to straight HAZ, has been given as well.

## 2.1 ALUMINIUM ALLOYS

Aluminium alloys are divided into two major categories; wrought products and casted products. Both main categories have two subcategories; heat treatable alloys and non-heat treatable alloys. These again obtain series classifying their major alloying elements. An overview is given in Table 2-1 [7, 8].

*Table 2-1: Overview of the dividing of the aluminium alloys in categories and series [7, 8].*

| | | | |
|---|---|---|---|
| **Aluminium alloys** | Wrought products | Heat treatable | 2xxx, 4xxx, 6xxx, 7xxx, 8xxx |
| | | Non-heat treatable | 1xxx, 3xxx, 4xxx, 5xxx, 8xxx |
| | Casted products | Heat treatable | 2xx.x, 3xx.x, 7xx.x |
| | | Non-heat treatable | 1xx.x, 4xx.x, 5xx.x, 8xx.x |

### 2.1.1 6xxx-series aluminium alloys

Alloys of the 6xxx-series are called Al-Mg-Si alloys due to the major alloying elements, which are silicon (Si) and magnesium (Mg). The 6xxx-series is widely used in constructions, shipbuilding, aerospace and the automotive industry [9]. These alloys provide an excellent combination of high strength-to-weight ratio, good weldability, ductility and corrosion resistivity. Due to aluminium's low density, the weight efficiency will be good in many designs compared to other competing construction metals. Lightweight structures are sought after in the transportation industry, for example to reduce fuel consumption [10]. Typical applications of the 6xxx-series are illustrated in Figure 2-1.

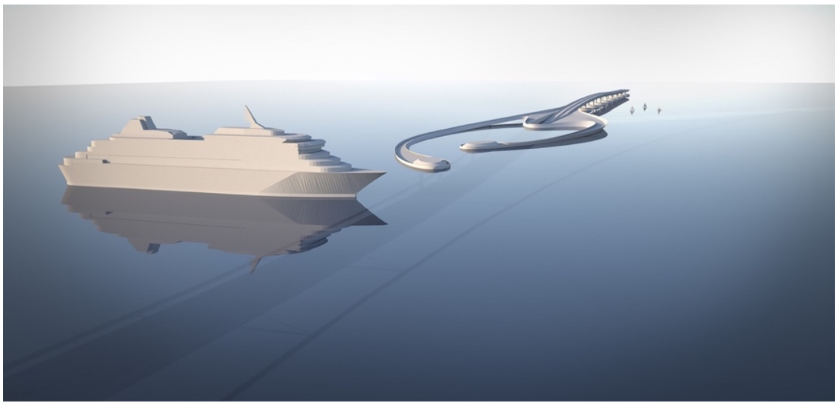

*Figure 2-1: Transport and construction structures are typical applications of the 6xxx-series aluminium alloys [11].*

Good ductility and low melting point are important properties in manufacturing of the 6xxx-series [10]. Components of the 6xxx-series may be formed by extrusion and stamping [8]. The structural properties of finished products are highly dependent of the thermomechanical treatment, which are further explained in the following sections of this chapter. A typical heat treatment timeline of the production process for 6xxx-series components is presented in Figure 2-2.

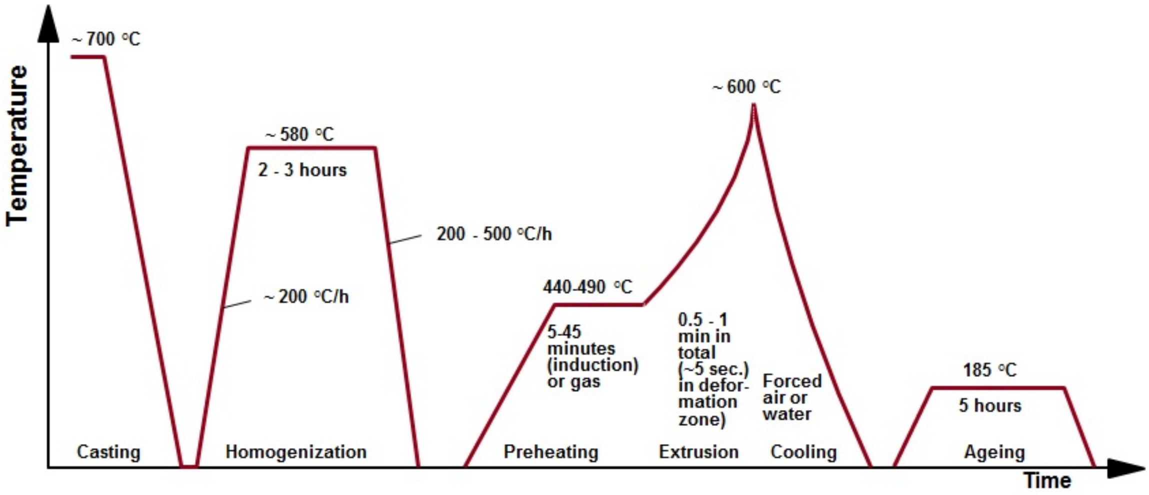

*Figure 2-2: Typical thermal history of the production route of the 6xxx-series [12].*

### 2.1.2 Solution heat treatment

The thermomechanical history begins with alloy design and casting of billets [8]. After casting, the billets are given a solution heat treatment called homogenization. This is conducted at temperatures above the equilibrium solvus, $T_{eq}$, of the major alloying elements and other heterogeneous phases to dissolve them into the aluminium (Al) matrix. The temperature interval range between 450-580°C for Al-Mg-Si alloys [13]. The process is driven by the free energy change of transformation [3, 14]. Figure 2-3 presents the equilibrium phase diagram of Al-$Mg_2Si$, showing temperature as a function of solubility of $Mg_2Si$ in Al. In addition, intermetallic phases containing iron needs to be controlled as they may form crack propagating particles and reduce the forming limits of the material. Spheriodizing insoluble phase particles is another important function of the homogenization process [15, 16].

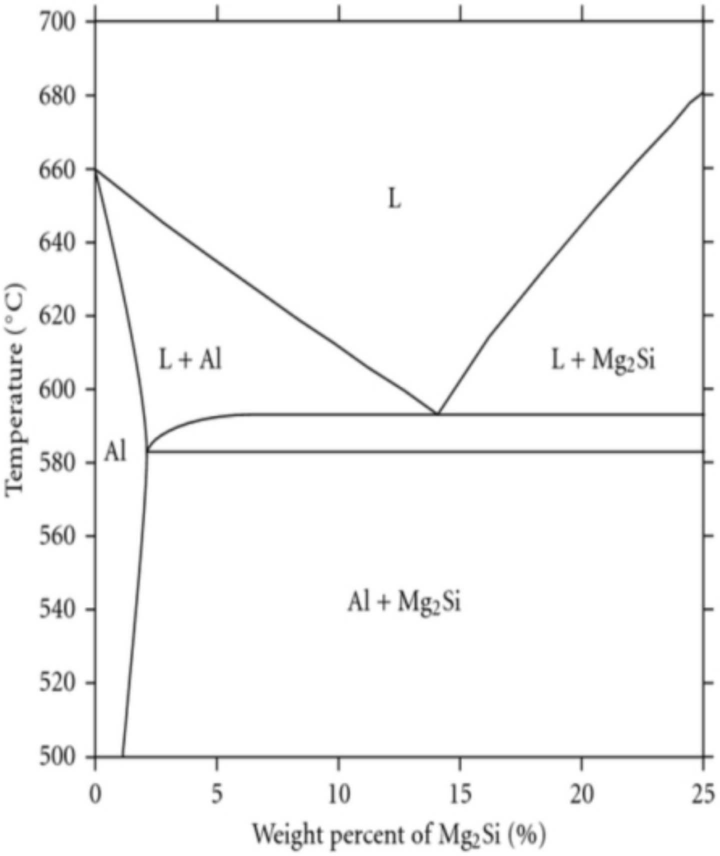

*Figure 2-3: Phase diagram showing the solubility of $Mg_2Si$ in aluminium as a function of temperature [17].*

The homogenization is followed by rapid cooling to obtain supersaturated solid solution (SSSS). The diffusion of solute alloying elements decrease or ”freeze” at room temperature (RT). Although they are over the equilibrium concentrations, the concentrations of Mg and Si will remain solute in the Al matrix [14]. The cooling stage should be rapid. If quenched, the flow stress of the material is raised, which may affect further processing. A controlled cooling rate of 300-500°C/h is considered sufficient [13]. Adequate solution treatment and quenching is vital for strength in any precipitation-hardening system. In general, prolonged homogenization times, increased temperature and accelerated quenching rates all result in better age-hardening [18].

### 2.1.3 Extrusion and dispersoids

Heat-treatable aluminium alloys are suited for lightweight structures. They provide the combination of good formability in T4 state and high in-service strength in T6. Aluminium has the ability to be extruded into open and closed profiles with intricate shapes and change in wall thickness [10]. Extrusion offers a relatively cheap method for producing complex shapes in long lengths, and the 6xxx-series has good geometric tolerances [12]. Finite element modelling enables weight optimizations which favours aluminium structures as these are highly formable. High stress areas can be avoided by expansion in the design and the centre of gravity can be positioned precisely in the axes of the stress to avoid eccentric loading. The 6xxx-series is dominating in the marked for extruded profiles.

Extrusion impacts the material's mechanical properties due to the change in microstructure. When the aluminium billets are forced through a die, the material deforms to match the geometry of the die's cross section while grains deform and stretch out. The metal's microstructure consists of elongated fibrous grains directly after the extrusion. An in-situ extrusion process is imaged in Figure 2-4. Due to the large pressure required for extrusion, most metals are extruded in heated condition to decrease the material's deformation resistance [19].

The extrudability of the 6xxx-series and microstructural changes by extrusion is related to the alloy composition. The solidus temperature decreases and the deformation resistance increases with increasing Mg and Si contents [12].

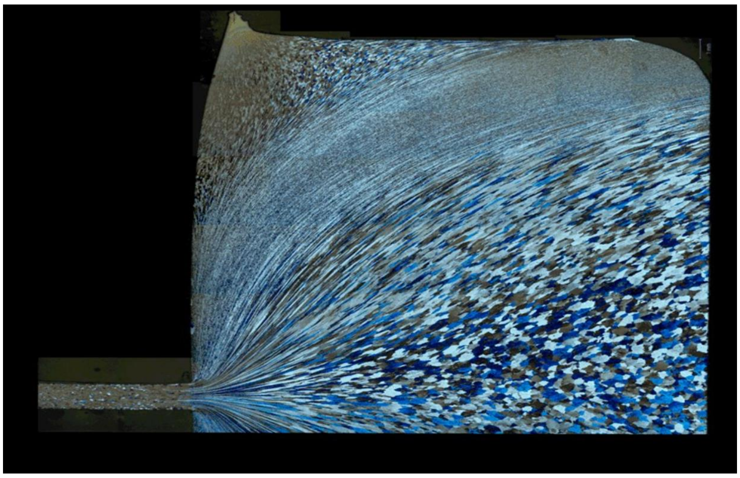

*Figure 2-4: In-situ microstructure of aluminium during extrusion. (Printed with permission from Dr. Trond Furu.)*

The deformation of the billet is relatively uniform until the entrance of the die. When the friction increases due to pressing against the container-wall, a dead zone of stagnant metal is produced. At the surface layer of the extrusion, the billet undergoes extensive shear deformation compared to the center, which is essentially pure elongation. The high friction together with the high temperatures obtained during the extrusion is a suiting environment for recrystallization of the deformed grain structure [19]. Recrystallization is thermodynamically activated, but a non-recrystallized microstructure is favourable as metal's mechanical properties are impacted by grain size. A too large grain size may be undesirable related to strength and ductility or other functional deficiencies such as orange peel. Controlling the grain size and texture represents quality control in sheet production [20].

Precipitates which have a rather limited direct effect on the mechanical properties are usually referred to as dispersoids [16]. Dispersoids prevent recrystallization and are favourable in a number of semi-products after heat treatment such as extrusion, aging and welding. The recrystallization is retarded by the particles due to pinning of the moving reaction front. The time spent at elevated temperatures after extrusion has an influence on the recrystallization, and water quenching gives a considerable thinner recrystallization surface layer compared to air-cooling [16].

Elements like manganese (Mn) and chromium (Cr) contribute to form different types of dispersoids at high temperatures (400 – 550°C) [16] and are often added to the alloy to reduce recrystallization. Due to their fairly high density and high thermal stability, the dispersoids may have a strong effect on the recovery, recrystallization, grain growth processes and may even act as nucleation sites for the precipitation of the strengthening precipitates [16]. The effect on recrystallization by increasing the Mn concentration in an AA6082 aluminium alloy are presented in Figure 2-5, where (a) have low Mn content and (b) have high Mn content. Other 3d transition metals (TM) like scandium (Sc) and zirconium (Zr) are also found to have a profound influence on preventing recrystallization, as seen in Figure 2-6.

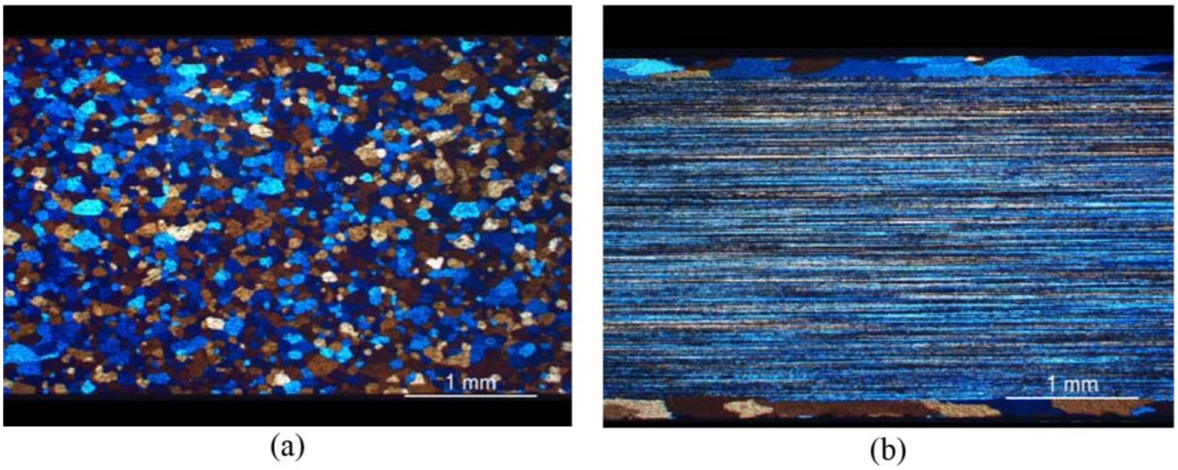

*Figure 2-5:Micrographs of the grain structure of AA6082 alloys with different Mn content. (a) 0,006 wt% Mn and (b) 1,172 wt% Mn. The degree of recrystallization decreases with increasing amount of Mn. [21]*

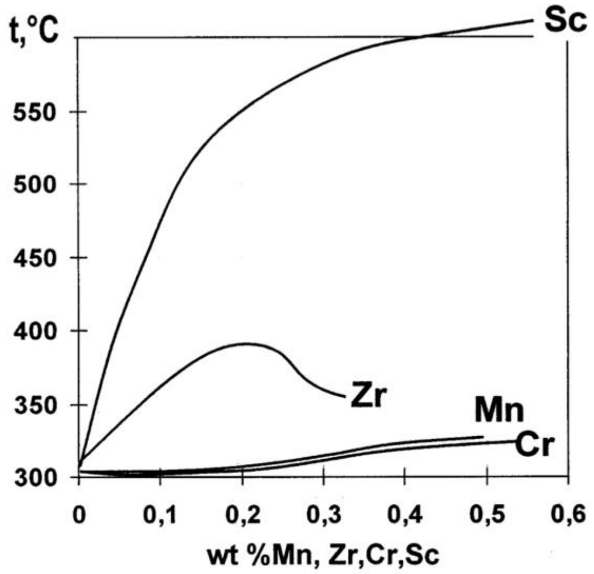

*Figure 2-6: A recrystallization temperature (50% recrystallization) of cold-rolled binary Al–TM alloy sheets vs. content of transition metals [22].*

### 2.1.4 Precipitation hardening

The most important hardening effect of the 6xxx-series is precipitation hardening. An impressive in-service strength is possible to obtain by treating an alloy of the 6xxx-series with homogenization (solution treatment) and quenching followed by artificial aging (precipitation). The Mg and Si atoms in SSSS gives the potential for precipitation of the $\beta$ phase ($Mg_2Si$). The generic precipitation sequence for metastable phases of the ternary Al-Mg-Si alloys is well known in literature [23, 24], and is presented here:

$$\boldsymbol{SSSS \rightarrow Solute\ cluster \rightarrow GP\ zones \rightarrow \beta'' \rightarrow \beta' \rightarrow \beta}\ (\boldsymbol{stable})$$

Guinier–Preston (GP) zones are an early stage phenomenon of the precipitation sequence. The different phases are described with formula in Table 2-2.

*Table 2-2: Precipitate composition and size [24, 25].*

| Phase | Formula | Shape | Size | Crystal system |
|---|---|---|---|---|
| **GP zones** | Si/Mg>1 | Semi-coherent needles | 1-2 nm | Unknown |
| $\boldsymbol{\beta''}$ | $Mg_5Si_6$ | Semi-coherent Needles | Up to 40*40*350 Å | Monoclinic |
| $\boldsymbol{\beta'}$ | $Mg_{1.7}Si$ | Semi-coherent Ribbons | Several µm long | Hexagonal |
| $\boldsymbol{\beta}$ | $Mg_2Si$ | Plates or cubes | 10-20 µm | Hexagonal |

Alloying elements in solid solution increase the materials strength by imposing an elastic stress field on the matrix, as illustrated in Figure 2-7 (A). Further strengthening and tensile strength values higher than 350 MPa is possible owing to growth and precipitation of fine needle shaped $\beta''$-particles along the <100> directions from clusters in the aluminium matrix [2]. The $\beta''$-precipitates are semi-coherent to the aluminium lattice and impose elastic stress fields which retard dislocation movements. For dislocation movements to propagate in the material, they must either bypass, illustrated in Figure 2-7 (B), or cutting through the precipitates, illustrated in Figure 2-7 (C).

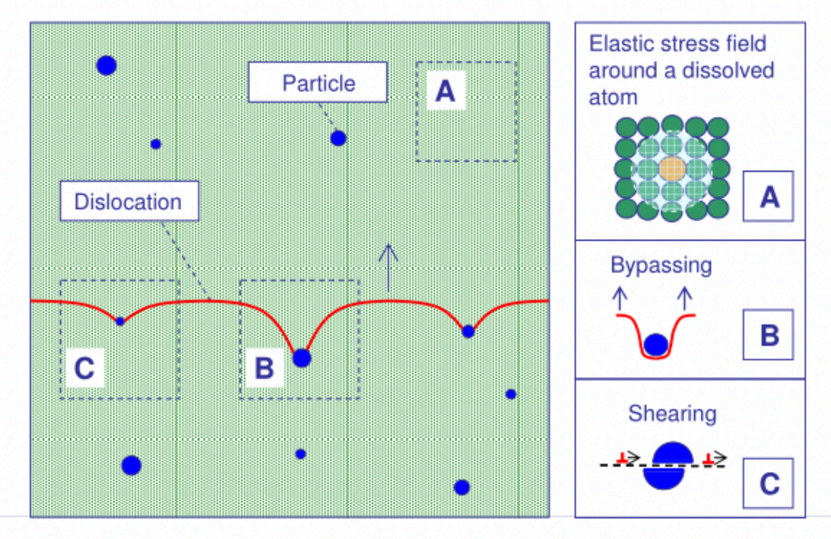

*Figure 2-7: Contributions from dissolved alloying elements in solid solution (A) and particles from precipitation hardening (B, C). Dislocations may either move through bypassing (B) of larger particles or shearing in the case of smaller particles (C) [26].*

The saturated material will gain some strength as the clusters of Mg and Si grow during prolonged storage at RT after solution treatment. The diffusion processes which are responsible for growth of clusters is slow at RT. Hence, the strength level saturates within a couple of days. The process of strengthening materials by precipitation at RT is called natural aging, and natural aged aluminium alloys are labelled T4. However, if the temperature is raised to 150 - 200°C, the kinetics become faster and a high fraction of small hardening $\beta''$-precipitates forms, causing a continuous increase in the strength level until the peak of the hardness curve is reached [27]. This process is called artificial aging. Materials that are artificially aged to peak strength and hardness is labelled T6. If the artificial aging process is held too long, the $\beta''$ precipitates will coarsen and lose coherency to the aluminium matrix. The coarsening is driven by the surface energy, where larger particles are thermodynamically more favourable than smaller particles [3]. The precipitates will then become $\beta'$ phase, which has a decreased hardening effect in the alloy. This mechanism is also activated in welding, and it has been further explained later in Chapter 2.3. At this point the alloy is overaged and the strength and hardness of the alloy will continuously decrease until a new solution treatment is given. The strengthening effect of the different precipitates are dependent on their resistance to dislocation movements.

## 2.2 WELDING OF THE 6XXX-SERIES

Major developments in manufacturing of aluminium components has been seen over the recent years, which have been strongly driven by the automobile industry [12]. Nevertheless, assembling has and will be more or less inevitable in many years to come for industrial purposes. Arc welding is an industrialized assembling process developed for metal joining. In the commercial vehicle and construction industry, tungsten inert gas (TIG)- and metal inert gas (MIG) arc welding are the most widely used processes.

Arc welding has been developed with focus on steel. It is important to understand and account for the differences in physical, chemical and mechanical properties between aluminium and steel when welding Al [28]. The well anchored oxide layer of aluminium develops in an atmosphere containing oxygen and is very positive with respect to corrosion resistance. In welding additional energy is required to burn through the oxide layer and melt the underlaying material. Aluminium oxide's melting point is 2060 °C. Compared to steel, the required energy for Al welding is much the same, despite that Al melts at much lower temperatures. Al-Mg-Si alloys has a melting interval of 570 - 660°C. The thermal conductivity of aluminium is sex times higher than to steel. To weld Al is also more complicated with respect to cracking, buckling and distortion due to its coefficient of thermal expansion, which is approximately twice of steel's [28].

For age hardening materials, the weld thermal cycle will degrade the mechanical properties of the unmelted metal in proximity to the weld. This area is called the heat affected zone (HAZ). To overcome the problem of deterioration in the HAZ, other techniques such as plasma-, laser-, resistance- or friction stir welding have been developed with promising results for aluminium joining. Until now they have been little used for industrial applications. Definitions of different features in MIG butt-welding are presented in Figure 2-8.

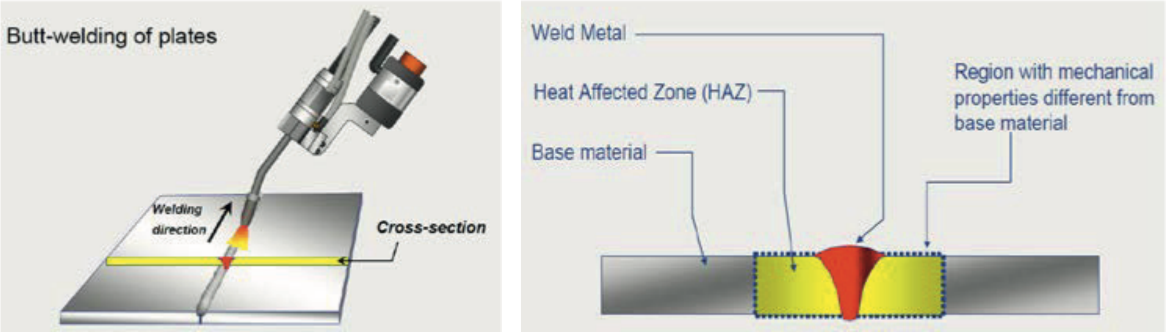

(a) (b)

*Figure 2-8: MIG welding of aluminium (a) butt-welded plates and (b) the Heat Affected Zones (HAZ) [29].*

### 2.2.1 MIG Welding

In MIG welding, two pieces of metal are joined by a continuously fed filler wire and the heat from the welding arc [30]. A filler wire of the 5xxx-series (frequently AA5183) with a high content of Mg is often used For MIG welding of the 6xxx-series. The arc ignites when the filler wire and work piece are connected by a closed circuit. An illustration of a MIG welding gun setup is presented in Figure 2-9. The circuit is made with reverse polarity in aluminium welding to ensures removal of the oxide film and the melting of the wire electrode at the same time [28]. The filler metal, arc and weld pool are protected by an inert gas shield, usually argon. MIG welding provides all positional welding capability, high welding speeds, excellent oxide film removal and smaller heat affected zones compared to TIG welding [28].

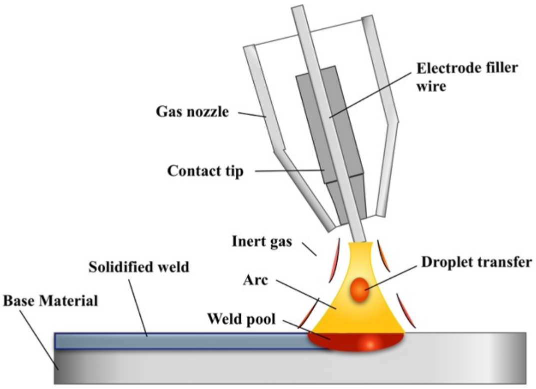

*Figure 2-9: Illustration of metal inert gas welding process [29].*

### 2.2.2 The weld thermal cycle

Products of the 6xxx-series in T6 condition are made from a meticulous metallurgical process. The weld thermal cycle is essential for the physical processes occurring during and after the welding process [3]. The highest peak temperatures of the weld process are observed in the weld pool. The peak temperatures will progressively decrease away from the center of the weld pool. Rosenthal's equation may be used to map the heat flow distribution in a plate from a quasi-stationary point heat source [31]. An example, taken from the work of Myhr, shows a measured and a predicted weld thermal cycle in the fixed-point P in aluminium plate welding. The example is presented in Figure 2-10.

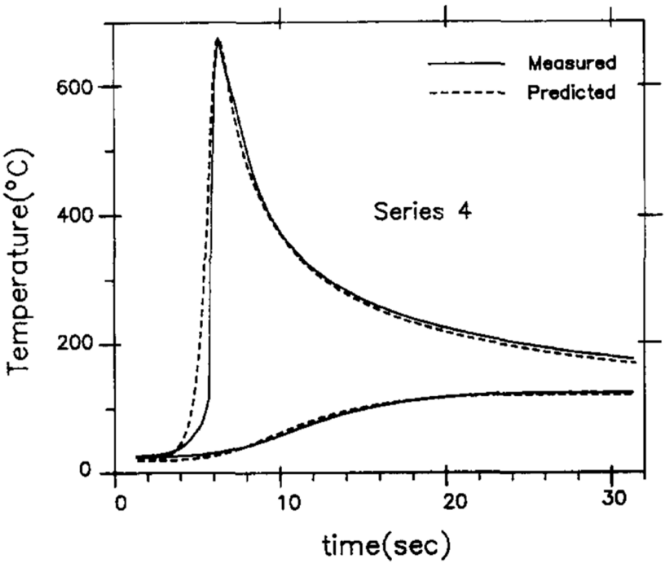

*Figure 2-10: Comparison between measured and predicted weld thermal cycles in MIG welding of an Al-2,5 wt% Mg plate for fixed values of $T_p$ [31].*

### 2.2.3 Heat flow distribution by Rosenthal's equation

Analytic models have been developed to predict the weld thermal program. A fair model for welding is the *"Thick plate solution"* version of Rosenthal's equation, given in Equation 2-1 [1]. It assumes a point heat source moving across an isotropic semi-infinite body with an initial temperature ($T_0$) [3]. An illustrative drawing has been presented in Figure 2-11. The thermal properties are assumed constant and independent of temperature, and heat losses by radiation and convection are ignored. The latent melting heat is ignored as well [3, 32].

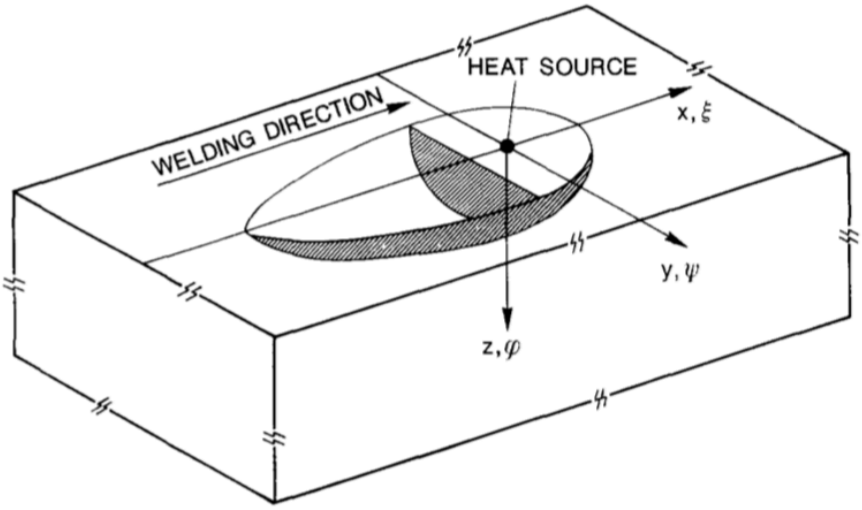

*Figure 2-11: Moving point source on a semi-infinite plate (3-D heat flow) [31].*

$$\boldsymbol{T - T_0 = \frac{q_0}{2\pi\lambda} \times \frac{1}{R} \times e^{-\frac{v}{2a} \times (R+x)}}$$ *Equation 2-1*

where

$$\boldsymbol{R = \sqrt{x^2 + y^2 + z^2}}$$ *Equation 2-2*

From Rosenthal's equation the *"Medium thick plate solution"* is extended for a point heat source with constant speed across a plate with given thickness. Constant material properties, no latent melting heat and no heat loss through the surfaces are assumed. The last condition is important with respect to reflecting heat, as it allows simulation of plate surfaces with extra heat sources. In order to maintain the net flux of heat through both plate surfaces equal to zero, is the heat reflection accounted for in the planes z=0 and z=d. By including all contributions from imaginary sources …. $2q_2$, $2q_1$, $2q_{-1}$, $2q_{-2}$, …. located symmetrically at distances ± 2id below and above the upper surface of the plate, the temperature increase in an arbitrary point P located within the plate is calculated on the basis of the "method of images", as shown in Figure 2-12. Where "d" is the plate thickness and "i" range from -∞ to ∞. The quasi-stationary temperature distribution is obtained in the form of a convergent series [3, 31-33] [1]:

$$\boldsymbol{T - T_0 = \frac{q_0}{2\pi\lambda} \times e^{-\frac{v}{2a}} \times \left[\sum_{i=-\infty}^{i=+\infty} \frac{1}{R_i} \times e^{-\frac{v}{2a} \times R_i}\right]} \qquad \textit{Equation 2-3}$$

where

$$\boldsymbol{R_i = \sqrt{x^2 + y^2 + (z - 2id)^2}} \qquad \textit{Equation 2-4}$$

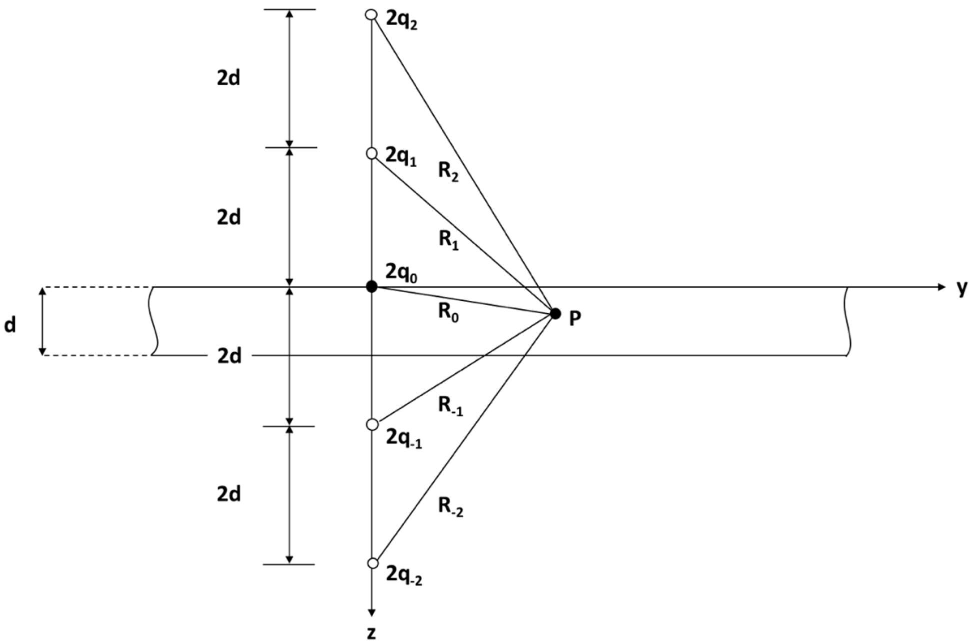

*Figure 2-12: Real and imaginary point heat sources for the medium thick plate solution [3, 31].*

## 2.3 THE SOFTENING REACTIONS OF WELDING AL-MG-SI ALLOYS

The age-hardening Al-Mg-Si alloys may offer tensile strength values higher than 350 MPa in T6 condition, but they are known to soften due to over-aging from welding [31]. Due to the thermal cycle of welding, change in microstructure and meta stable precipitates may cause severe softening in the HAZ. A typical hardness curve across an AA6061-T6 weldment is presented in Figure 2-13.

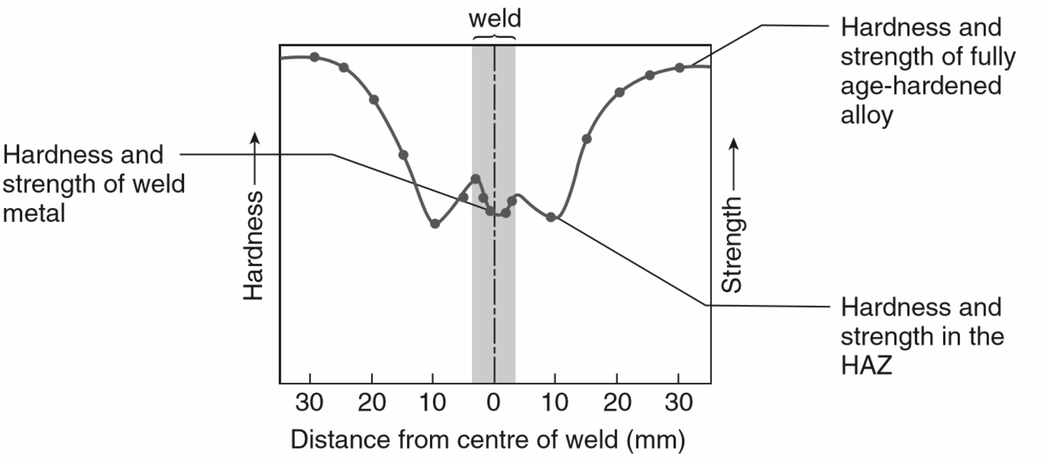

*Figure 2-13: Effect of welding on an AA6061T6 age-hardened alloy – as welded [28].*

Typical softening mechanisms occurring are particle coarsening, reversion, grain growth and recrystallization [3]. There is a potential strength reduction due to loss of alloying elements from the weld pool. Magnesium has a low boiling point and may be lost or oxidized during welding, but sufficient inert shielding gas may minimize this problem [28]. The microstructure of the fusion zone is dominated by solidified filler metal, but melted metal from the welded pieces is also present. This metal goes back to an as-cast state. Thereby, the memory of thermomechanical treatment gained through the past processing steps is lost [34]. The microstructure of this zone depends on the solidification behaviour of the weld pool, which controls size and shape of the grains, segregation, and distribution of inclusions and porosity [35].

### 2.3.1 Particle coarsening and reversion

Particle coarsening (Ostwald ripening) and reversion (particle dissolution) are the dominating processes in HAZ softening of the 6xxx-series [3]. The microstructural changes are explained by Figure 2-14, which is based on Myhr et al. The $\beta''$ particles, which forms under artificial aging, contributes to the strength of the 6xxx-series alloys, have low thermal stability.

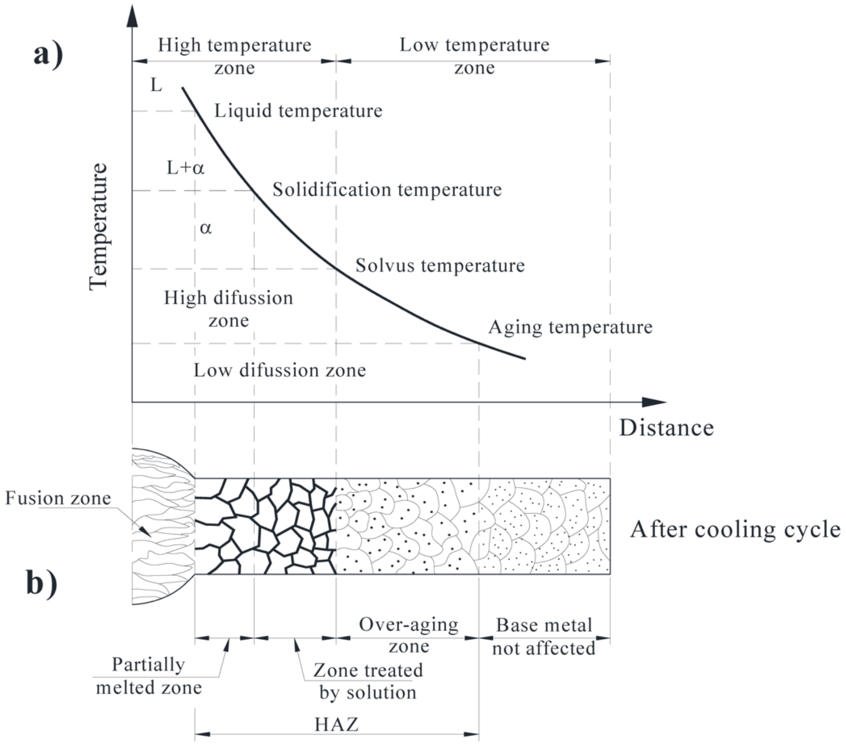

*Figure 2-14: Peak temperature evolution in the welded material moving away from the weld center (a) combined with microstructural changes (b).*

As seen in Figure 2-15, particle dissolution occurs typically above the equilibrium solvus, $T_{eq.}$, of the precipitates and below the eutectic temperature since there is no melting in the HAZ. The process is driven by the free energy change of transformation, which involves a change in the total volume fraction. In the area nearest to the fusion line, temperatures exceed the solvus temperature. Here, full reversion of the $\beta''$ particles is expected, resulting in a new local solution treatment. This area is shown by the partially melted zone and zone treated by solution in Figure 2-14 b). Hence, the material suffers severe softening in the area. However, a small increase in hardness after welding may be observed in the time after, due to effects of natural aging.

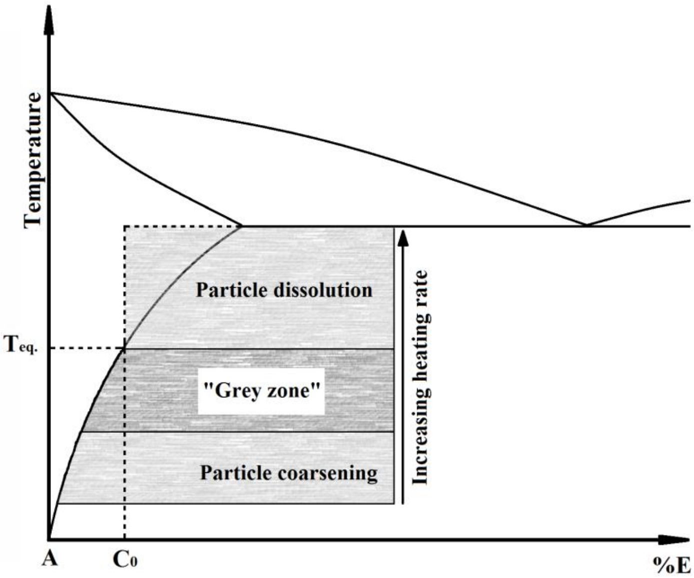

*Figure 2-15: Schematic diagram showing the characteristic temperature ranges where specific physical reactions occur during reheating of grain size-controlled and dispersion-hardened materials [3].*

Below the $T_{eq.}$, there is an interval named the “grey zone” in Figure 2-15, where both particle-coarsening and reversion may happen simultaneously. Coarser and rod-shaped β’ precipitates may form in the intermediate peak temperature range between 250°C and 480°C [29]. These β’ precipitates will grow rapidly in the presence of the abundant solute being supplied from the small, dissolving $\beta''$ precipitates. Below the “grey zone” interval, particle coarsening is the dominating process, which is driven by surface energy alone [3]. The phenomena of increased solubility of smaller particles than larger particles due to more favourable size and curvature is often referred to as the Gibbs-Thomson effect [3]. The areas where temperatures have been below this critical transformation temperature of particle coarsening will be unaffected by the weld thermal cycle. The strength losses are less in naturally aged metal than in the artificial aged alloys.

### 2.3.2 Grain growth, recrystallization and recovery

Due to the thermal cycle of the welding, the mechanical properties of the material are influenced by grain growth, recrystallization and recovery.

In general, grain growth is an important aspect of welding metallurgy as it has an influence on both strength and ductility. Normal grain growth in metals and alloys is a thermally activated process driven by the reduction in the grain boundary energy. Physically, it occurs by growth of the larger grains at the expense of the smaller ones [3]. During the process of deformation, e.g. extrusion, metallic materials has the ability to store crystal deformations. Hence, strain hardening increases the strength of metals. Stored dislocations are thermodynamically unstable. With increasing temperatures, the strain hardening effect becomes more and more unstable [19]. Through recovery and recrystallization, the metal will release the stored dislocations to lower its free energy. Recovery is usually defined as the restoration of the physical properties from strain hardening without any observable change in microstructure. Recrystallization is nucleation of a new set strain free grains. Recrystallization will, in addition to reduce strength, increase ductility [19]. During prolonged annealing, the recrystallized granular structure can coarsen, and is referred to as grain growth [36].

Precipitated particles reduce these effects. As explained in chapter 2.1.3, dispersoids of high thermal stability, containing Mn, Cr, Zr and Sc are important for retarding recrystallization, recovery and grain growth. A fibrous extruded microstructure after welding is a sign of high dispersoids and precipitate contents. Even though not all dispersoids contribute to improved strength it is a sign of microstructure control.

## 2.4 STRENGTH REDUCTION IN HAZ

The thermal cycle of the welding process has a major impact on the metallurgical and mechanical properties of the Al-Mg-Si alloys. This type of mechanical impairment represents a major problem in engineering design. Myhr et al. have developed tools to predict the strength of the Al-Mg-Si alloys after thermal processing, including welding. The different zones of the weld are linked to the representative material strength and hardness in Figure 2-16. The metallurgical mechanisms behind HAZ softening are explained in the previous chapter (Chapter 2.3).

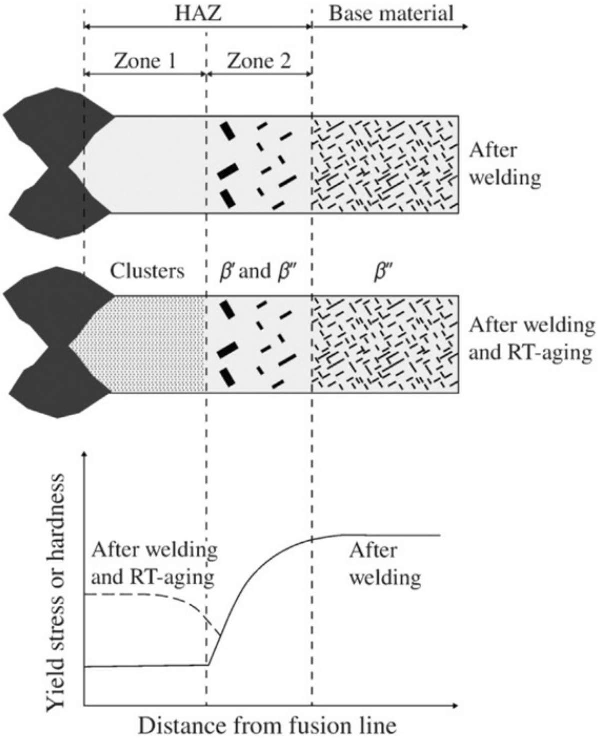

*Figure 2-16: Microstructural changes during welding and natural aging [37].*

### 2.4.1 Through Process Modelling

Through Process Modelling is a concept were different modelling tools are coupled together for analysis of the structural behaviour of welded aluminium structures. In short, the modelling concept relies upon the coupling of a welding simulation tool (WELDSIM), a microstructure model (NaMo) and a non-linear mechanical model (LS-DYNA) [38].

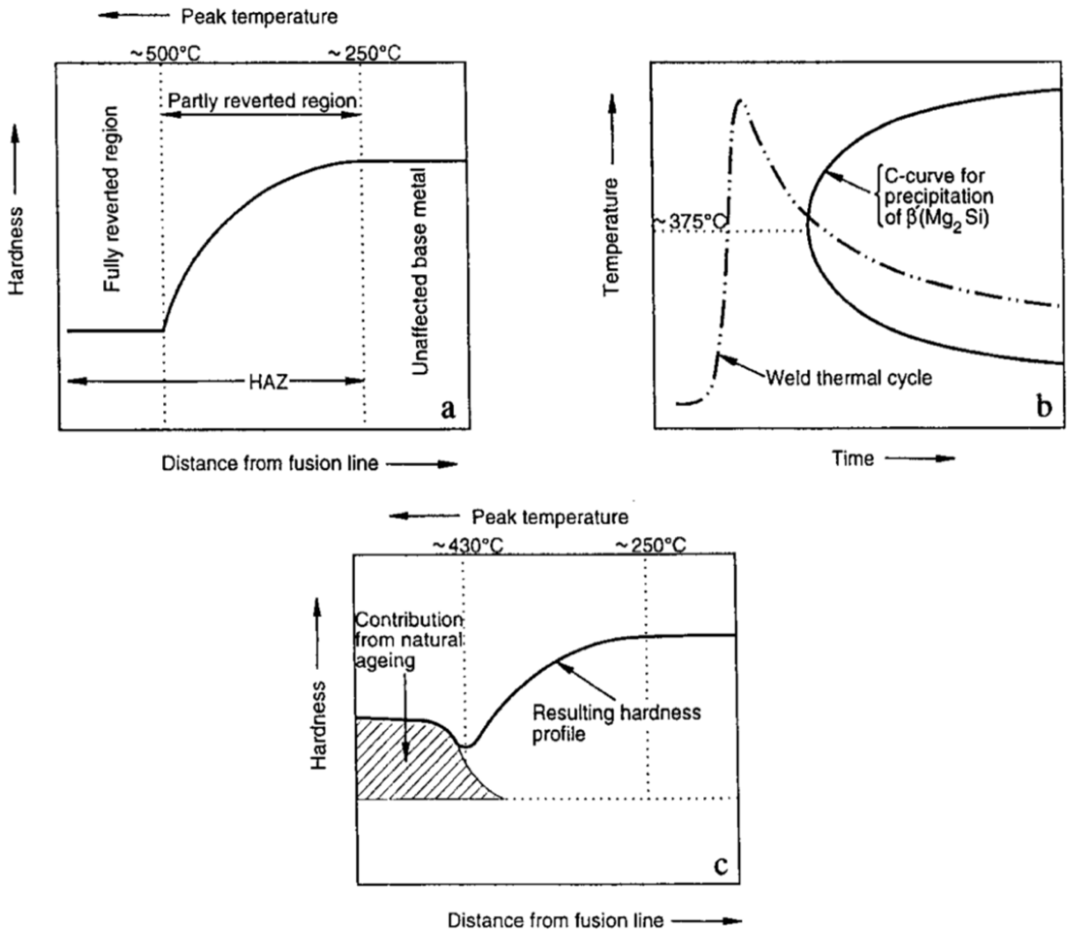

*Figure 2-17: Schematic diagrams showing the sequence of reactions occurring in the HAZ of 6082-T6 aluminium weldments: (a) hardness distribution following $\beta''$ dissolution; (b) precipitation $\beta'$ during the weld cooling cycle; (c) hardness distribution following prolonged room temperature ageing [2].*

In the numerical investigation, the scheme presented by Myhr et al. is to be followed. A thermomechanical analysis of the welding process is carried out by means of WELDSIM to determine the temperature field in the weld, HAZ and surrounding base material. This field of thermal histories is used as an input to the microstructure model NaMo which determines the spatial distribution of the mechanical properties in the HAZ. These results are then transferred to LS-DYNA for the structural response analysis [38].

### 2.4.2 Eurocode 9

When designing welded structures made of aluminium, it is important to account for the reduction in strength properties due to the presence of the heat affected zone. The design standard Eurocode 9 is to be used when designing load bearing structures by aluminium. Numerical values for partial factors and other reliability parameters are provided as basic values for an acceptable level of reliability. They have been selected assuming that an appropriate level of workmanship and quality management is applied.

The extent of the HAZ ($b_{haz}$)for a MIG weld deposited on unheated material, with interpass cooling to 60°C or less for multi-pass welds, is in Eurocode 9 (Section 6.1) thickness dependent. $b_{haz}$ is given in Table 2-3. An illustration of how the $b_{haz}$ is measured is presented in Figure 2-18.

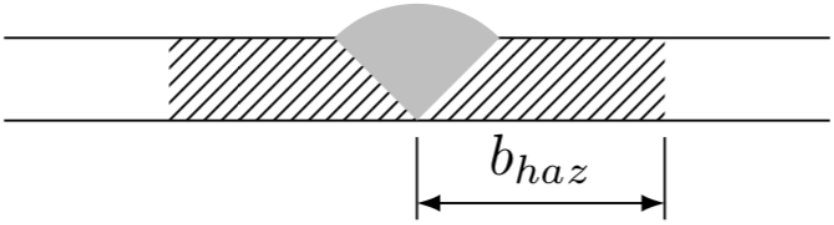

*Figure 2-18: Extent of HAZ from a weld ($b_{HAZ}$) [5].*

*Table 2-3: $b_{haz}$ applicable for different thicknesses given by Eurocode 9 (section 6.1.6.3) [5].*

| **Thickness range** | $\mathbf{b_{haz}}$ |
|---|---|
| 0-6mm | 20 |
| 6-12mm | 30 |
| 12-25mm | 35 |
| 25mm<t | 40 |

A study done by Nyhus et al. has observed that $b_{haz}$ is smaller than what specified in the standard [39]. They tested aluminium profiles with thicknesses between 10 mm and 40 mm and found that material thickness does not have a significant effect on the width of the HAZ.

Generally, it is assumed that the HAZ is stretched 25 mm out from the weld center line, if adequate procedures have been implemented [40].

The yield strength and tensile strength are important parameters for calculating the load-bearing capacity of a structure. A set of values for yield strength ($f_0$) and ultimate tensile strength ($f_u$) for different alloys, unwelded and in the HAZ, are given in Eurocode 9. The valid strength values given for EN AW-6082 as set in Eurocode 9 are presented in Table 2-4. Reduction factors are determined by Equation 2-5.

$$\boldsymbol{\rho_{HAZ} = \frac{f_{HAZ}}{f}}$$

*Equation 2-5*

*Table 2-4: Characteristic values for 0,2 proof stress ($f_0$), ultimate tensile strength ($f_u$), for both unwelded and HAZ, for EN AW-6082, and reduction factors $\rho_{0,HAZ}$ and $\rho_{u,\,HAZ}$.[5]*

| **Temper** | **$f_{0,haz}$ [MPa]** | **$\rho_{0,haz}$** | **$f_{u,haz}$ [MPa]** | **$\rho_{u,\,haz}$** |
|---|---|---|---|---|
| **T4** | 100 | 0,91 | 160 | 0,78 |
| **T6** | 125 | 0,49 | 185 | 0,62 |

## 2.5 LOCAL LASER HEAT TREATMENT

A heat source, such as light amplification by stimulated emission of radiation (laser) or induction spools, may be used on the 6xxx-series to tailor the properties of the material by heat treatment. However, it is difficult to test different heat treatment layouts and it is therefore challenging for scientific investigations. Some research has been done on the topic under the term “Tailored Heat-Treated Blanks (THTB)” [41]. It is especially forming limits during manufacturing which have been enhanced by THTB.

By using THTB different microstructural changes can be used to adapt the mechanical properties by a local heat treatment. Generally, three microstructural mechanisms are aimed at: recrystallizing the grain structure, annealing and modifying the precipitation structure[42].

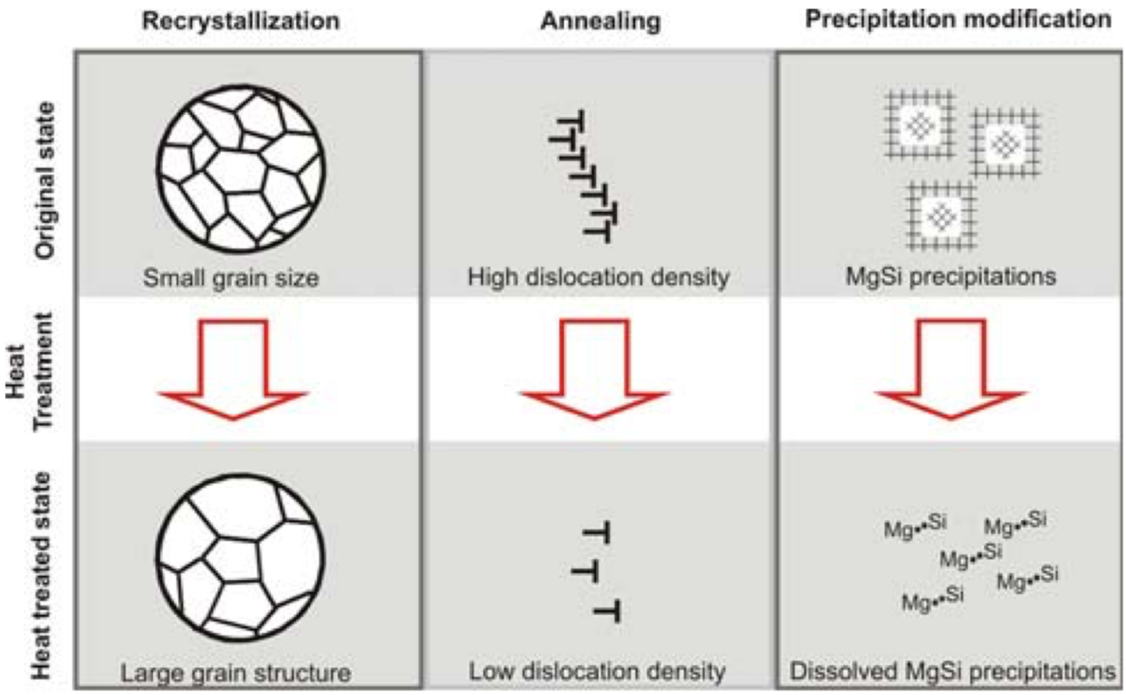

*Figure 2-19: Three microstructural effects due to a short-term local heat treatment of aluminium alloys [42].*

### 2.5.1 Manipulation of HAZ geometry

Norsk Hydro has put forward the idea of manipulating the HAZ geometry by the use of local heat treatment. In conventional welding, welding strings are often deployed in straight lines, leaving a HAZ parallel to the weld. By creating a more complex HAZ geometry it is possible to change stress and strain distribution in the material during tensile testing and thereby increase the global strength of the component. Numerical tests and finite element analysis (FEA) have been conducted by Fjær at the Institute of Energy Technology (IFE), investigating the basic concept of this idea with promising results [6]. Three zones with different mechanical properties, T4, HAZ and T6, have been combined together in different patterns in the FEA. An image from the FEA is presented in Figure 2-20. The tests showed that it is possible to obtain strength increase of 10% in a design with bulged pattern than for a straight HAZ, as shown in Figure 2-21.

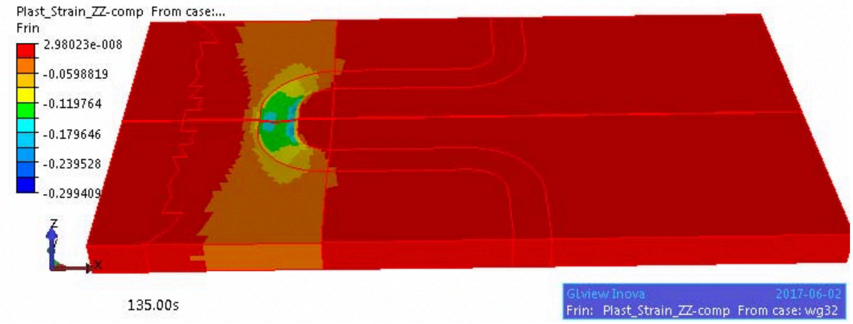

*Figure 2-20: Finite element analysis of the HAZ [6].*

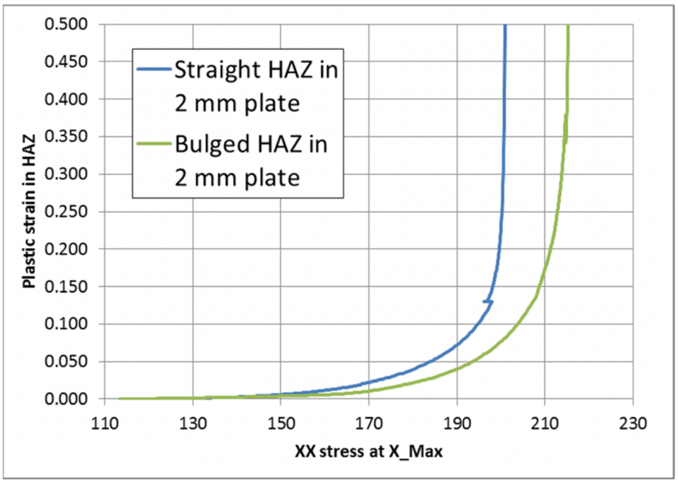

*Figure 2-21: Stress-strain curves from the FEA [6].*

## 2.6 CALCULATION OF MECHANICAL PROPERTIES

### 2.6.1 Load bearing capacity of welded components

Yield stress across the HAZ profile can be calculated from hardness measurements by using the relationship presented in Equation 2-6.

$$\boldsymbol{R_{p0.2}(MPa) = 3.0 \times HV - 48} \qquad \text{Equation 2-6}$$

where $HV$ is hardness and $R_{p0,2}$ is yield strength.

By inserting the minimum value from the HAZ hardness profile into Equation 2-7, the corresponding minimum HAZ yield strength $R_{min}$ can be found. If the loading is perpendicular to the weld, as shown in Figure 2-22, the load-bearing capacity, $P$, can be calculated by using the relationship:

$$\boldsymbol{R_{min} = \frac{P}{d \times W}} \qquad \text{Equation 2-7}$$

from which:

$$\boldsymbol{P(kN) = R_{min} \times d \times W} \qquad \text{Equation 2-8}$$

where $P$ is the maximum tensile (or compressive) force that can be applied perpendicular to the axis of the weld, when $d$ is the plate thickness and $W$ is the width of the component.

In engineering design $R_{min}$ has a direct physical meaning, since it is the key parameter determining the joint strength when the loading is perpendicular to the weld.

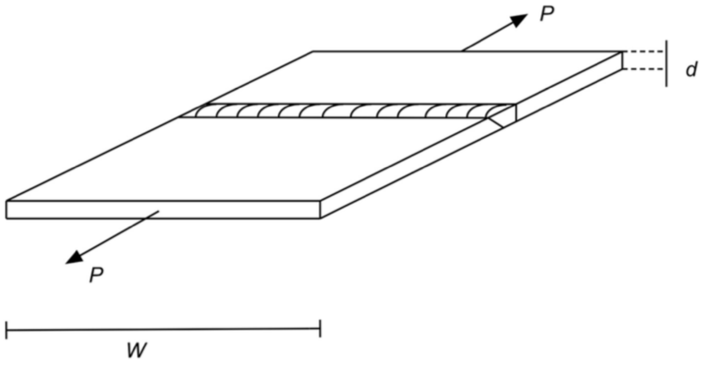

*Figure 2-22: Loading perpendicular to the weld [40].*

### 2.6.2 Toughness

Toughness is defined as the ability of a material to absorb energy and plastically deform before fracturing. For brittle materials a Charpy test is often used to get a measurement of the toughness. For a ductile material, the area under the curve in a stress-strain plot is used to measure the amount of work per unit volume that the material may be exposed to without fracturing. Toughness, $U_T$, may be approximated from Equation 2-9.

$$\boldsymbol{U_T = \frac{R_{p0.2}+R_m}{2} e_f} \qquad \text{Equation 2-9}$$

where $R_{0.2}$ is the engineering yield stress, $R_m$ is the engineering ultimate tensile stress and $e_f$ is the engineering strain at fracture.

# 3 EXPERIMENTAL

The challenge in this thesis is to test if local heat treatment can change the geometry of the HAZ and hence positively impact the welded component's strength.

Mechanical testing of a reference without any local heat treatment has been established. Thereafter, the reference has been compared to specimens where local heat treatment has been applied by laser to change the HAZ geometry. The experimental method applied with relevant procedures are presented in this chapter. The base material and its history has been described as well.

## 3.1 BASE MATERIAL EN AW-6082

The experiment has been carried out on a profile of the alloy EN AW-6082. A 1700 mm long profile of thickness 3.6 mm was applied. The profile was solution heat-treated, extruded and artificial aged (T6) from Hydal Aluminium Profiler AS at Raufoss. The received extruded profile was cut by hand using an angle grinder before welding was conducted at NTNU Gløshaugen. The work process is illustrated in Figure 3-1.

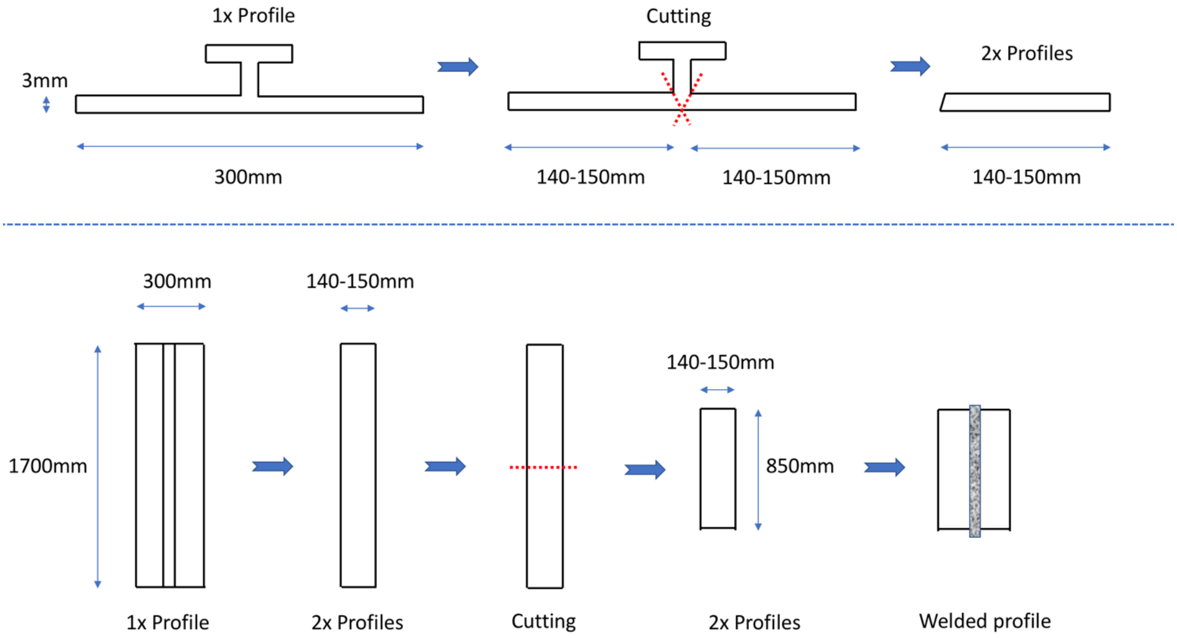

*Figure 3-1: Work process of the cutting process and welding of the received profile to welded product.*

### 3.1.1 Chemical composition

The chemical composition of the profile (EN AW-6082-T6) is given in Table 3-1. The compositions have been provided from the casting at Norsk Hydro. The material certificate has been given in Appendix 1.

*Table 3-1: Chemical composition*

| | **Si** | **Mg** | **Mn** | **Fe** | **Ti** | **Zn** | **Cu** | **Cr** | **Al** |
|---|---|---|---|---|---|---|---|---|---|
| **Profile** | 0.99 | 0.66 | 0,54 | 0.20 | 0.02 | 0.00 | 0.01 | 0.01 | Remainder |
| **Eurocode** | 0.7-1.3 | 0.6-1.2 | 0.4-1.0 | 0.50 | 0.10 | 0.20 | 0.10 | 0.25 | Remainder |

### 3.1.2 Extrusion, homogenization and artificial aging

Homogenization has been performed by SINTEF Raufoss Manufacturing for three hours at 555°C. A heating rate of 200°C/hour and a cooling rate of 350°C/hour was applied. Hydal Aluminium Profiler AS conducted extrusion and artificial aging in their extrusion machine at Raufoss. Artificial aging was conducted at 185°C for five hours. Information from the extrusion process has been presented in Table 3-2. Billet temperature in billet loader ($T_{billet}$), maximum ram speed ($v_{max}$), average ram speed ($v_{avg}$) and maximum pressure ($P_{max}$) is provided.

*Table 3-2: Extrusion parameters*

| $T_{billet}$ **[°C]** | $v_{max}$ **[m/min]** | $v_{avg}$ **[m/min]** | $P_{max}$ **[bar]** |
|---|---|---|---|
| 480 | 8.14 | 5.87 | 158 |

## 3.2 WELDING PROCEDURE

The welding was conducted at SINTEF Materials and Chemistry at NTNU Gløshaugen. The profiles were butt-welded along the extrusion direction to form a plate with nominal length of 850 mm and width of 290 mm, with the weld along its centre line, as illustrated in Figure 3-2. The profiles were welded with a fully automatic welding robot using 131 MIG Pulse, single sided welding and stainless-steel backing. The aluminium-based filler material used was AlMg4.5Mn (AA5183) with diameter 1.2 mm. The minimal mechanical properties of the welding wire as welded metal, provided by the manufacturer, are presented in table 3-2.

*Table 3-3: Minimal values of mechanical properties of the welding wire as welded metal.*

| **Yield strength** $R_{p0,2}$ | **Tensile strength** $R_m$ | **Elongation** $\varepsilon$ |
|---|---|---|
| 125 MPa | 275 MPa | 17% |

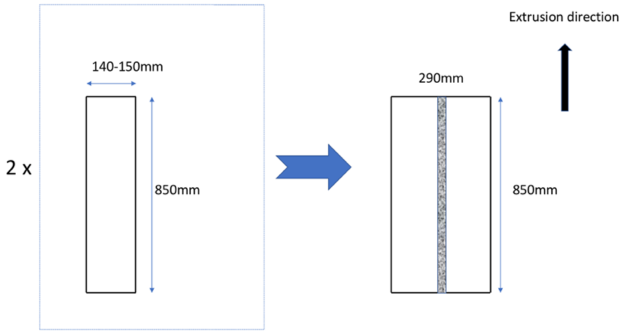

*Figure 3-2: Work drawing of the welded profile.*

Important parameters from the welding process are listed in table 3-3.

*Table 3-4: Welding parameters*

| **Passes** | **Wire feed speed [m/min]** | **Current [A]** | **Voltage [V]** | **Welding speed [mm/s]** | **Gas [L/min]** |
|---|---|---|---|---|---|
| 1 | 7 | 115 | 18,5 | 10 | 12 |

## 3.3 LASER HEAT INPUT

A robotised laser, located at SINTEF Raufoss Manufacturing, has been used in the experiment to manipulate the HAZ geometry of a welded profile. The laser is shown in Figure 3-3. To manipulate the geometry of the HAZ a heat source need to be applied to create a new thermal cycle which effect the precipitation sequence. Two thermocouple measurements tests were conducted to verify laser heat input and material heat distribution.

*Figure 3-3: The laser stationed at SINTEF Raufoss Manufacturing.*

### 3.3.1 Static laser on cube

In the first test the laser was set on a fixed point of an aluminium cube with sides of 25 mm. Five holes were drilled 12.5 mm into the cube for the thermocouples at strategic locations to measure the heat distribution throughout the material. An image of the setup is presented in Figure 3-4.

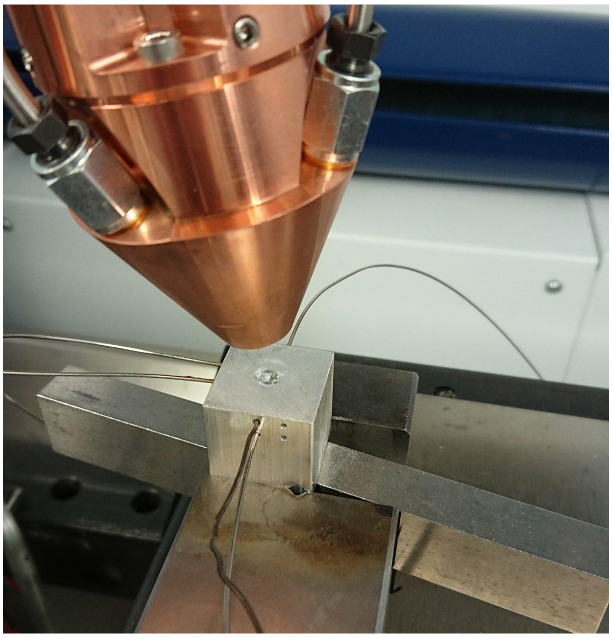

*Figure 3-4: Image of the setup in the static laser on cube test.*

### 3.3.2 Moving laser on profile

The laser was tested by running it over a profile of the same extruded material as used for the welded profile in this thesis. Eleven runs were carried out with different parameters and temperatures measured by five thermocouples. Three thermocouples were placed in drilled holes at distances 2.28 mm, 3.28 mm and 4.16 mm away from the center of the laser beam to measure the material temperature at the surface. The recorded measurements have been applied together with a heat distribution model to estimate the efficiency factor ($\eta$) of the laser on the aluminium surface. It should be noted that the locations of the thermocouples are different in laser moving direction (x-direction). This will be reflected in a time delay of the thermocouple measurements at 3.28 mm and 4.16 mm compared to the one at 2.28 mm. The laser moving direction is from right to left in Figure 3-5, and the laser will pass by the thermocouple at 2.28 first.

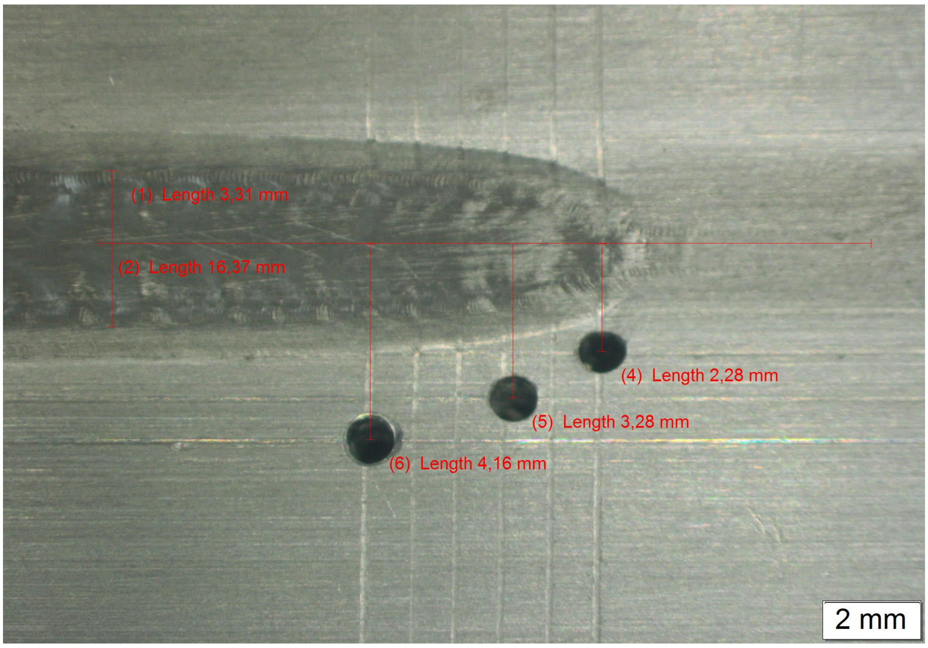

*Figure 3-5: Illustrative picture of the profile with the holes drilled for thermocouples. The material began to melt when the laser passed by the location of the thermocouples.*

## 3.4 EXPERIMENTAL TESTING

### 3.4.1 Pre-experiment

A pre-test was done on a hand welded spare profile, from the same extrusion batch as the profile from the experiment, to establish basis for the work programme. A MIG welded string were laid on the profile's surface, without joining to pieces, to imitate a welded profile. The laser parameters for the pre-experiment were set with the experiences gained from the laser distribution tests. Setup for the laser treatment is shown in Figure 3-6 a). Laser treatment was supposed to give solution treatment, but melting was not desired. If melting occurs, microstructure will lose thermomechanical history gain through solution treatment and extrusion. Nevertheless, some areas of the pre-experiment's laser treated patterns did experience melting. The first side to be laser treated started to melt during the laser treatment, like in the last run of the laser distribution test. For the side of the weld secondly laser treated, melting occurred continuously due to insufficient cooling between first and second laser treatments. The laser treated profile can be seen in the Figure 3-6 b). A laser effect (Q) of 2600 W was used, laser spot diameter ($\phi$) were set to 3 mm and v was 10 mm/s.

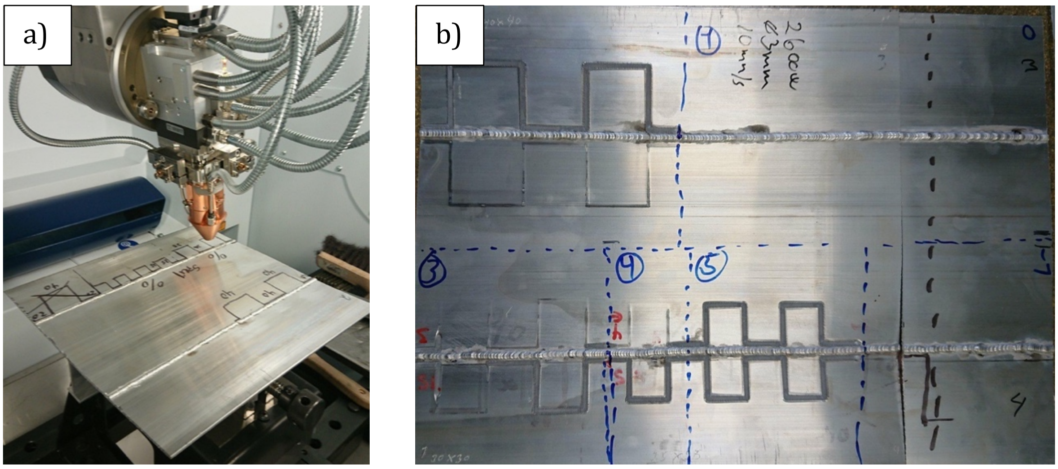

*Figure 3-6: Image of laser setup with the pre-experiment profile.*

Proof of concept was achieved during this pre-experiment as imaged in Figure 3-7. Here, the fracture followed the pattern made by the laser. No comparison could be made regarding if the laser heat treatment had improved the strength of the welded component could be made.

The other specimens were of different geometries and many of them fractured in the clamping.

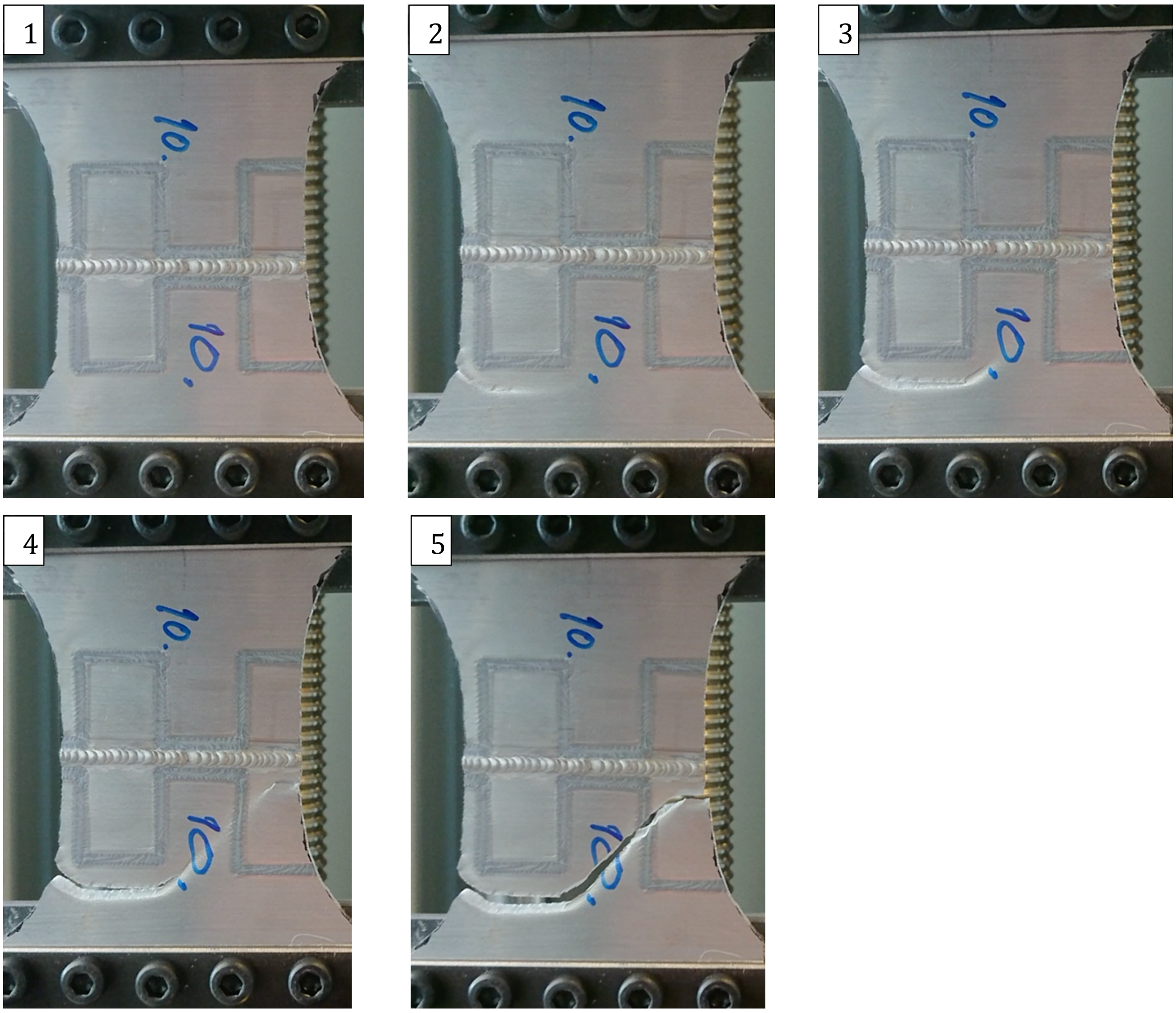

*Figure 3-7: Proof of concept. A laser treated specimen strained to fracture.*

### 3.4.2 Experiment

From the welded profile, five equal large specimens with different layout of heat treatment patterns was made for tensile testing. A layout for the laser treatment was made out to imitate the patterns in the concept study conducted by Fjær (Chapter 2.6.1). The laser patterns marked on the welded profile has been shown in Figure 3-8. All laser treatment patterns were symmetrical on each side of the weld. The idea is that strain and fracture propagation will follow the undermatching properties of the laser pattern instead of the weld

HAZ. One reference specimen without laser treatment was used for comparison. The welded profile distorted due to material contraction during and after the welding process. Before the laser treatment was applied, the profile was cut in three parts of equal size. A and B was one part, C and D was another part and last one was the reference. The cutting had a straightening effect on the three cut-out pieces. No further mechanical treatment was necessary to have an approximate equal working distance for the laser.

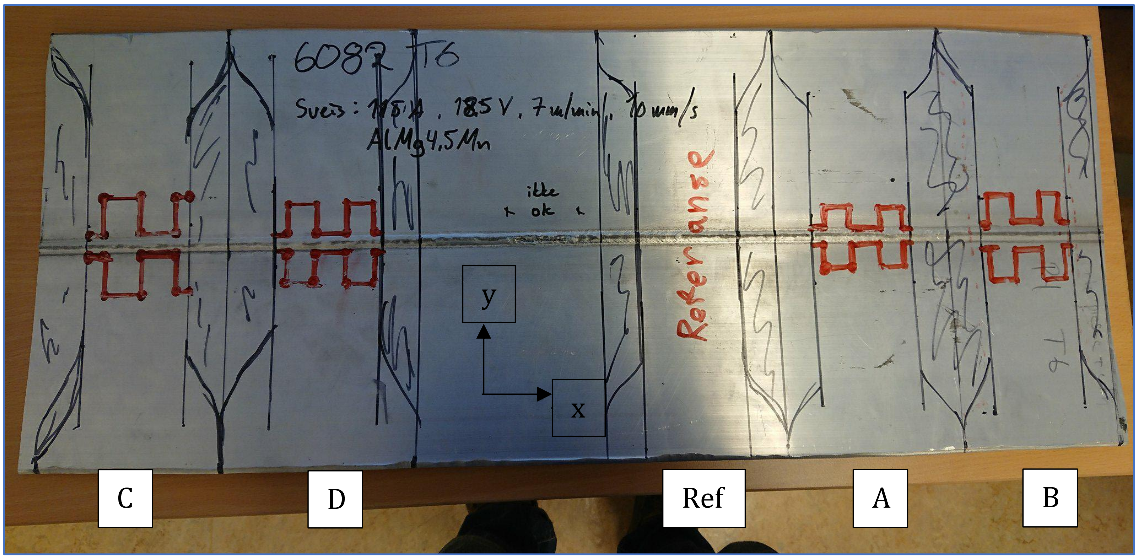

Figure 3-8: Image of the welded profile with patterns for the laser treatment and tensile test specimen geometry.

A working distance of 1 mm to the surface of the welded profile was applied, as applied for the pre-tests in chapter 3.4. The laser treatment parameters were set based on the experiences gained from the heat distribution tests and the pre-experiment. The laser parameters were set to give a continuous melting for the laser treatment patterns. Due to the assumptions that this had strengthen the unfractured sides in the pre-experiment. Continuously melting was also supposed to give easy comparable data, as it would give consistent results. From the pre-experiment the laser effect was kept at 2600 W. The laser spot diameter was 3 mm. To ensure melting the laser speed was reduced to 9 mm/s.

The two first specimens, Specimens A and B, were laser treated with these parameters. Melting was obtained for the whole laser pattern. The laser did not burn through the underneath oxide surface layer of the profile, but when the specimens was turned around and inspected after the laser treatment, distortions from the laser pattern was observed under. The laser treatment was considered too hot. To reduce the heat input per unit length, the *v* was increased to 9.33 mm/s for Specimens C and D. This resulted in less melting as seen from the microscopy investigations. Specimen B, C and D was cleaned with ethanol to remove marker ink before the laser treatment, this was not done for Specimen A. To reduce end-effects the pattern was continued for 15 mm outside the specimen form. An overview of the laser pattern geometry and laser parameters have been given in Table 3-5. Distances between the fusion line and the laser center line is given as (l). Pattern is given by height (h) and width (b) as displayed in Figure 3-9.

*Table 3-5: Overview of the laser parameters and pattern geometry used for the experiment.*

| **Specimen** | **Laser effect** | **Spot diameter** | **v [mm/s]** | **b*h [mm]*[mm]** | **l [mm]** |
|---|---|---|---|---|---|
| **Ref** | - | - | - | - | - |
| **A** | 2600 | 3 | 9 | 20*15 | 1.5 |
| **B** | 2600 | 3 | 9 | 20*20 | 3.5 |
| **C** | 2600 | 3 | 9.33 | 25*25 | 1.5 |
| **D** | 2600 | 3 | 9.33 | 20*20 | 1.5 |

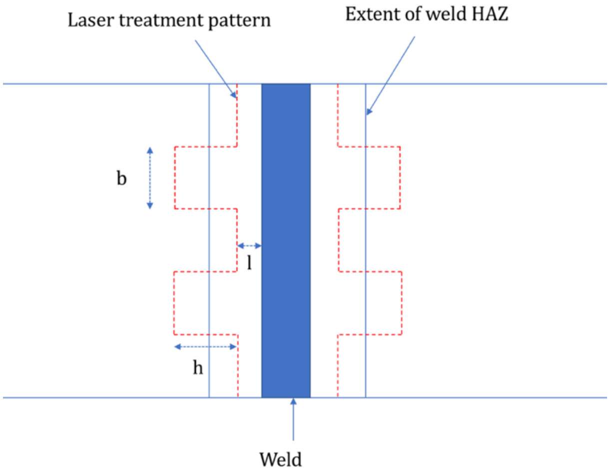

*Figure 3-9: Illustrative drawing of the laser treatment pattern.*

## 3.5 MATERIAL CHARACTERIZATION METHODS

Cross-weld tensile testing was performed on all five specimens after laser heat treatment. Analysis of microstructure by optical microscopy and hardness measurements across the weld have been carried out on the cut-off sides of the tensile test specimens extracted from the welded plate.

### 3.5.1 Sample preparation

Samples for optical microscopy and hardness measurements were extracted from the spare material of the tensile test specimens. The spare material and location of the extracted samples can be seen in Figure 3-10. The samples had 60 mm width, where the weld line was located in the center. A water cooled Discotom cutting tool was used. The depth of the samples in welding direction was approximately 20 mm due to practicality with respect to cold mounting in Epofix resin. All samples have been taken from the side where the laser treatment started.

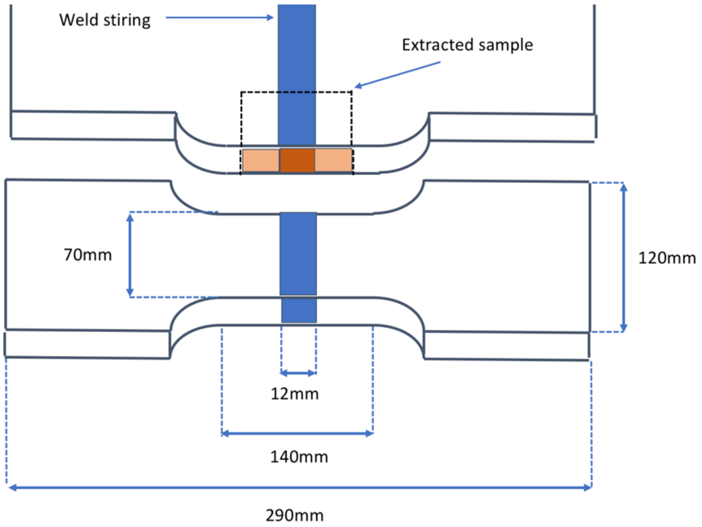

*Figure 3-10: Work sketch of the extraction of optical microscopy and hardness measurement samples. Here, together with the tensile test sample. The area coloured orange was examined in microscopy and for hardness.*

### 3.5.2 Grinding and polishing

The mounted samples were then grinded by the use of water proof SiC grinding papers with increasing fineness. Grinding papers used were P500, P800, P1200, P2400 and P4000, presented in chronological order. During grinding, water was used as lubricant. The samples were handheld during the grinding process.

Grinding was followed by polishing of the samples by the use of 9, 3 and 1 µm polishing disks, with DiaPro Mol and OP-S suspensions respectively. In between each grinding and polishing step, all samples were rinsed in soap water and ethanol. For polishing, a sample holder and a Struers modular rotating preparation systems was used.

### 3.5.3 Anodising

Anodising was performed on selected samples in order to examine the grain orientation and moreover the extent of the recrystallized layer after extrusion. The process involved immersion of selected samples in an electrolyte containing 5 % $HBF_4$ and 95 % $H_2O$ by volume. The potential and current were set to 20 V and 1 A, respectively. A holding time of approximately 90 seconds was found to provide satisfactory results. Finally, all samples were immediately washed in water and ethanol after immersion and then air dried.

### 3.5.4 Optical microscopy

The specimens where examined in a Leica MeF4M optical microscope with a lens of magnification 2.5x. The software Pixelmator was used to montage several microscope images to one overview image of each sample.

### 3.5.5 Hardness measurements

Hardness across the weld was measured to establish the extent of HAZ and the hardness in the different zones of the weld. The hardness of the samples was measured after the optical microscopy by using the machine Zwick/Roell ZHV 30. The samples were grinded with P500, P800 and P1200 to remove the anodised layer. Impression force was set to 1 kg (HV1) and dwell time was 10 seconds. The hardness is measured from one side and across to the other side with the weld in the center, 1 mm between each impression. For each sample 2-3 parallels were run (top, middle and bottom of the sample), as shown in Figure 3-11. All hardness measurements were made more than a week after heat treatment.

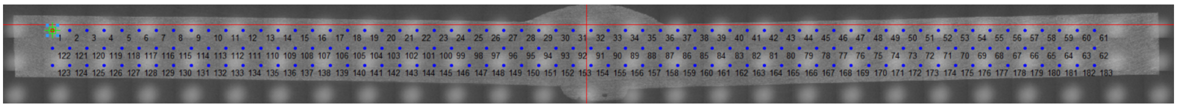

*Figure 3-11: Imprint pattern for the hardness measurements of the welded samples.*

### 3.5.6 Cross-weld Tensile Testing

The five specimens were extracted from the welded profile by the use of water jet cutting at "Finmekanisk verksted" at NTNU. Cross-weld tensile tests at room temperature were done by SINTEF Materials and Chemistry at Gløshaugen. The specimens were tested at constant strain rate of 4.2 mm/min. From the logged force-time data, the 0.2 % proof strength (Rp(0.2)), the stress to achieve 0.5% elongation (Rt(0.5)), ultimate tensile strength (Rm), total elongation and toughness were calculated and reported.

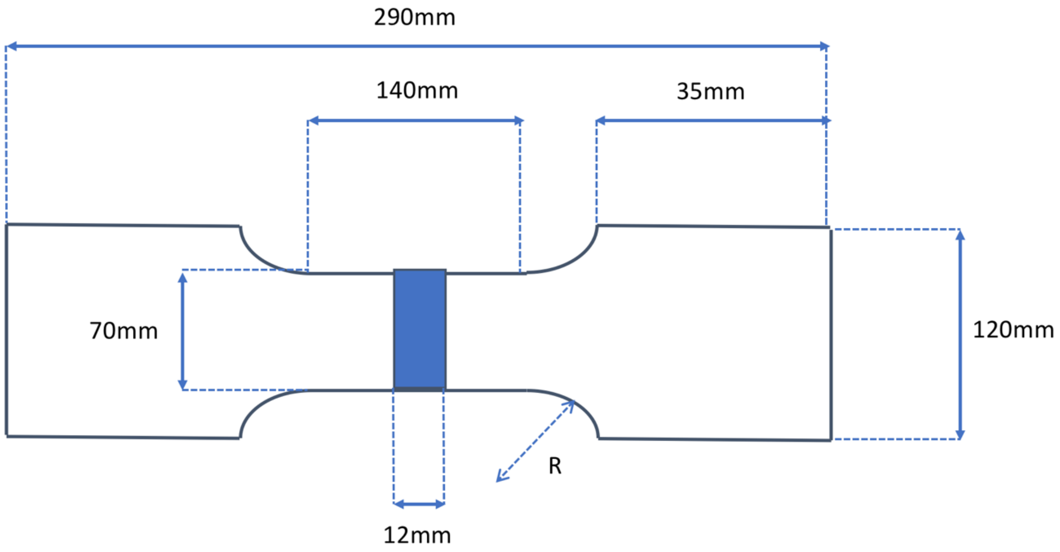

*Figure 3-12: Work sketch of the cross-weld tensile test specimens. The weld was centred in the middle of the specimens.*

Digital image correlation (DIC) was used to map the deformation and estimate the strain in the specimens during testing. The test setup is imaged in Figure 3-13. It is possible to get a full picture of the deformation and localization of the strain during testing by the use of DIC. In combination with the obtained stress-strain curves for the different regions of the HAZ. Stress-strain curves and movies with visualization of the strain were made.

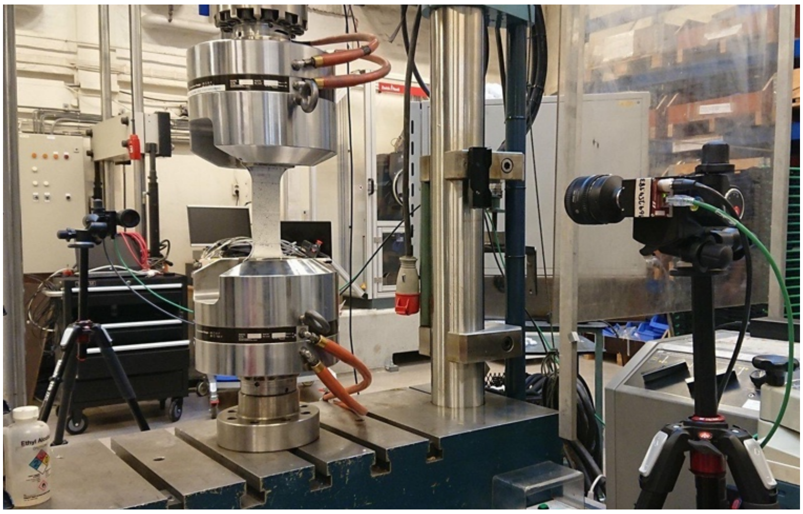

*Figure 3-13: Setup of the tensile test with camera for DIC recording.*

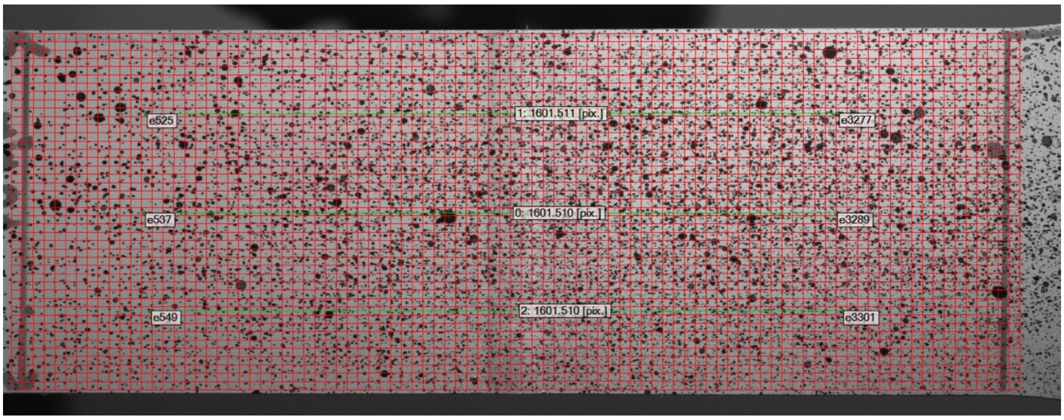

*Figure 3-14: The mech and three vectors on the Reference specimen used for calculating strain in DIC post processing.*

# 4 MODELLING

## 4.1 HEAT DISTRIBUTION MODEL FROM ROSENTHAL'S EQUATION

A heat distribution model for a moving heat source has been created to analyse the heat distribution in the aluminium profile by welding and laser treatment. The model is based on the "Medium thick plate solution", Equation 2-3, after Rosenthal for heat distribution by a moving point source [3, 31]. The equation is commonly applied for welding modelling, and research has verified the use of it in several studies. The model has been made in Microsoft Excel and contains applications for thermal cycle and peak temperature distribution in the y-direction. Directions are explained by Figure 4-1.

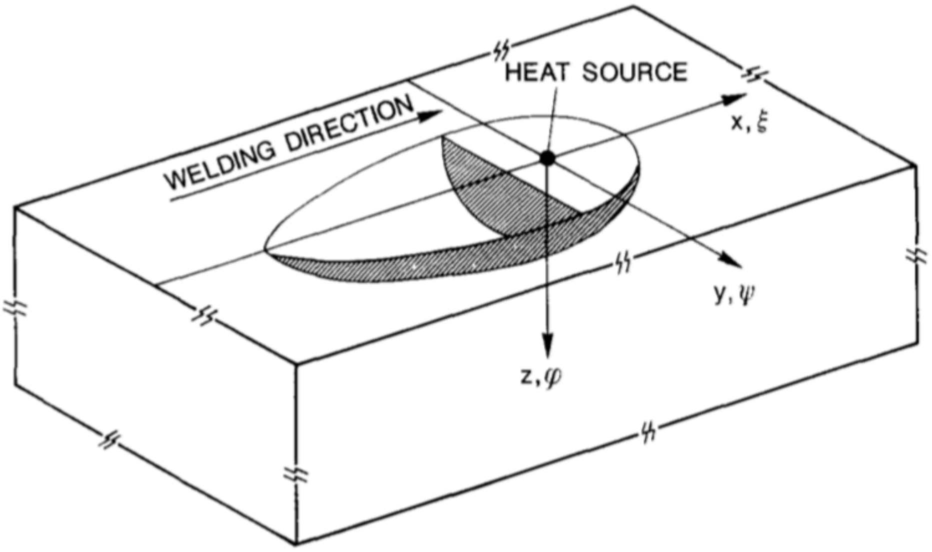

*Figure 4-1: Moving point source on a semi-infinite plate (3-D heat flow) [31].*

The thermal conductivity (λ) and volume heat capacity (ρc) of Al-Mg-Si alloys are 0.167 W/(mm·°C) and 0.0027 J/(mm$^3$·°C), respectively [3].

Figure 4-2 show the input spreadsheet for the heat distribution model.

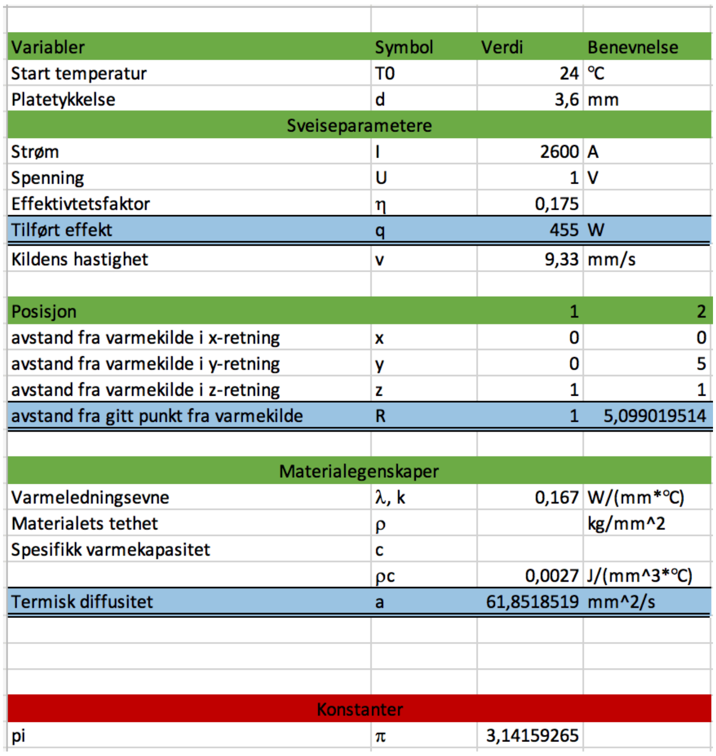

| Variabler | Symbol | Verdi | Benevnelse |
|---|---|---|---|
| Start temperatur | T0 | 24 | ℃ |
| Platetykkelse | d | 3,6 | mm |
| Sveiseparametere | | | |
| Strøm | I | 2600 | A |
| Spenning | U | 1 | V |
| Effektivtetsfaktor | η | 0,175 | |
| Tilført effekt | q | 455 | W |
| Kildens hastighet | v | 9,33 | mm/s |
| | | | |
| Posisjon | | 1 | 2 |
| avstand fra varmekilde i x-retning | x | 0 | 0 |
| avstand fra varmekilde i y-retning | y | 0 | 5 |
| avstand fra varmekilde i z-retning | z | 1 | 1 |
| avstand fra gitt punkt fra varmekilde | R | 1 | 5,099019514 |
| | | | |
| Materialegenskaper | | | |
| Varmeledningsevne | λ, k | 0,167 | W/(mm*°C) |
| Materialets tethet | ρ | | kg/mm^2 |
| Spesifikk varmekapasitet | c | | |
| | ρc | 0,0027 | J/(mm^3*°C) |
| Termisk diffusitet | a | 61,8518519 | mm^2/s |
| | | | |
| | | | |
| | | | |
| Konstanter | | | |
| pi | π | 3,14159265 | |

*Figure 4-2: The spreadsheet for input in the model.*

The simplifying assumptions for the model [1, 31]:

- Homogeneous and isotropic material with no phase transformations upon heating.
- Constant thermal conductivity, density and specific heat are constant.
- Insulated base material
- The material is infinite in all direction, except thickness
- The heat source is concentrated to a zero-volume point or line.
- Pseudo-steady state

### 4.1.1 Net heat input received by the material

In arc welding, the heat source energy($Q$) is determined by arc voltage ($U$) and welding current ($I$) as given in Equation 4-1.

$$\boldsymbol{Q = IU}$$

Equation 4-1

For laser treatment Q is the set laser effect. The net heat input received by the weldment ($q_0$) is determined Equation 4-2. Heat losses by reflection, convention and radiation are taken into account by the efficiency factor ($\eta$) [3].

$$\boldsymbol{q_0 = Q\eta}$$

Equation 4-2

For MIG welding, $\eta$ has been reported in the range from 0.65 to 0.85 [3]. In this thesis 0.85 has been used. The efficiency factor for laser treatment has been analysed from results obtained in experimental testing of laser heat input in aluminium by thermocouples.

# 5 RESULTS

## 5.1 MODELLING OF THE WELD THERMAL CYCLE

The heat distribution model has been used to map the heat distribution in the material during welding. Modelled thermal cycles at distances of 0, 5, 10, 15, 20 and 25 mm in the y-direction of the material, and 1 mm in z-direction are presented in Figure 5-1. η = 0.85. Directions are given by Figure 4-1.

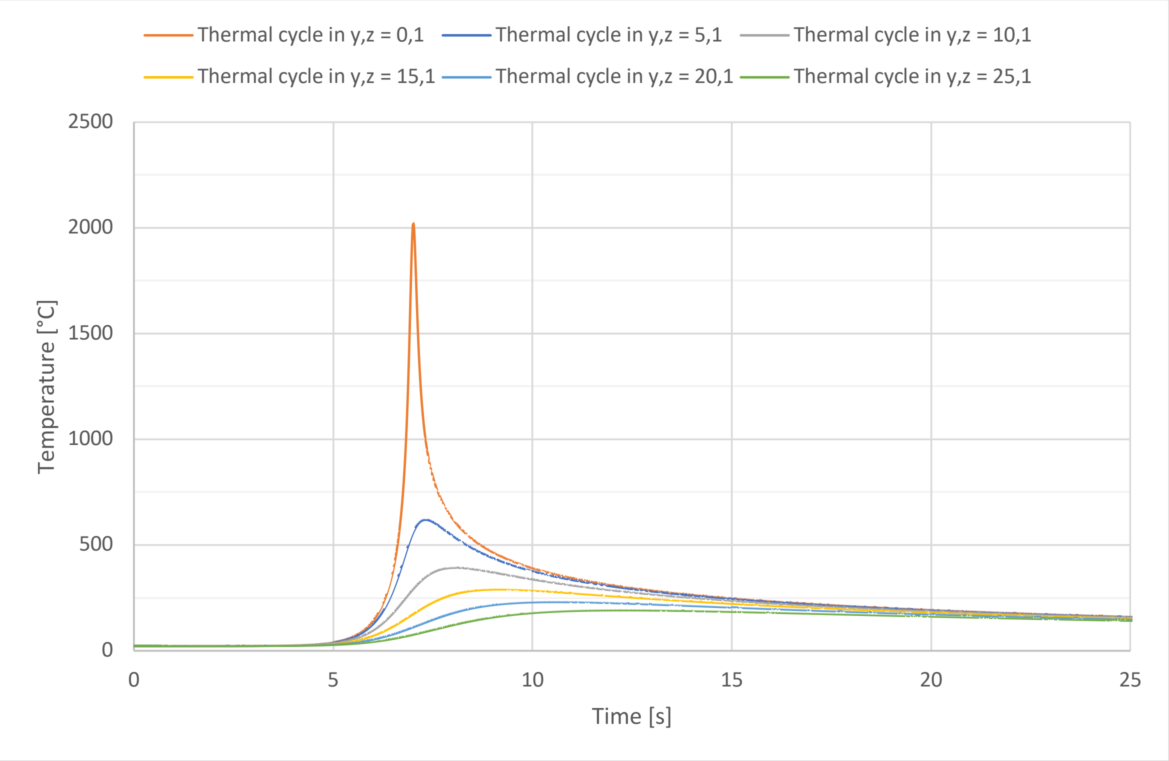

*Figure 5-1:Weld thermal cycle for selected position in y-direction across the weld.*

Figure 5-2 is a plot of the peak temperature distribution across the weld in y-direction at distances of 1, 2 and 3 mm in the z-direction of the material.

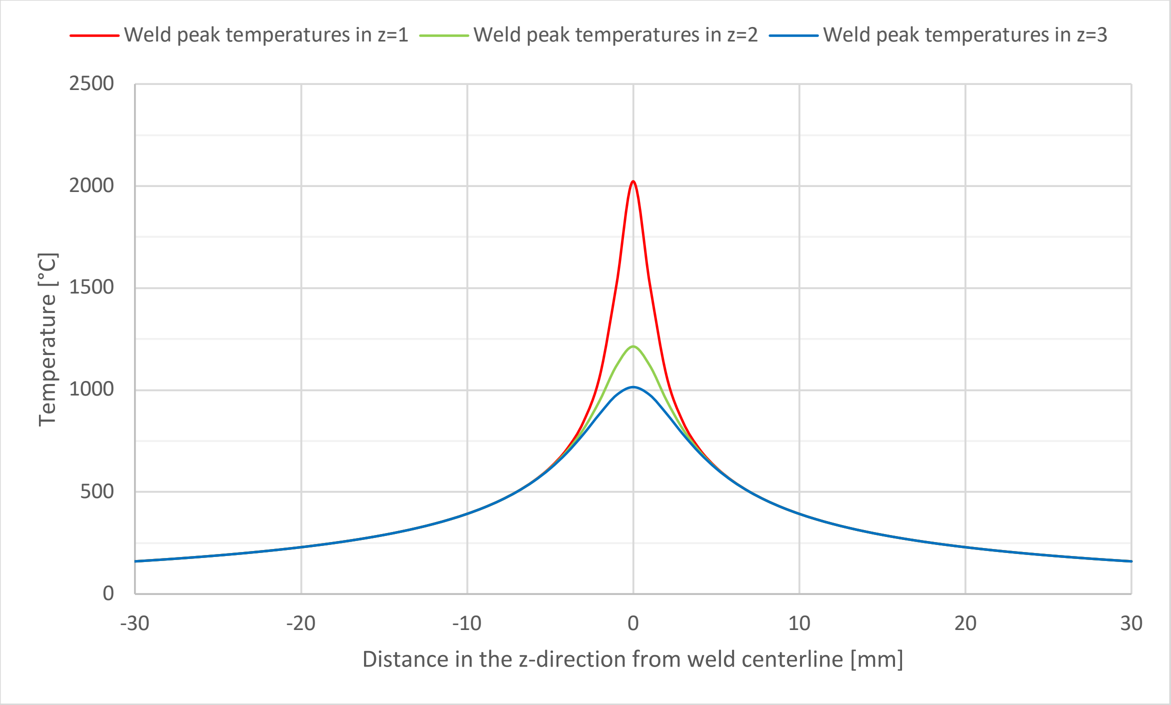

*Figure 5-2: Peak temperatures in transverse (y) direction at depths z=1, z=2 and z=3 during welding.*

## 5.2 LASER HEAT INPUT

The heat distribution for a laser in material EN AW-6082 was measured with thermocouples. First test was with a static laser on a cube. The laser was then tested on a profile from the same extrusion as described in Chapter 3.1. These tests were carried out to establish a basis for model evaluation.

### 5.2.1 Static laser heat distribution test

The peak temperatures ($T_{max}$) measured from the first run of the test are added to the illustration in Figure 5-3. The parameters set were a 4 mm spot diameter ($\phi$) and laser effect ($Q$) of 2400 W held for 10 seconds. The laser effect was increased for the second run. This caused the laser to melt the cube surface and form a pit. The pit in the surface reduced the distance between the location hit by the laser beam and the thermocouples.

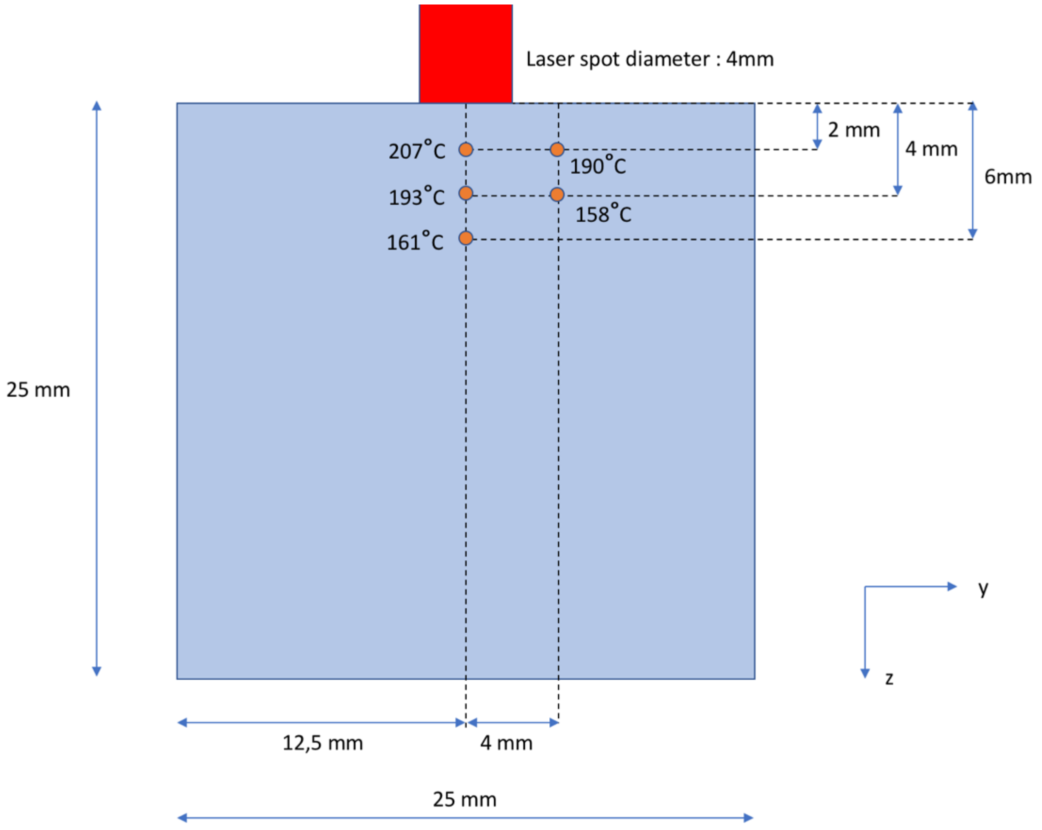

*Figure 5-3: Illustration of the static laser test on cube. The peak temperatures measured from first run have been added.*

Pit depth after each run and $T_{max}$ from the measurements of the thermocouple closest to the center point of the laser are reported in Table 5-1. The location of the thermocouple closest to the center point of the laser was y = 0 mm and z = 2 mm, directions are set by Figure 5-3.

*Table 5-1: Laser parameters with measured pit depth from melting and recorded peak temperature.*

| Run | Q [W] | ϕ [mm] | Time [s] | Pit depth [mm] | $T_{max}$ [°C] |
|---|---|---|---|---|---|
| 1 | 2400 | 4 | 10 | - | 207 |
| 2 | 3118 | 4 | 10 | 0,4 | 517 |
| 3 | 2600 | 4 | 10 | 1,0 | 759 |
| 4 | 1800 | 4 | 5 | 0,7 | 479 |

### 5.2.2 Moving laser heat distribution test

Eleven runs with the laser were done and measured by the thermocouples. Laser moving speed ($v$), $Q$ and $\phi$ were varied. Selected thermocouple measurements are plotted together with predicted thermal cycles as temperature versus time in Figures 5-4 to 5-7. The thermocouple measurements are labelled TM_(distance from laser center line in y-direction [mm]) and the predicted thermal cycles are labelled Model_(distance from laser center line in y-direction [mm]). The predict thermal cycles have been optimized with respect to the peak temperatures measured by the thermocouple located furthest away from the heat source (TM_4.16) by variating the efficiency factor ($\eta$). The model is better to predict the measured thermal cycles further away from the heat source. This is in accordance with the theory behind the model and its simplifying assumptions. Laser beam energy distribution is not accounted for, which is more important close to the heat source. The position of TM_4.16 was at y = 2.28 mm and z = 0 mm (at the profile surface).

***Q = 2400 W, ϕ = 4 mm, v = 10 mm/s***

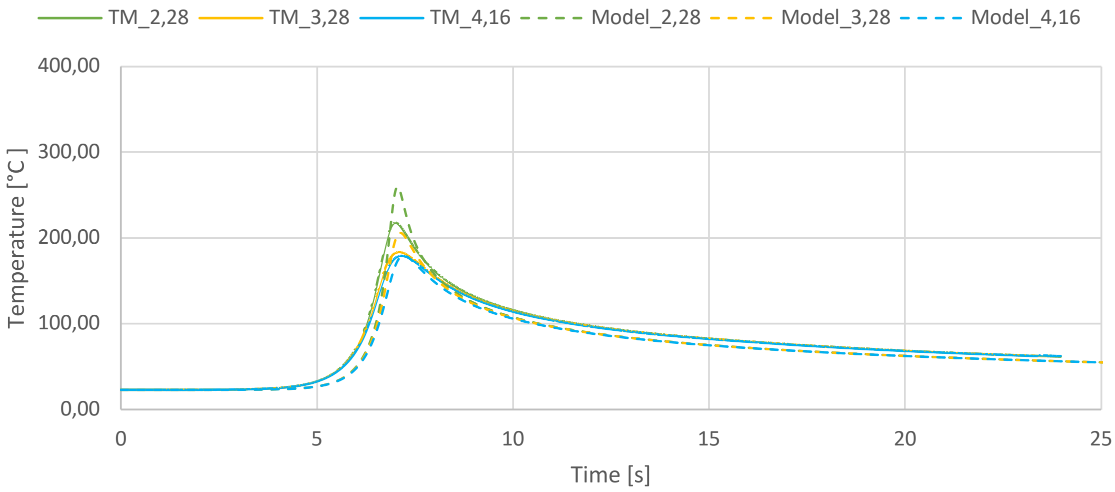

*Figure 5-4: The measured and modelled thermal cycle of run 1. η = 0,1748*

***Q = 2400 W, ϕ =4 mm, v=2 mm/s***

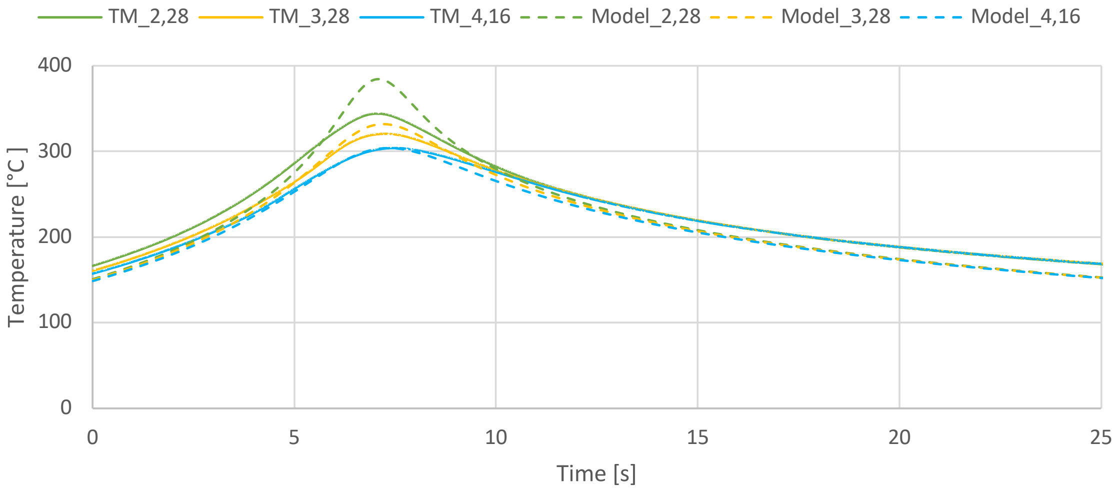

*Figure 5-5: The measured and modelled thermal cycle of run 7. η = 0,1563*

***Q = 1800 W, $\phi$ = 3 mm, v = 10 mm/s***

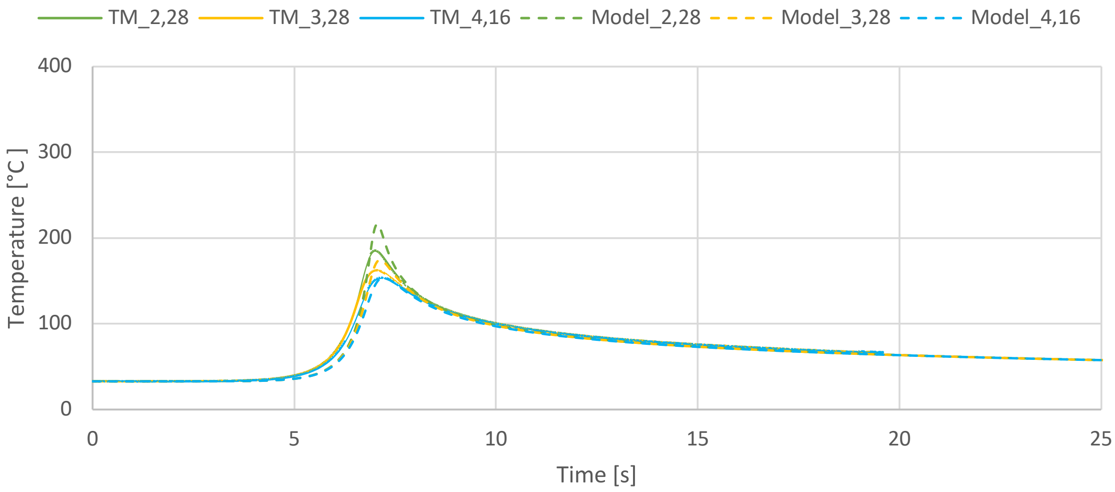

*Figure 5-6: The measured and modelled thermal cycle of run 9. η = 0,1803*

***Q = 2400 W, $\phi$ = 3 mm, v = 10 mm/s***

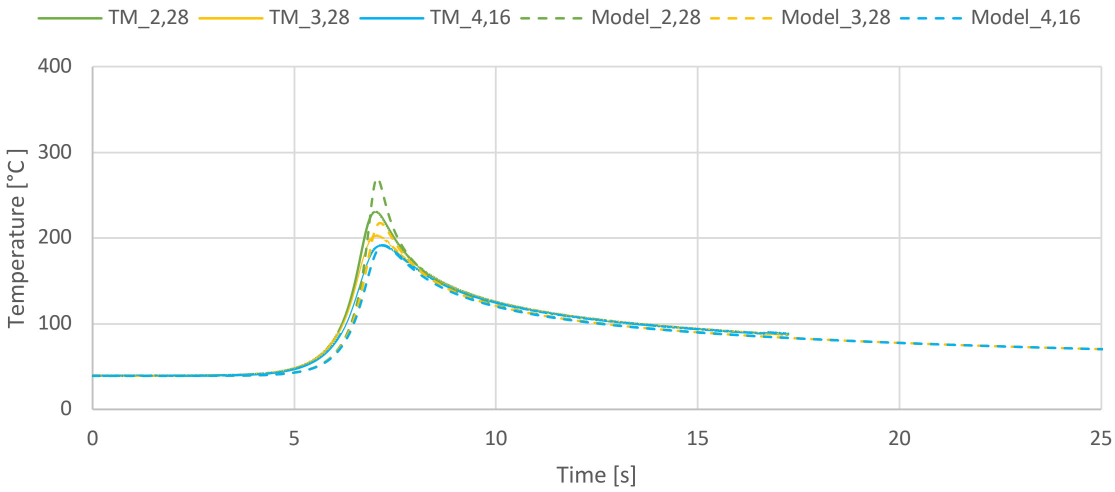

*Figure 5-7: The measured and modelled thermal cycle of run 10. η = 0,1705*

The predicted and the measured thermal cycles have good compliance for all tested laser moving speeds, as shown in Figure 5-8.

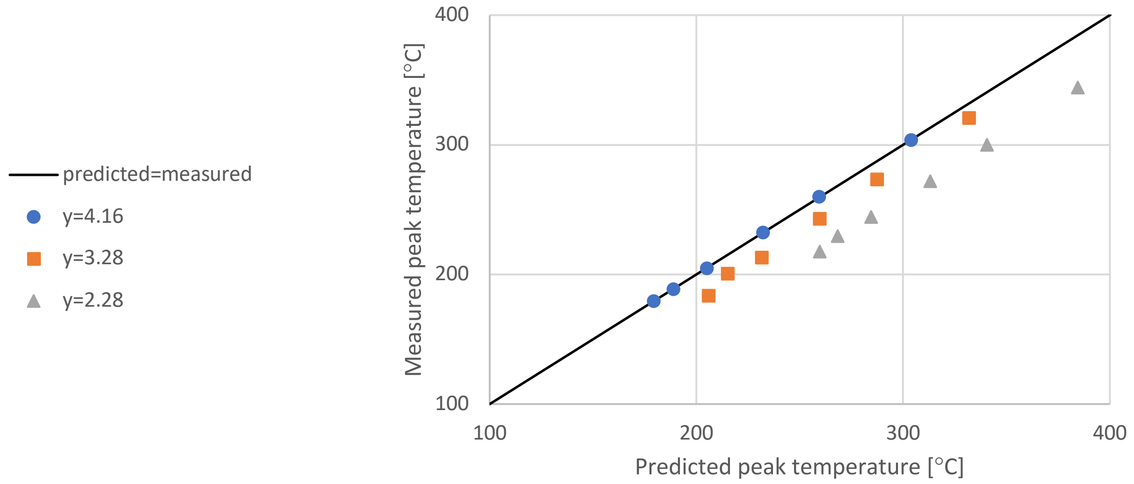

*Figure 5-8: Comparison between predicted and measured peak temperatures for varying laser movement speeds in the moving laser heat distribution test*

Laser parameters used with start temperature ($T_0$) and peak temperature ($T_{max}$), measured by TM_2.28, and the efficiency factor used for optimized predictions for TM_2.28 ($\eta_{2.28}$) and TM_4.16 ($\eta_{4.16}$) are reported in Table 5-2.

*Table 5-2: Laser parameters form each test run. The measured initial temperature ($T_0$) and max temperature ($T_{max}$). Laser efficiency factor ($\eta$) used for the predicted thermal cycles optimized with respect to the peak of the measured thermal cycle.*

| **Test Run** | **Q [W]** | **v [mm/s]** | **ϕ [mm]** | **$T_0$ [°C]** | **$T_{max}$ [°C]** | **Estimated $\eta_{2.28}$** | **Estimated $\eta_{4.16}$** |
|---|---|---|---|---|---|---|---|
| **1** | 2400 | 10 | 4 | 23,0 | 217,9 | 0,1439 | 0,1748 |
| **2** | 2400 | 10 | 4 | 29,8 | 219,8 | 0,1403 | 0,1695 |
| **3** | 2400 | 8 | 4 | 33,3 | 243,3 | 0,1415 | |
| **4** | 2400 | 8 | 4 | 34,9 | 244,4 | 0,1412 | 0,1682 |
| **5** | 2400 | 6 | 4 | 38,2 | 271,9 | 0,1412 | 0,1664 |
| **6** | 2400 | 4 | 4 | 34,9 | 299,9 | 0,1403 | 0,1622 |
| **7** | 2400 | 2 | 4 | 34,1 | 344,1 | 0,1384 | 0,1563 |
| **8** | 2400 | 10 | 4 | 34,3 | 229,5 | 0,1440 | 0,1728 |
| **9** | 1800 | 10 | 3 | 32,9 | 285,4 | 0,1501 | 0,1803 |
| **10** | 2400 | 10 | 3 | 39,1 | 230,7 | 0,1409 | 0,1705 |

### *Last run, Q = 3000 W, $\phi$ = 3 mm, v = 10 mm/s*

Last run had the highest laser energy input density. When the laser passed the thermocouples, it burned through the oxide surface layer and the beneath material started to melt. The measured temperatures from this incident were higher for the thermocouples located further away from the laser center line. These thermocouples were passed later by the laser due to their position.

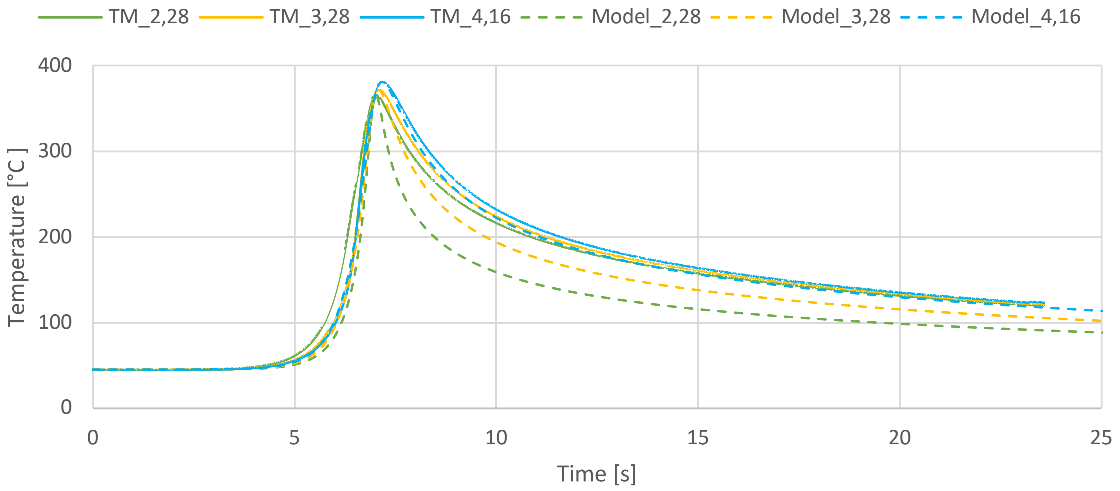

*Figure 5-9: The measured and modelled thermal cycle of run 11.* $\eta_{2,28} = 0{,}1892$ $\eta_{3,28} = 0{,}2495$ $\eta_{4,16} = 0{,}3005$

An image taken after this laser run is presented in Figures 5-10.

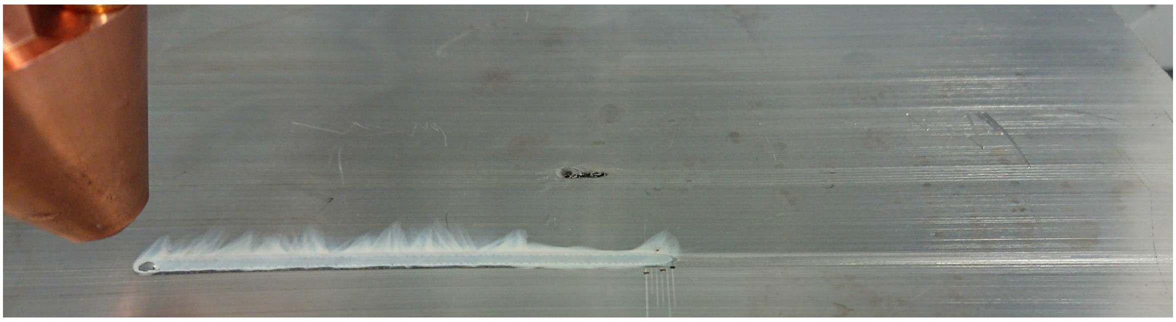

*Figure 5-10: Image of the last run by moving laser on profile. The laser burned through the surface oxide layer and the material started to melt.*

The sudden beginning of the melting may be explained by heating of the whole plate, and at one point the accumulated energy is high enough to cause melting. The peak temperatures and efficiency factors from this last run are presented in Table 5-3. The melting had an increased effect on the material's heat absorption.

*Table 5-3: Peak temperatures and efficiency factors used to estimate the three thermal cycles measured at different positions in the profile for run 11.*

| Thermocouple distances from laser centreline | Peak temperature | $\eta$ |
|---|---|---|
| **2.28 mm** | 365.6 | 0.1892 |
| **3.28 mm** | 371.7 | 0.2495 |
| **4.16 mm** | 381.1 | 0.3005 |

## 5.3 MICROSTRUCTURE

### 5.3.1 Base material microstructure

The profile microstructure is presented in Figure 5-11 to show the received state of the base material. Extruded direction of the profile is the horizontal direction in the figure and the thickness is vertical. The fibrous extruded microstructure is evident. The thickness of the specimen is 3.6 mm, while the recrystallized surface layer has a thickness of 0.14 to 0.17 mm, measured in Figure 5-11. The microstructure shows good production quality.

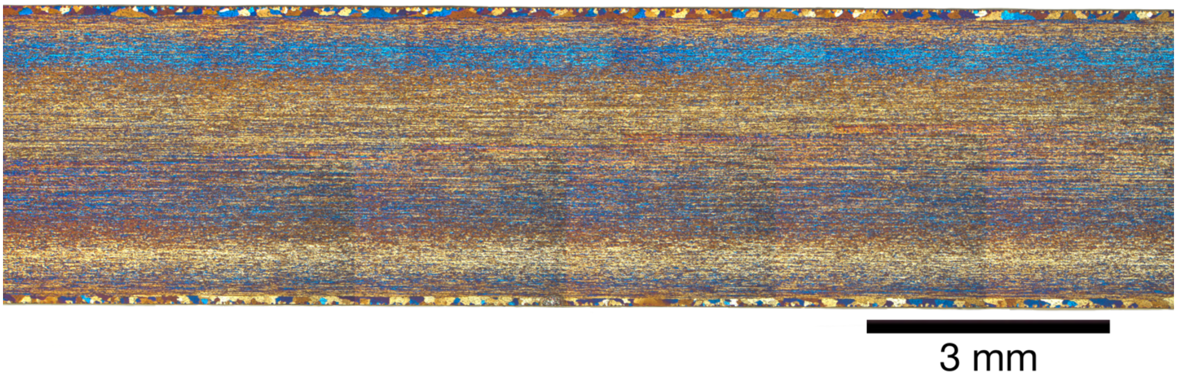

*Figure 5-11:Microstructure of the base material in the direction transverse to the extrusion.*

### 5.3.2 Weld Microstructure

Microstructural changes across the specimens due to the thermal cycle given by weld and laser are shown in Figures 5-12 to 5-16.

***Reference***

Figure 5-12 shows the microstructure of the welded reference specimen where no laser treatment was given. The fibrous microstructure of the extrusion is clear in the center of the profiles on both sides of the weld. An increase in the thickness of the recrystallized surface layer may be observed nearby the weld. In the fusion zone an as-cast microstructure is seen from the occurred melting and solidification by the welding. Filler material used was AA5183.

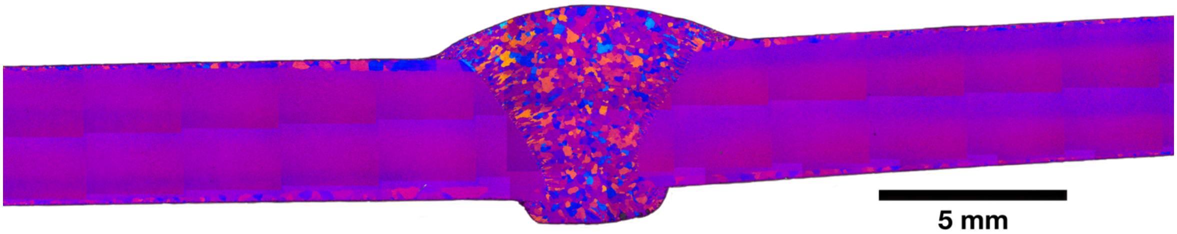

*Figure 5-12: Image of the microstructure of the Reference specimen.*

### Specimen A

Figure 5-13 shows the microstructure of Specimen A, which is laser heat-treated on both sides of the weld. Melting has occurred through the profiles on both sides, resulting in deformation. The solidified microstructure of the laser heat treatment on the left side is merged together with the weld microstructure. Pores are observable in the weld, marked with white circle in Figure 4-18.

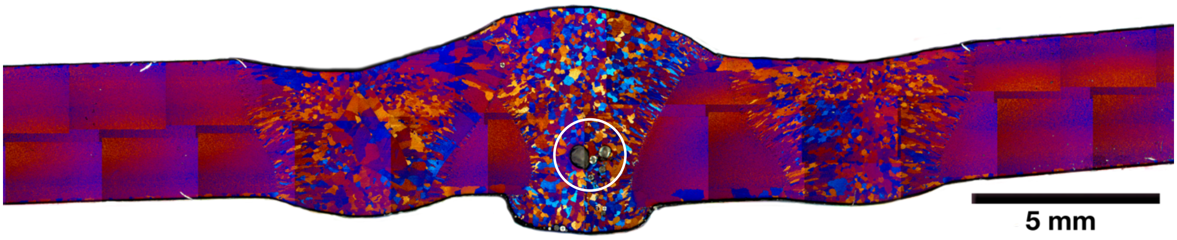

*Figure 5-13: Image of the microstructure of Specimen A.*

### Specimen B

Figure 5-14 shows the microstructure of Specimen B. The laser heat treatment is melted through the profile. Specimen A is less misshaped than Specimen A. Some misalignment of the welded profiles is observed.

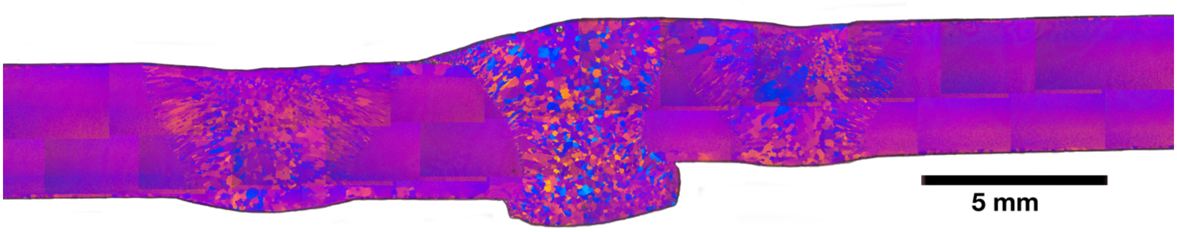

*Figure 5-14: Image of the microstructure of Specimen B.*

***Specimen C***

Figure 5-15 shows the microstructure of Specimen C. The laser moving speed ($v$) was increased for Specimens C and D, resulting in less heat input from the laser. Hence, the melting observed is severely reduced and doesn't go through the profile. The depth of the melting zones is 1.21 mm on the left side and 0.58 mm on the right side.

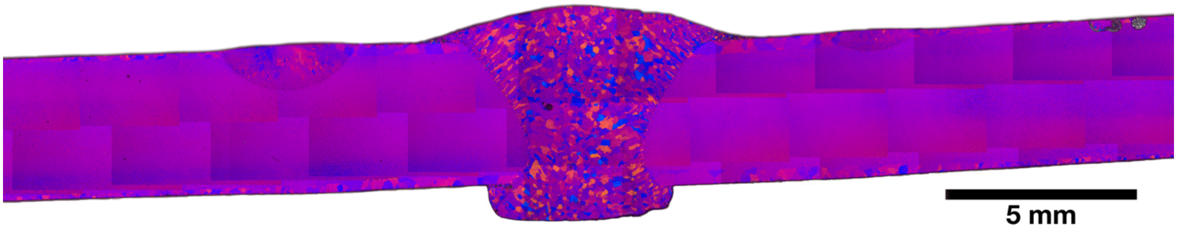

*Figure 5-15: Image of the microstructure of Specimen C.*

***Specimen D***

Figure 5-16 shows the microstructure of Specimen D. The melting has reached approximately half way through the profile on both sides. The melting pool depth is measured to 2.1 mm. Pores can is observed in the surface of the right melting pool, marked with a yellow ring.

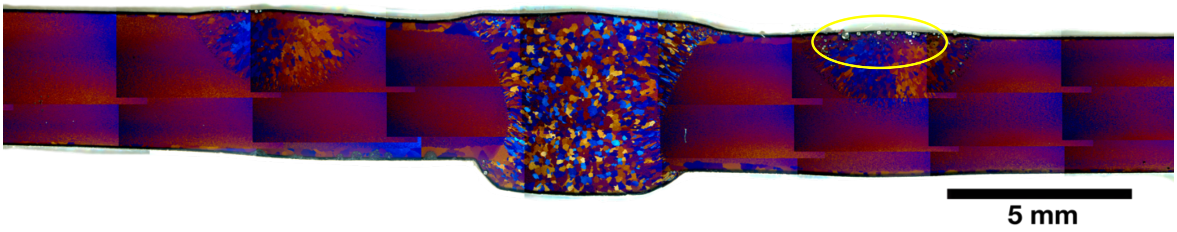

*Figure 5-16: Image of the microstructure of Specimen D.*

## 5.4 WELD THERMAL CYCLE IMPACT ON HAZ

The base material used in this experiment obtain high strength and hardness due to a high density of $\beta''$-particles which forms uniformly in the matrix during artificial aging. However, these precipitates are thermodynamically unstable at welding conditions [29]. The heat distribution model has been used to map the peak temperatures across the weld. These has been used to analyse how the weld thermal cycle effects the mechanical properties. The predicted weld peak temperatures distribution and the Reference specimen's hardness profile across the weld are plotted in Figure 5-17.

The hardness of the base material starts to decrease 18 mm from the weld center line, which corresponds well to where the temperature exceeds 250°C. This is marked with black dotted line in Figure 5-17. The reduction in base material hardness is caused by dissolution of smaller $\beta''$-precipitates and coarsening of bigger $\beta''$-precipitates. This is activated when the material temperature exceed 250°C [29]. Kinetics increase with increasing temperature. Hence, hardness continuously decreases until a minimum is reached at 8 mm from the weld center line. From 8 mm towards the weld center line, the hardness starts to increase. At this location the weld temperatures exceed 480°C. This is marked with a black dotted line. When the equilibrium solvus ($T_{eq}$) is exceeded, solutioning of small and larger MgSi-phases becomes dominating. Hence, the material obtain strength by solid solution. The hardness profile increase until 3 mm from the weld center. The material has melted within 3 mm and the hardness is decreased again. This is typical and represent the as-cast properties of the feeding wire material (AA5183). Melting temperature of the base material is 585-650°C. 5 mm from the weld center line, the predicted temperature distribution exceeds 600°C. However, required latent fusion heat is not accounted for in the Equation the model is based on. In addition, increased heating has a tendency to increase the melting temperature. The weld microstructure is presented in Figure 5-18 with distances indicated. The measured hardness is typical for a welded Al-Mg-Si alloy. A reduction in hardness of 30-40% is expected.

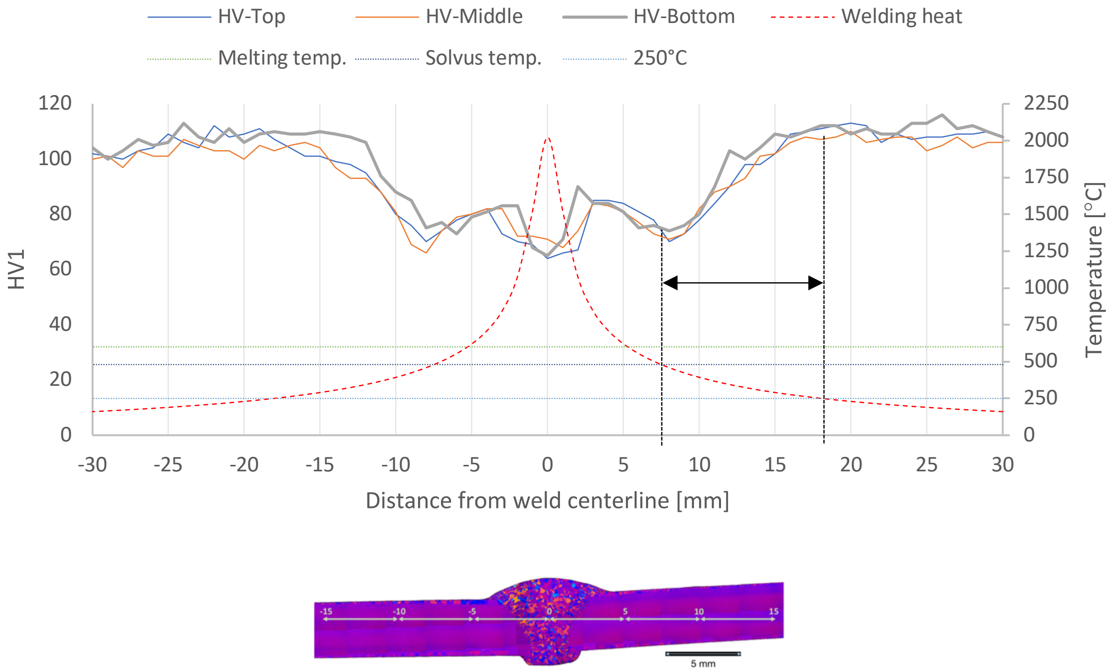

*Figure 5-17: Hardness measurements of the Reference specimens plotted together with the peak temperature distribution from the modelled weld thermal cycle. A miniature version of Figure 5-2 has been added for scale*

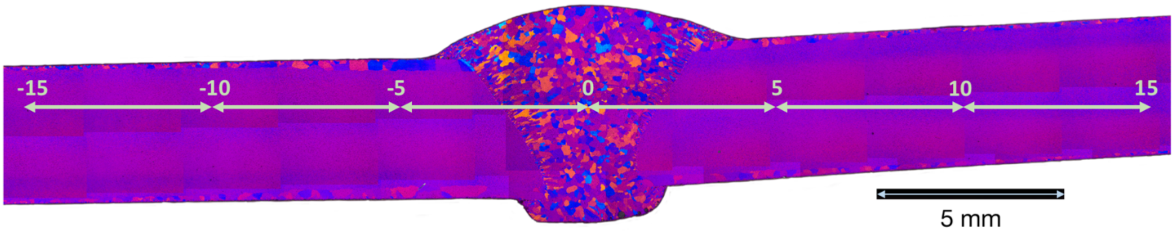

*Figure 5-18: Microstructure of the Reference specimen with scaling system.*

## 5.5 HARDNESS PROFILES

Figures 5-19 to 5-23 shows measured hardness profiles across the weld and laser heat treated area for all the specimens. The same samples used for microscopy have been used for hardness measurements and has been extracted from the spare material from the tensile test specimens. Hardness measurements are useful to illustrate how the precipitates in the material have reacted to the heat treatment and indicate the $b_{haz}$. Hardness measurements are a low-cost and efficient way to map the materials mechanical properties as it is strongly related to the materials strength.

### *Reference specimen*

The obtained hardness profiles of the Reference specimen, which has not been laser treated after welding, are presented in Figure 5-19. The minimum hardness value is marked. The minimum hardness is essential to the load bearing capacity of the material. For a welded Al-Mg-Si alloy a tensile test fracture would initiate and follow the weakened HAZ rather than the unaffected base material or weld if there are no pores and other flaws.

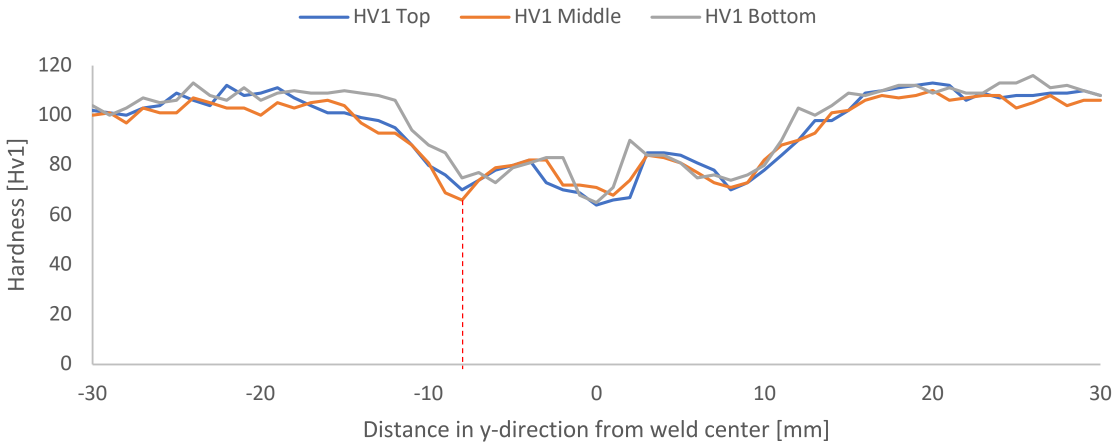

*Figure 5-19: Hardness measurements across the weld on the Reference sample.*

### *Specimen A and B*

The hardness profiles of Specimens A and B are presented in Figures 5-20 and 5-21, respectively. The minimum hardness and the zones melted by the laser are marked. The laser melted through the profile thickness for both specimens. A too hot laser treatment was applied which has resulted in major deterioration to the base material unaffected by the welding. The minimum hardness is also reduced compared to the Reference specimen. The melted material has lost its thermomechanical history. Nevertheless, higher minimum hardness is observed in the laser melted metal than in the new laser treatment HAZ. The extent of the new laser HAZ is increased compared to the weld HAZ. For profile A, it was only possible to fit two series (top and bottom) into the sample due to its deformed geometry. Here it can be observed that the minimum hardness of the HAZ has moved from 8 mm (Reference specimen) to 18 mm away from the weld center line. The laser treatment has resulted in similar response for Specimens A and B. Minimum hardness has moved to 22 mm from the weld center line for Specimen B, presented in Figure 5-21.

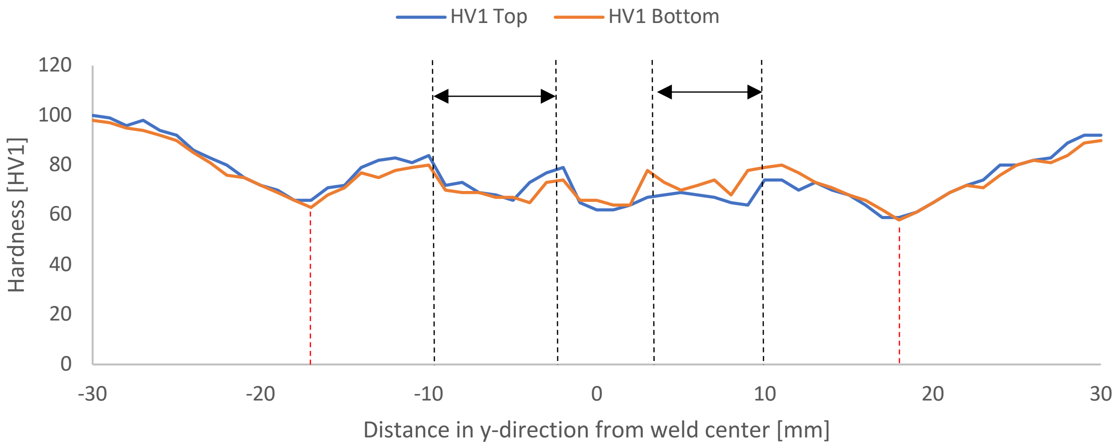

*Figure 5-20: Hardness profile for Specimen A. Minimum hardness and melted area is marked.*

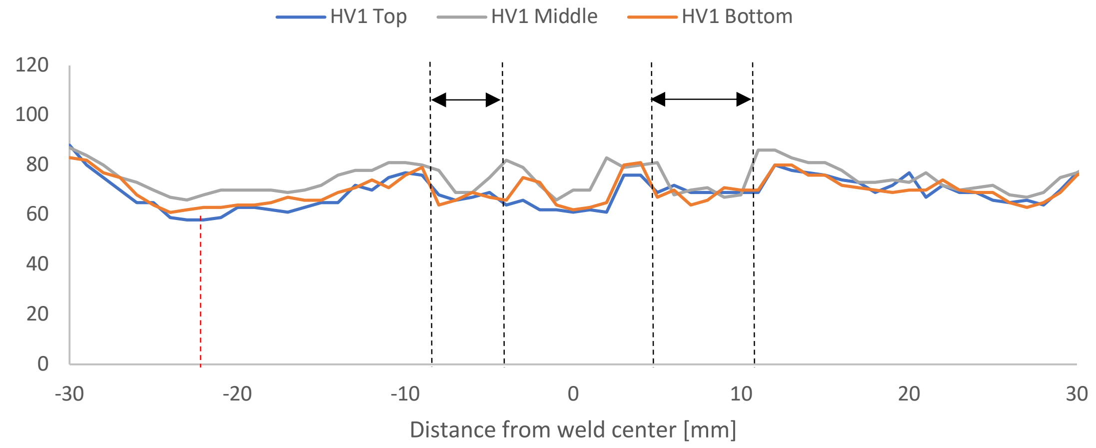

*Figure 5-21: Hardness profile for Specimen B. Minimum hardness and melted area are marked.*

### *Specimen C*

It should be noted that this was the specimen which had smallest area of melting from the laser heat treatment. The hardness profile of specimen C has been presented in Figure 5-22. Here, the minimum hardness has been marked. The hardness profile is quite similar compared to the Reference specimen. The minimum hardness improved from 66 HV1 to 70 HV1 compared to the Reference specimen. The weld thermal cycle at this point in the weld may have given reduced decrease of hardness. Or else has the laser treatment given the HAZ solution treatment and resulted in improved hardness.

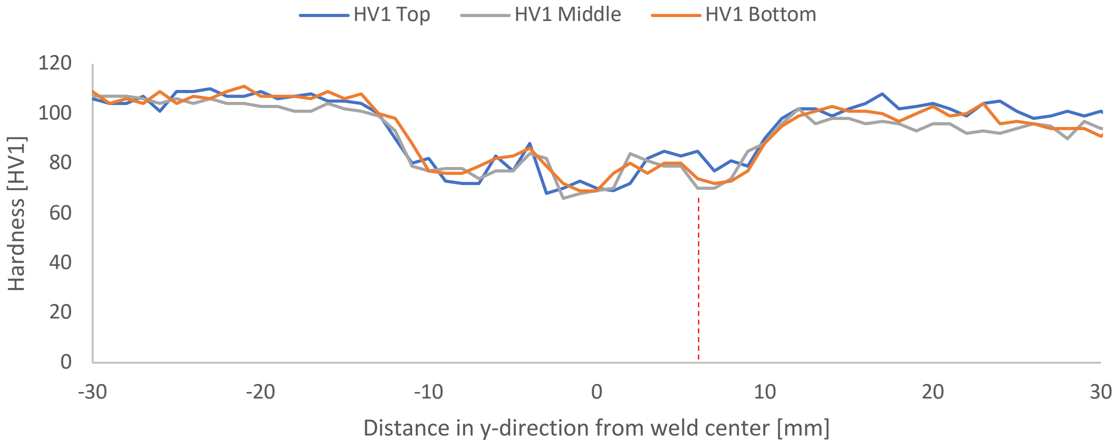

*Figure 5-22: Hardness profile for Specimen C. Minimum hardness is marked.*

***Specimen D***

In Figure 5-23, the hardness profile of Specimen D is presented, with marks for minimum hardness and melted zones. The hardness has decreased for the melted material in the marked zones for HV1 Top and HV1 Middle. For the unmelted material, HV1 Bottom, the hardness has increased in the same zone. This is evidence of solution treatment from the laser treatment. The hardness has increased by minimum 6 HV1 compared to the untreated Reference specimen at 8 mm from the weld center line. A possible explanation to the hardness increase is solution treatment and hardening by elements in solid solution. As it was for Specimens A and B, the extent of the new HAZ from the laser treatment is longer for Specimen D. In comparison, melting for Specimen D is more severe than for Specimen C as observed by microscopy. The laser treatment parameters used for Specimens C and D were equal, but more melting occurred for Specimen D. This indicates that the parameters used has been on the limit for melting.

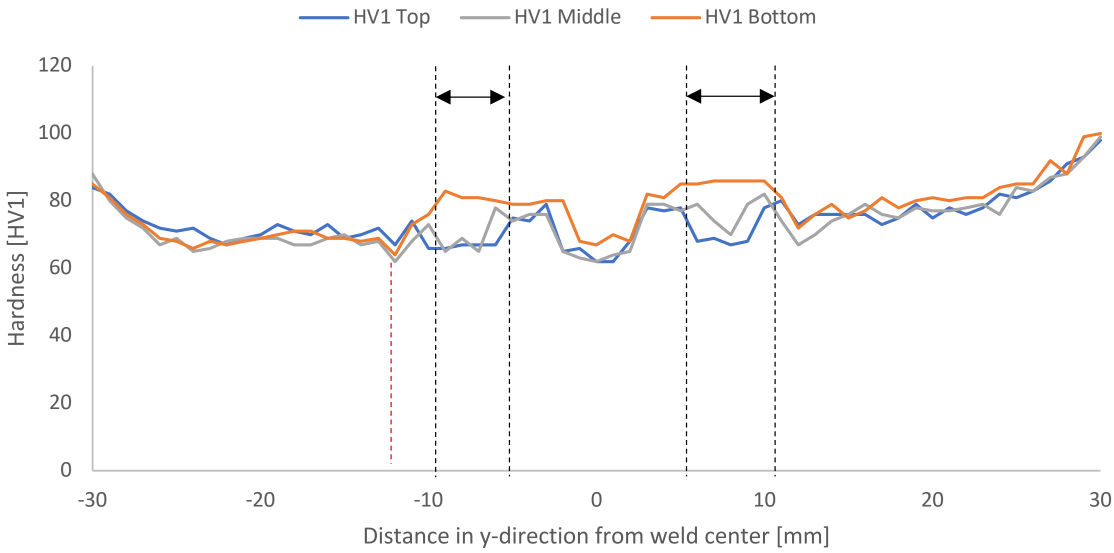

*Figure 5-23: Hardness profile for Specimen D. Minimum hardness and melted area are marked.*

### 5.5.1 Summary of the hardness

A summary for the minimum hardness (Min. H) for all the specimens are presented in Table 5-4. To link minimum hardness to load bearing capacity, Equation 2-8 has been used to calculate yield strength corresponding to the Min. H. Form the Table, it can be seen how the location of minimum hardness has moved for Specimens A, B and D. According to hardness measurements, the physical properties is improved by the laser treatment for Specimen C.

*Table 5-4: Summary of the minimum hardness value of each specimen and the location of it in the weld. Strength corresponding to the minimum hardness $\sigma_{min}$ is presented.*

| | **Ref** | **A** | **B** | **C** | **D** |
|---|---|---|---|---|---|
| **Min. H [HV1]** | 66 | 58 | 58 | 70 | 62 |
| **Distance from weld [mm]** | 8 | 18 | 22 | 6 | 12 |
| **$\sigma_{min}$ [MPa]** | 150 | 126 | 126 | 162 | 138 |

## 5.6 TENSILE TEST

Instead of extensometer, which is normal, digital image correlation (DIC) was used to measure specimen strain during the tensile testing. Testing was performed at SINTEF Materials and Chemistry. Stress-strain curves and movies with strain visualization has been made by post processing of the DIC data.

### 5.6.1 Stress-strain curves

Stress-strain curves from the tensile testing of all specimens are presented in Figure 5-24. The Reference specimen yielded at highest stress. Hence, yield stress has been reduced for all laser treated specimens. Tensile stress has also been reduced, but there is a big difference between Specimens; A and B, and Specimens; C and D. The laser moving speed was increased for the laser treatment of C and D, which reduced the degree of melting. Increased plastic strain after the yield point is observed for the Specimens C and D, which were treated by laser.

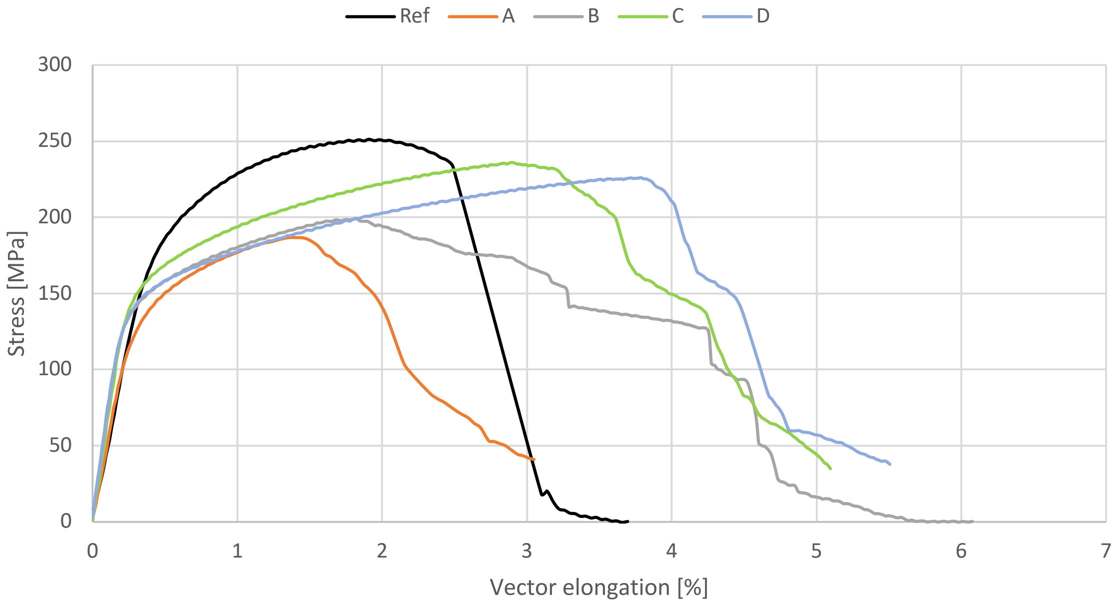

*Figure 5-24: Strain-stress curves for the tensile tests.*

The specimens yield strength ($R_{p0,2}$), tensile strength ($R_m$) and stress at 0,5 % strain ($R_{t0,5}$) are presented in Figure 5-25.

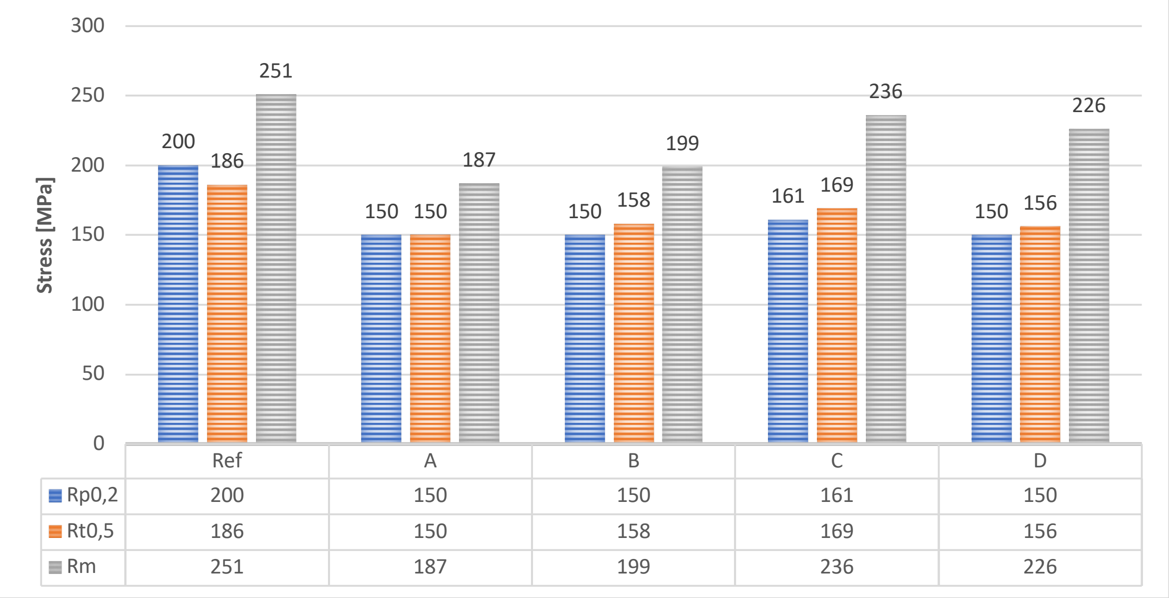

| | Ref | A | B | C | D |
|---|---|---|---|---|---|
| Rp0,2 | 200 | 150 | 150 | 161 | 150 |
| Rt0,5 | 186 | 150 | 158 | 169 | 156 |
| Rm | 251 | 187 | 199 | 236 | 226 |

*Figure 5-25: Strength values from the tensile tests.*

All specimens have strength values higher than the minimum values listed in the Eurocode 9 standard. Yield strength ($f_{0,HAZ}$) of the welded zone of 125 MPa and tensile strength ($f_{u,HAZ}$) of 185 MPa are stated. The best strength values are obtained by the Reference specimen. Yield strength is 60 % higher than $f_{0,HAZ}$ and tensile strength is 35.7 % higher than $f_{u,HAZ}$. Compared to the Reference specimen, the strength of all the laser treated specimens have decreased. An overview of the reduction factors with respect to the Reference specimen values are given in Table 5-5.

*Table 5-5: Listed strength values for the Reference specimen and reduction factors for laser treated specimens.*

| | **Ref** | **A** | **B** | **C** | **D** |
|---|---|---|---|---|---|
| **$R_{p0,2}$** | 200 MPa | 0.75 | 0.75 | 0.81 | 0.75 |
| **$R_{t0,5}$** | 186 MPa | 0.81 | 0.85 | 0.91 | 0.84 |
| **$R_m$** | 251 MPa | 0.75 | 0.79 | 0.94 | 0.90 |

Ductility is very important in terms of fracture resistance, which also is important for structural components. Toughness is a measure of the material's resistance to fracture. The toughness of the specimens has been calculated from Equation 2-10 and reported in Table 5-6.

*Table 5-6: Toughness of the specimens*

| | **Ref** | **A** | **B** | **C** | **D** |
|---|---|---|---|---|---|
| $U_T$ | 5,61 | 2,63 | 5,03 | 6,47 | 7,13 |

The elongation at maximum stress ($A_{gt}$) is reported for all specimens in Figure 5-26. Increased ductility has been observed for Specimens C and D. The elongation has doubled for Specimen D. This is remarkable, as it shows that the specimen's ability to withstand plastic deformation without fracturing has improved. An increase of 60 % in $A_{gt}$ was experienced for Specimen C. Specimens A and B have shown a decrease in $A_{gt}$. All laser treated specimens have a ductile fracture, where the specimens are severely strained without fracturing after the maximum load is reached.

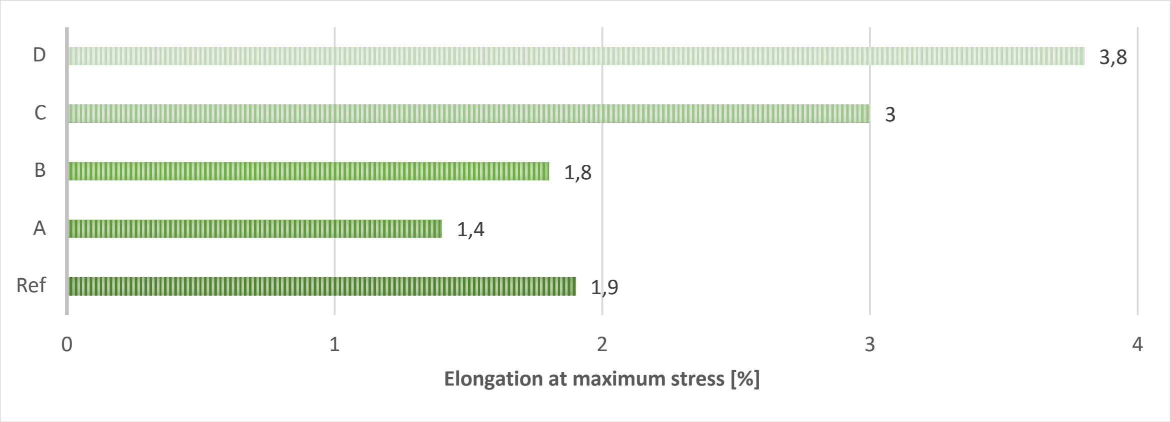

*Figure 5-26: Nominal elongation at maximum load for all specimens.*

### 5.6.2 Fracture propagation

Fracture propagation is shown by images from the straining session. Images from the beginning of the tensile test beginning, fracture initiation and point of total fracture are attached for all five specimens. Images extracted from films made by DIC post processing are added as well. The films show straining of the specimens with added visual effects to display the magnitude of the straining. For the Reference specimen has the colouring scale for strain been set from 0 - 20 % strain. The colouring scale has been automatic, which means that it is adjusting during the strain session. This give a better insight to the early small-scale strain occurring. The pictures have been numbered in chronological order.

***Reference specimen***

The fracture of the Reference specimen occurred from the middle of specimen. The fracture initiation is marked in Figure 5-27.

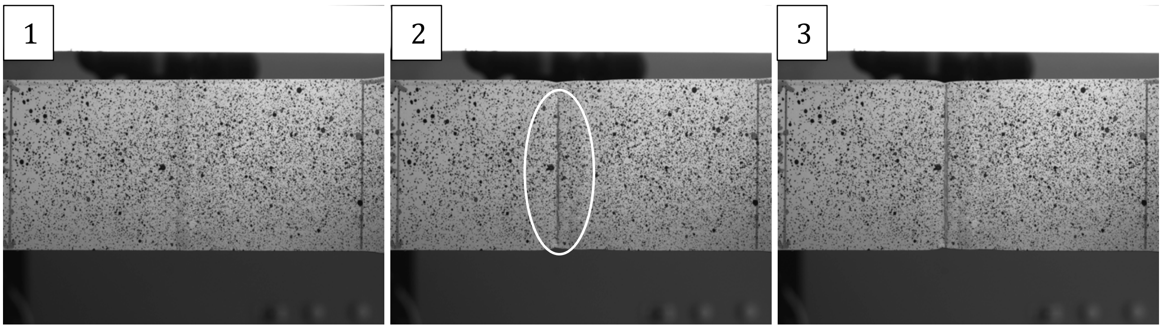

*Figure 5-27: Fracture propagation of the Reference specimen by pictures from the test's beginning, fracture initiation and at total fracture.*

From the DIC post processing presented in Figure 5-28 the strain localisation may be observed. The strain developed in the HAZ as expected.

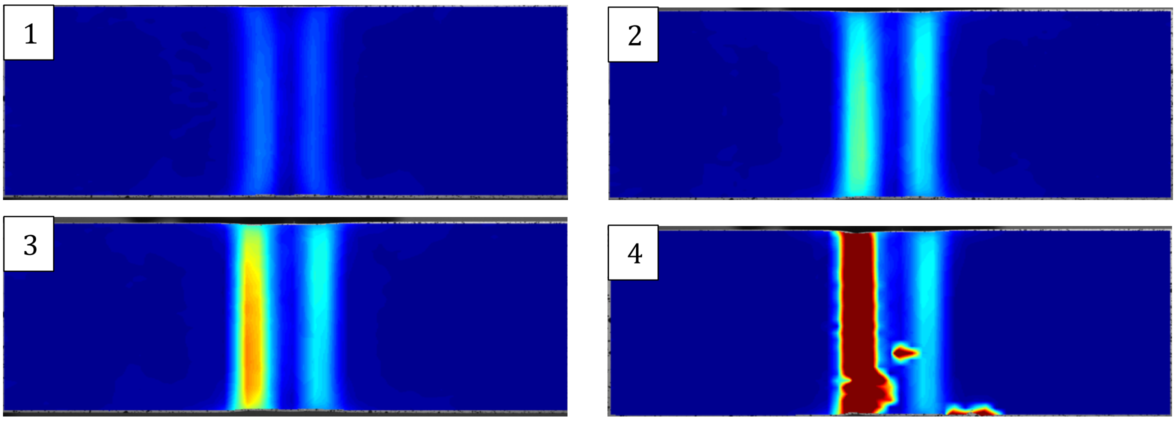

*Figure 5-28: DIC post processing which show strain development for the Reference specimen.*

***Specimen A***

Two cracks developed which the fracture of Specimen A grew from. The fracture has a serrated formation as seen in Figure 5-29, picture 3. The DIC post processing presented in Figure 5-30 show the strain propagation more clearly.

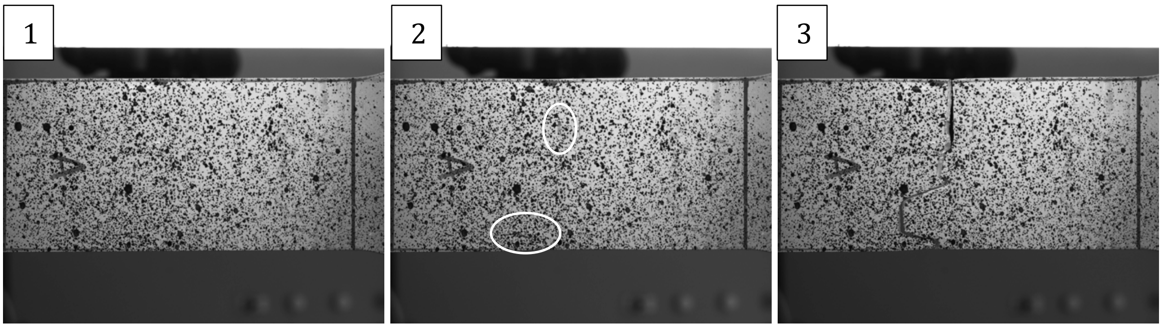

*Figure 5-29: Fracture propagation of Specimen A by pictures from the test's beginning, fracture initiation and at total fracture.*

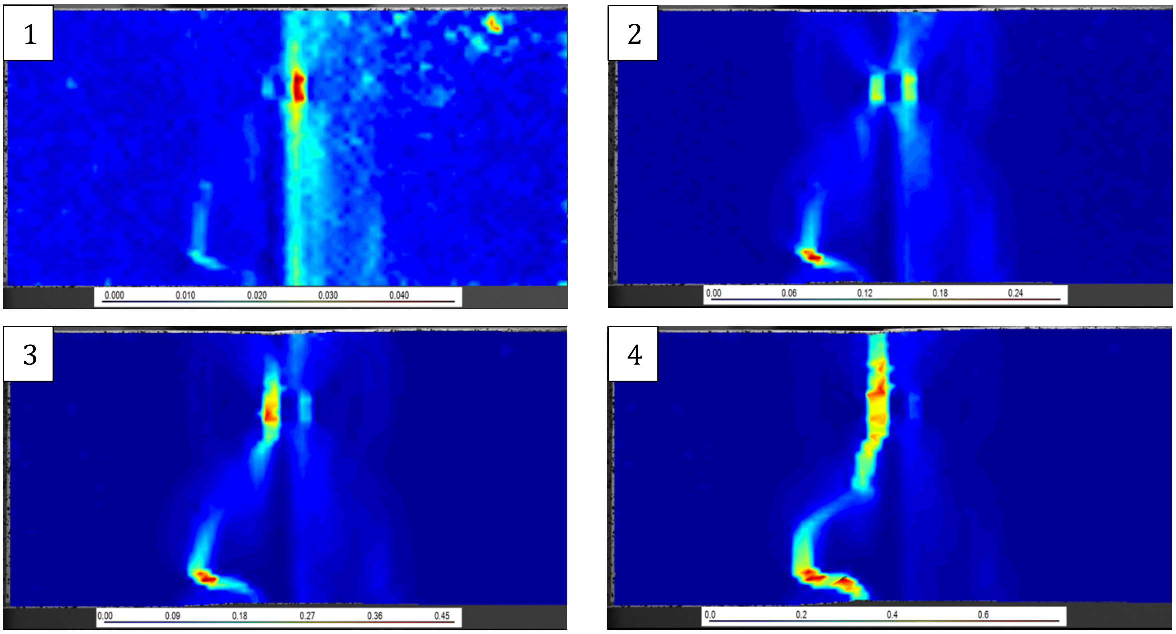

*Figure 5-30: DIC post processing which show strain development for Specimen A.*

### *Specimen B*

For specimen B the fracture developed from a crack initiated in a corner of the laser treatment pattern. This can be observed in Figures 5-31 and 5-32

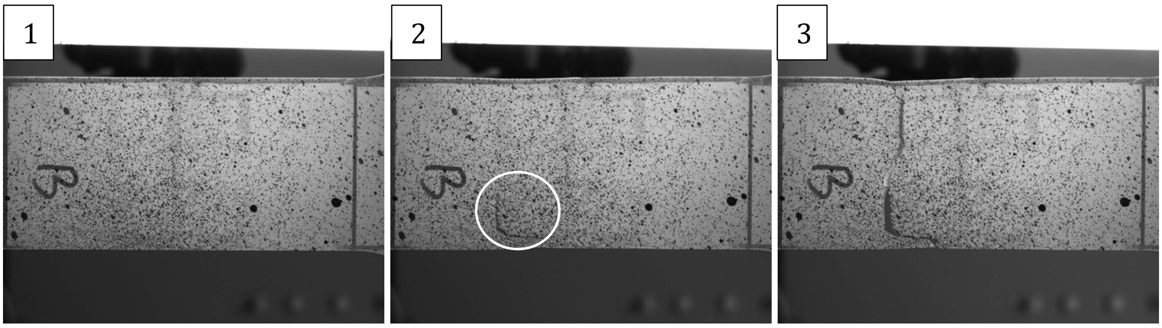

*Figure 5-31: Fracture propagation of Specimen B*

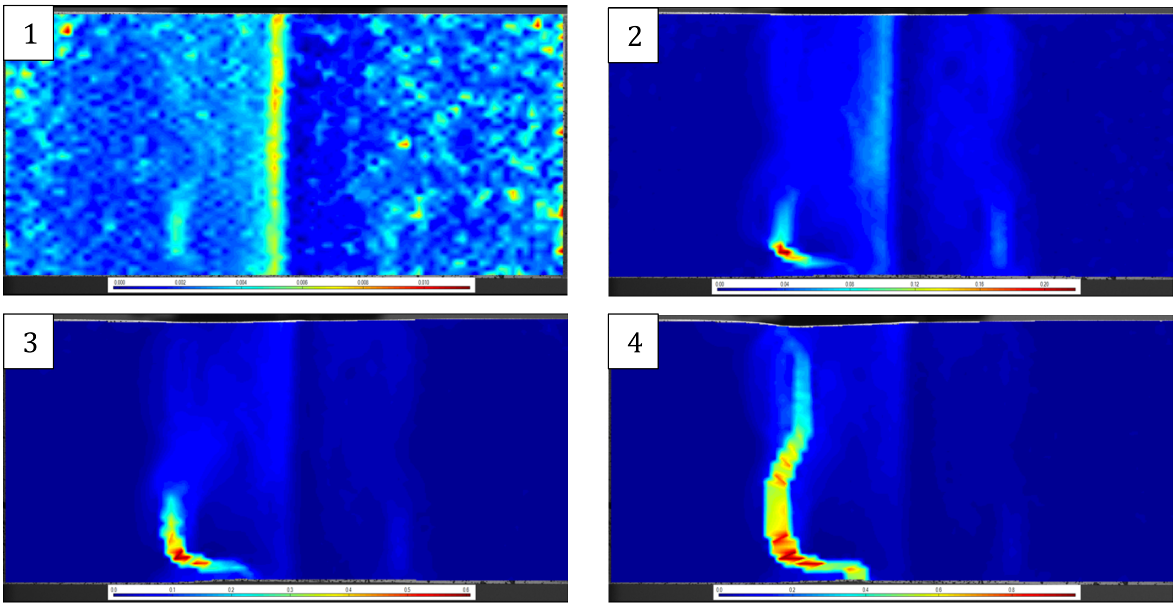

*Figure 5-32: DIC post processing which show strain development for Specimen B.*

### *Specimen C*

The crack initiation point is on one inner corner of the pattern towards the weld, marked with white ring in Figure 5-33. Compared to the Reference specimen, the fracture has still initiated and propagated in HAZ, but a more ductile fracture is observed. The strain is spread over a larger area for specimen C following the laser treatment pattern, as may be seen in Figure 5-34.

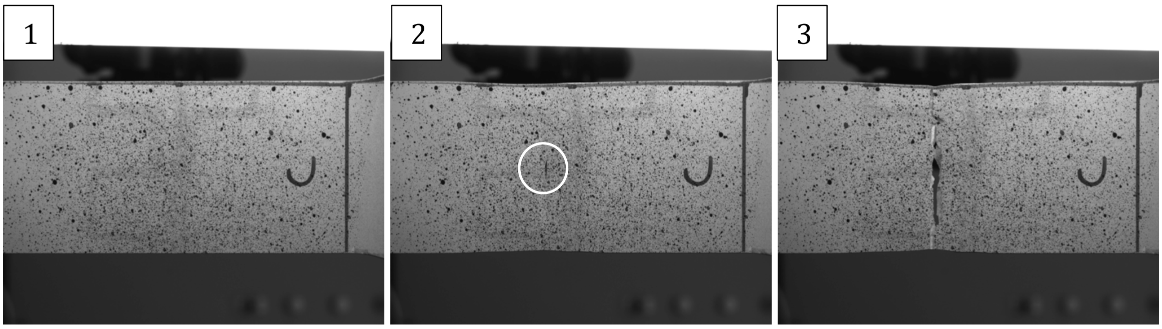

*Figure 5-33: Fracture propagation of Specimen C*

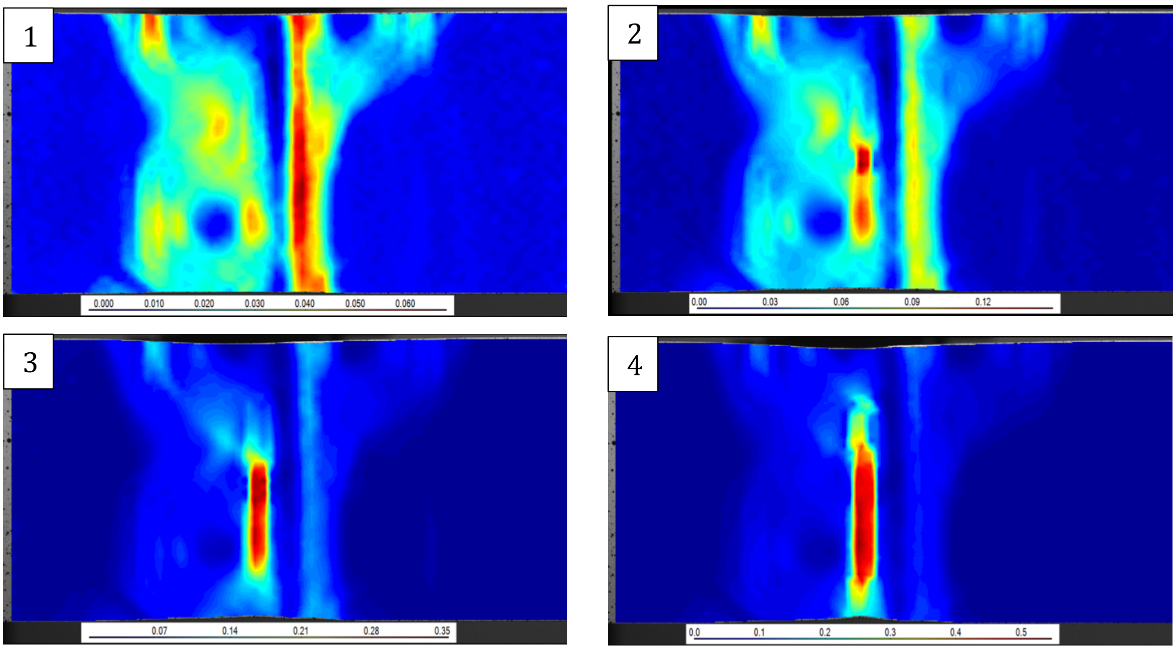

*Figure 5-34: DIC post processing which show strain development for Specimen C.*

***Specimen D***

The fracture initiation and growth for Specimen D is similar to Specimen C. The crack initiation is at one corner of the laser treated pattern, towards the weld, marked with white ring in Figure 5-35. The strain has been more evenly distributed to both sides of the weld, as seen in Figure 5-36, compared to Specimen C.

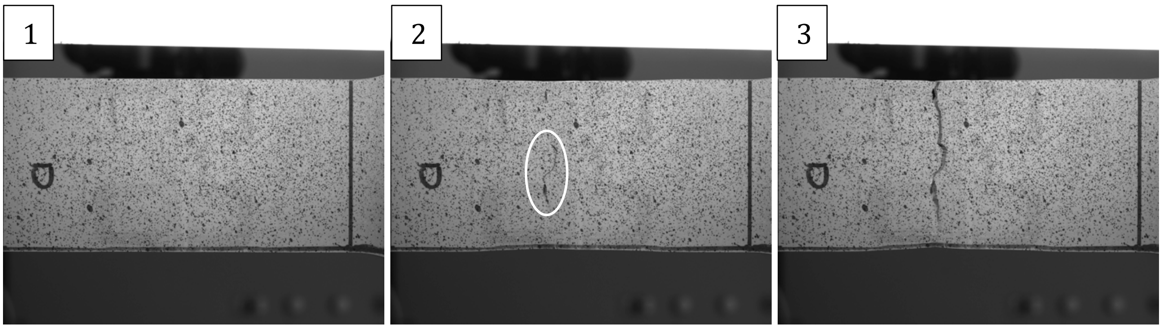

*Figure 5-35: Fracture propagation of Specimen D*

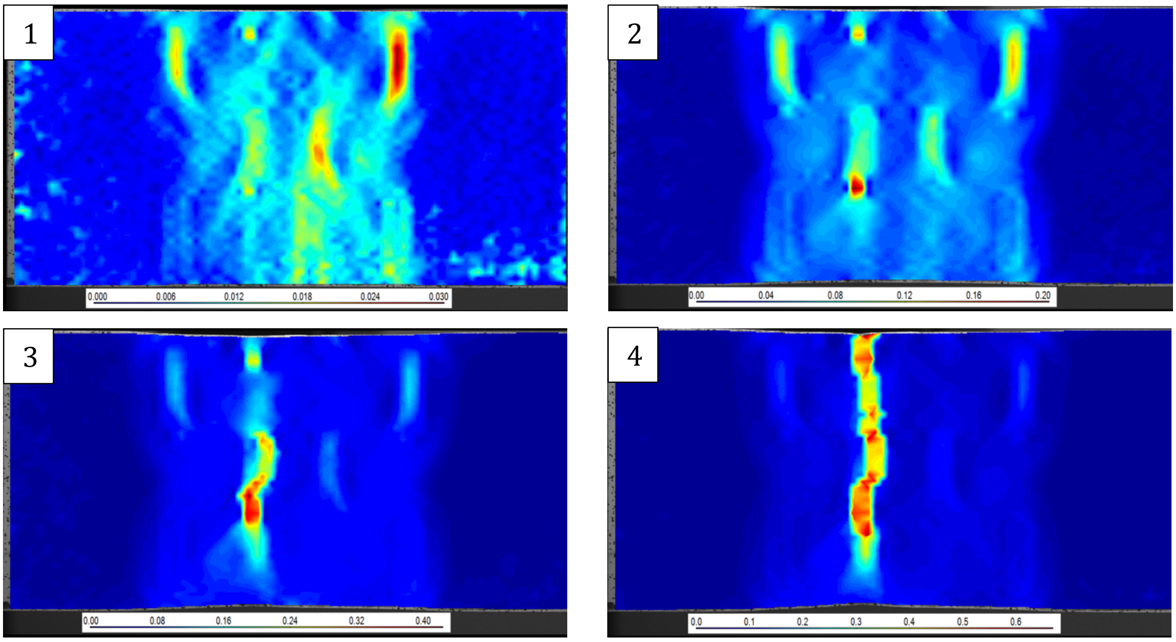

*Figure 5-36: DIC post processing which show strain development for Specimen D.*

# 6 DISCUSSION

## 6.1 THE DETERIORATION IN HAZ BY THE WELD THERMAL CYCLE

The equation used for creating the heat distribution model (Equation 2-4) has in several studies been proven reasonable for welding. Still it is important to be aware of the limitations when applying the model. Predictions of the weld thermal cycle should be restricted to positions well outside the fusion zone where the simplifying assumptions are less impacting. The model has predicted a temperature distribution which agrees well with the extent of HAZ ($b_{haz}$) measured by hardness. However, for a more reliable prediction of HAZ extent, microstructure models, such as NaMo, should be coupled together with the complete predicted thermal history form casting to welded product.

### 6.1.1 Ideal thermal cycle for welding

The model can be applied to determine an ideal thermal cycle by altering the welding parameters; arc voltage, welding current and welding moving speed. In addition, plate thickness is essential for the predicted thermal cycle. Wire feeding speed and applied shielding gas will have an effect on the energy distribution and heat input, which can be compensated by the efficiency factor. There are many practical considerations regarding power density distribution in welding which can't be predicted by the model, and a professional welder should be consulted. The welding parameters in this study were set by a professional welder.

The weld thermal cycles for the fusion line (y = 3), the position of minimum hardness (y = 8 mm) and extent of HAZ ($b_{haz}$) (y = 18mm) predicted from the welding parameters used in this thesis are shown in Figure 6-1. Based on the predicted thermal cycle, these results can be used to anticipate the position of minimum hardness in HAZ. This position hasn't experienced temperatures above equilibrium solvus and has spent most time in the "grey zone" interval. The $b_{haz}$ will be located at the position where the peak temperature is under the lower limit of the “grey zone” interval. Temperatures in the “grey zone” interval should be minimized to reduce the deterioration and minimize the $b_{haz}$. This can be achieved by applying high welding moving speed, and a rather high welding effect (Q) to ensure adequate melting. Eurocode 9 indicates $b_{haz}$ = 20 mm if adequate welding has been applied. This is within the limit and hence the applied welding parameters are good.

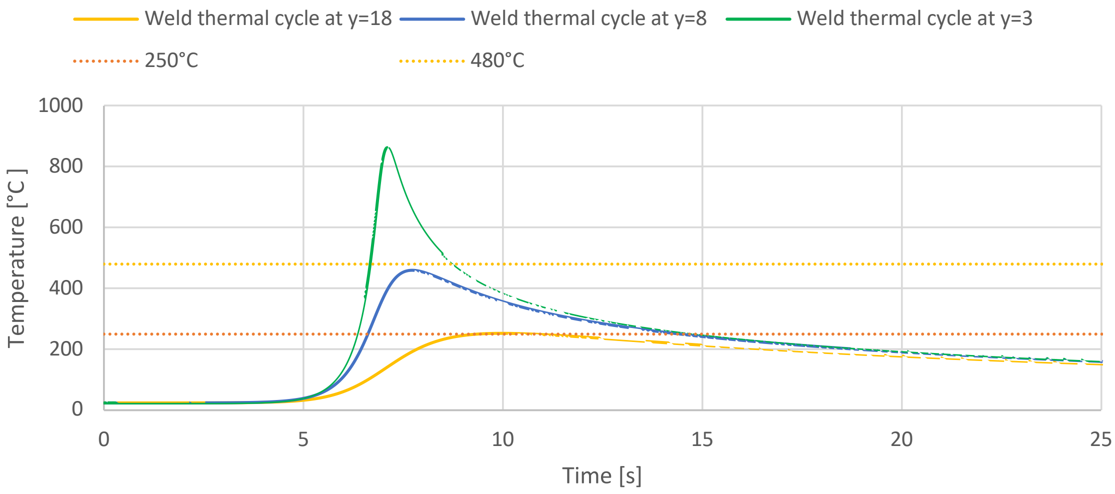

*Figure 6-1: The weld thermal cycles in positions of HAZ extent, minimum*

## 6.2 LASER HEAT DISTRIBUTION TESTING AND MODELLING

The measured temperatures from the heat distribution testing have been analysed by using the heat distribution model. Good predictions by the model have been seen, but model limitation does apply for laser treatment as well. The model doesn't account for latent melting heat. During laser treatment no melting should occur as it wipes out microstructure's thermal history. Hence, the model should work even better for laser treatment under conditions not involving melting. Compared to applying the model for welding, directed metal currents in the weld can also be ignored. The arc energy distribution and laser beam energy have similar influence which should be noticed. The laser energy distribution will be influenced by changing the laser spot diameter. A smaller laser spot size ($\phi$) will be more in accordance with the simplifying assumptions. It should be noted that the predicted temperatures will diverge towards infinity in proximity to the heat source, which does not apply for reality. Hence, the model shows too high values when the distance to the heat source are approaching zero.

However, better predictions by the model has been observed for the thermocouples located further away from the heat source, at 4.16 mm. Thermal cycles measured by the thermocouple (T) located furthest away from the laser beam center line are plotted together with modelled (M) thermal cycles in Figure 6-2. All tested laser moving speeds are presented. The predicted thermal cycles have been optimized with respect to the peak temperature of the measured thermal cycles by adapting the efficiency factor ($\eta$). A study of the efficiency factors used is presented in Chapter 6.2.1. By decreasing the speed, time spent for the thermal cycle in the "grey zone" area is increased. To achieve high peak temperatures, it is beneficial to increase the laser effect. This will increase the peak temperature, but with minor impact on heating and cooling rate.

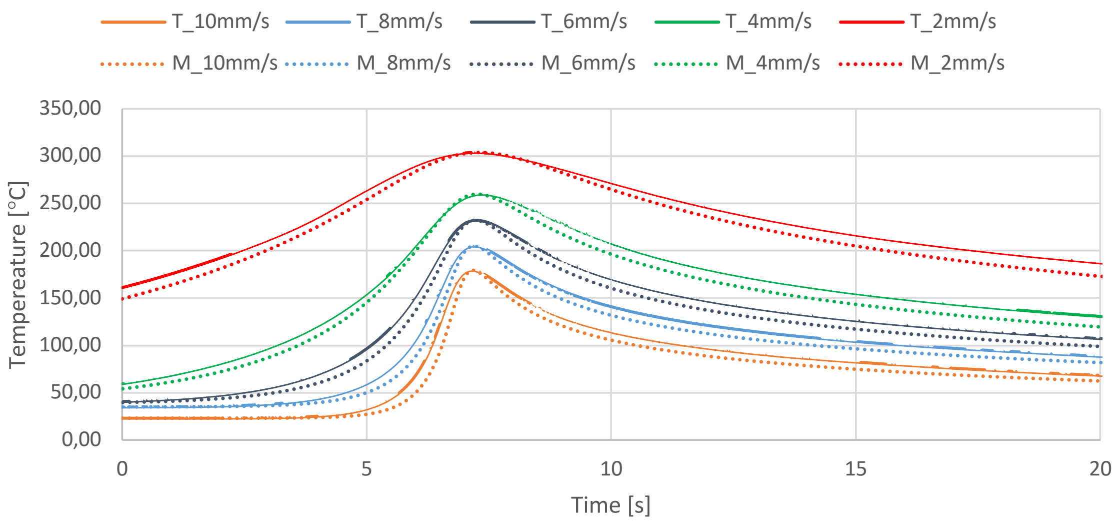

*Figure 6-2: Thermal cycles measured by the thermocouple (T) located 4.16 mm away from the laser beam center and modelled (M) thermal cycles optimized with respect to peak temperature*

### 6.2.1 Efficiency factor

The efficiency factor is used to account for the percentage of the given laser effect absorbed by the material as heat. The efficiency factor was, prior to the heat distribution test, regarded to be dependent on the surface condition. After several runs the efficiency factor anticipated to increase due to reduced reflections from the profile's surface. This has been found to be incorrect as the thermal cycles have been reproduceable with little variation in laser efficiency over several runs. Good reproducibility is positive for industrial application. Three runs have been conducted with $v$ = 10 mm/s. The standard deviation in efficiency factor have variated from 0.002 to 0.004 for the three thermocouples. Two runs were conducted at v = 8 mm/s, where the variation of the efficiency factor was 0 and 0.0004 for the different located thermocouples. $\eta$ have been found to increase with increasing distance from the heat source. This may be a result of the model's limitation and that the predicted peak temperatures are too high in proximity to the heat source. By optimizing the predicted thermal cycles with respect to peak temperature will result in a too low $\eta$, and the predicted heating will be too slow and the predicted heating too fast. All efficiency factors used to optimize the modelled thermal have been plotted versus $v$ in Figure 6-3.

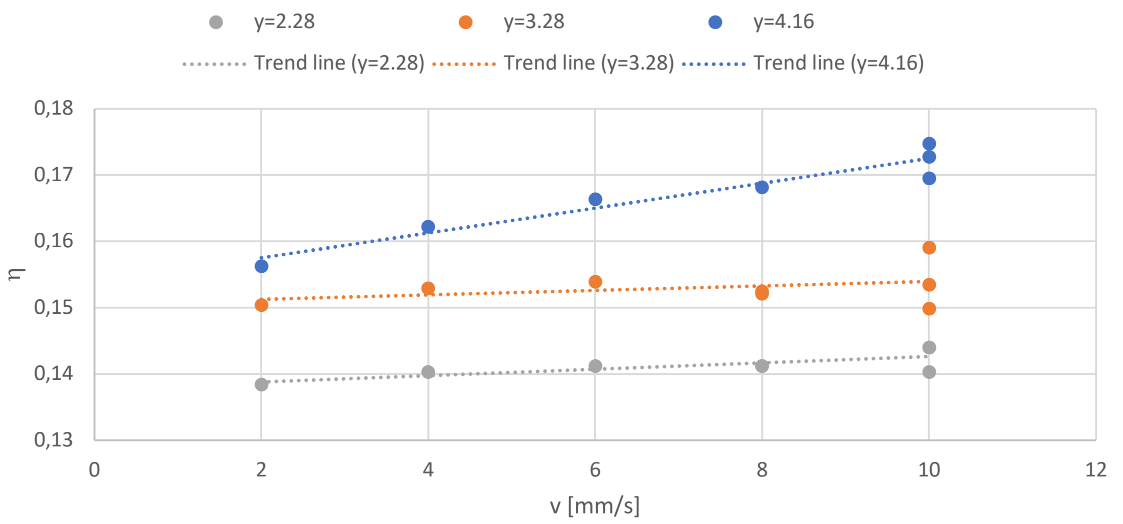

*Figure 6-3: Efficiency factors (η) used to optimize the modelled thermal cycles plotted versus the laser moving speed (v).*

A tendency that $\eta$ increase for increasing $v$ has been observed. The laser efficiency is affected by the absorption properties of the material. Figure 6-4 has been taken from a study on temperature dependency of material absorption in aluminium [43]. The figure shows absorption in aluminium as a function of temperature, and it is decreasing with temperature increased. This is caused by changes in the oxide surface layer. For higher $v$ the heating increase, and the laser is moving faster to an unheated area. This is a reasonable explanation for increase in $\eta$ with higher $v$.

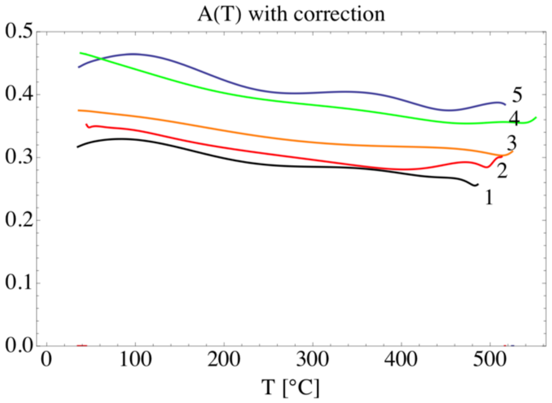

*Figure 6-4: Aluminium sample absorptivity in several heating and cooling cycles up to ~550°C. The increase in absorptivity is evidence for the modification of the aluminium oxide layer [43].*

A sudden increase in laser heating was experienced, during the last run of the laser heat distribution test. This occur when the laser burned through the oxide surface layer in this test. By modelling this event, the efficiency factor is observed to increase when melting occurred. Melting will change the surface conditions considerably, which will also increase the absorption.

## 6.3 LASER TREATMENT PARAMETERS AND EFFECT ON MICROSTRUCTURE

### 6.3.1 Pre-experiment laser treatment

A pre-experiment was conducted to establish a basis for which parameters and pattern to be used for the laser treatment of the welded specimens. These results are not published in this thesis, due to the poor quality. All reference specimens, untreated by laser, fractured in the clamping. Hence, an evaluation could not be made regarding the laser treatment impact on the welded profile. It was observed for those successfully fractured, that the fracture occurred on the side with largest extent of melting. That side where evaluated to have best strength. This observation could be a coincidence. Also, the tensile specimens were cut with free hand machining, this could have influenced location for fracture due to geometry.

### 6.3.2 Thermal cycle of the experimental laser treatment

Increasing the $v$ for the laser treatment of Specimens C and D had a big impact on the melting of the laser treatment pattern. The laser heat input has been too high as the treatment resulted in melting. The used $\phi$ has given too concentrated energy input and should have been increased. High temperatures are desired due to solution treatment but melting have a reducing effect on the material. Increasing the laser spot diameter would give a broader energy distribution, which would have a positive effect; less melting.

The heat distribution model does not apply for the laser treatment applied since the laser movement was conducted in a pattern and not in a straight line. However, predicted heat distribution for the applied laser treatments has been presented in Figure 6-5. By changing the $v$ from 9 mm/s to 9.33 mm/s, a very little temperature decrease has been seen in the model. Nevertheless, the change had a big effect on the laser's melting. Here an efficiency factor of 0,175 has been applied, but it is anticipated to be higher since melting occurred.

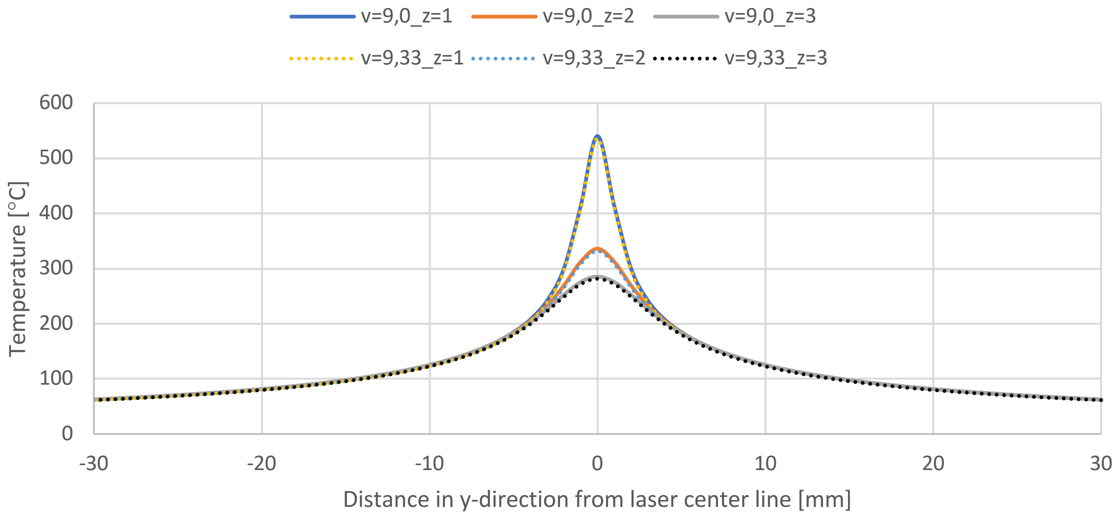

*Figure 6-5: Predicted peak temperature distribution for laser treatments, with both laser parameters applied, in the y-direction from the laser center line at depths; z=1, z=2 and z=3 of the material.*

The laser pattern applied is not optimal in combination with the chosen laser parameters. Some areas of the laser treatment have been influenced negatively by both welding and laser treatment, marked as red circles in Figure 6-6. The parameters need to be adjusted for the specific pattern to avoid negative impact of the laser treatment.

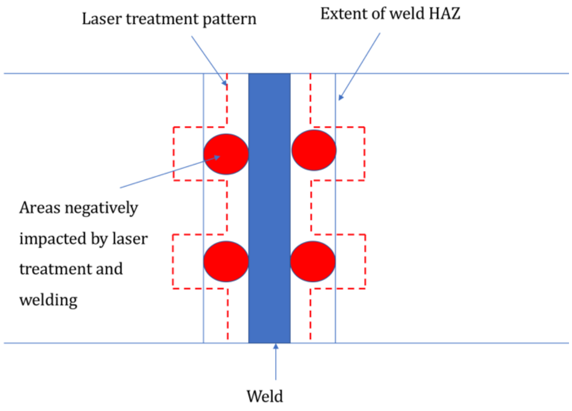

*Figure 6-6: Illustration of areas influenced negatively by welding and laser treatment.*

Compared to the weld thermal cycle, the laser treatment's cooling is rapid, and time spent above 250°C is drastically reduced. This is beneficial with respect to the coarsening of $\beta''$-precipitates. In addition, the area experiencing the temperatures of the "grey zone" will be smaller for the laser treatment compared to the welding. If a laser treatment with temperatures sufficient for solution heat treatment can be achieved with area of $\beta''$-precipitates coarsening of minimized, a method to regain a solution treated microstructure in HAZ may be developed. Kinetics should be further studied for this concept. To achieve rapid heating and cooling with a high peak temperature, high $v$ and $Q$ should be applied. Ideal laser treatment parameters for a 3.6 mm thick plate; $Q$ = 3000 W, $v$ = 12 and spot diameter of 4 mm. The recommended $\phi$ will give a broader laser energy distribution, which will counteract melting. Additional plate cooling may also be beneficial to enable further increase heating and cooling rates of the thermal cycle. Heat will build up during laser treatment. This can be counteracted by applying gradually increasing $v$ or decreasing $Q$ during laser treatment. Hence, a more homogeneous heat treatment of the material is achievable. Changing the parameters during a run is not in compliance with the model.

## 6.4 LASER TREATMENT EFFECT ON MECHANICAL PROPERTIES

Digital image correlation (DIC) instead of an extensometer to measure strain has proven to work well. More information regarding the straining is available with this method. This is especially important when straining components, where different parts of the component are strained differently. Videos of the straining graphically visualized has been especially helpful to evaluate the fracturing.

Due to the softening of the HAZ compared to the base material, referred to as undermatching, fracturing of welded components initiates and remains in this weakened HAZ rather than the base metal (BM). Strain is concentrated to a straight line in HAZ as seen from the DIC results. By applying a laser for post weld heat treatment (PWHT) the HAZ has been modified both metallurgical and mechanical so that the strain is distributed along the laser treatment pattern. Metallurgical the material has been further weakened, especially since the laser caused melting. The concept study conducted by Fjær has predicted a 10 % increase in yield strength from a mechanical design point of view. The mechanical design should be further studied as the optimal design will vary for different component design, like width of the weld and plate thickness for instance. Welding defects, such as micro-cracking and porosity, are easily formed in aluminium welds, which are minimized when using a bigger specimen geometry. The specimen geometry used in for this experiment has worked well, and none fractured in the weld.

The welded specimens in this experiment was not strengthened by laser treatment. Both yield and tensile strength has been reduced for all laser treated specimens. Laser PWHT has many metallurgical aspects needs to be considered. Presence of $\beta''$-precipitates is very important. The hardness measurements indicate that the laser thermal cycle has caused major coarsening for three out of four specimens. Specimen C has experienced an improved hardness profile. This suggest that the laser treatment has solution treated and strengthened the weakest part of HAZ. But as a component the strength has decreased. Form the strain visualisation of Specimen C, it can be observed that a crack is formed in the untreated part of

HAZ. This area would have been further weakened by the laser treatment as explained in chapter 6.3.2.

During and after welding residual stresses developed in the profile which made it distort. In PWHT, softening of the material will occur due to the recovery. This may explain that the yield strength reduced more than the tensile strength for Specimen C and D.

Inhomogeneous nature of both the weld and laser treatment pattern renders for a complex analysis from both metallurgical and mechanical viewpoint. The strength properties were least reduced for Specimen C, but Specimen C did also experience least melting from the laser treatment. Several additional specimens should be tested to give a picture of how pattern geometry influence the stress and strain localization in tensile straining of the specimen.

### 6.4.1 Increase in ductility

Increased plastic straining was observed for Specimens C and D, and the increase can be explained by recovery due to the thermal cycle. Improved ductility is very important in terms of fracture resistance, which also is important for structural components. Toughness is a measurement of the material's resistance to fracture. The toughness of the specimens has been calculated from Equation 2-10 and reported in Table 5-4.

*Table 6-1: Toughness of the specimens*

| | **Ref** | **A** | **B** | **C** | **D** |
|---|---|---|---|---|---|
| **$U_T$** | 5,61 | 2,63 | 5,03 | 6,47 | 7,13 |

During tensile testing all the laser treated specimens developed small cracks which grew into fracture. The untreated specimen fractured immediately after a crack developed in the center of the specimen. The laser treatment has been successful in distributing the strain from a concentrated line in HAZ to a bigger area where it followed the pattern. This has hindered fracture propagation.

## 6.5 FURTHER WORK

Laser treatment is anticipated to give improved behaviour if proper parameters and laser treatment pattern are applied. To demonstrate the idea the following suggestions are given:

The possibility of increasing the minimum hardness without manipulating the HAZ geometry should be tested. Laser treatment alone may give the possibility to give local solution treatment and strengthening of HAZ. Compared to welding, laser treatment has a much more rapid cooling to temperatures under 250°C. Hence, the laser treatment will leave a much smaller deteriorated HAZ. The concept is visualized in Figure 6-9. This method has potential to improve the component's ductility as well make a welded component to withstand more plastic deformation without fracturing.

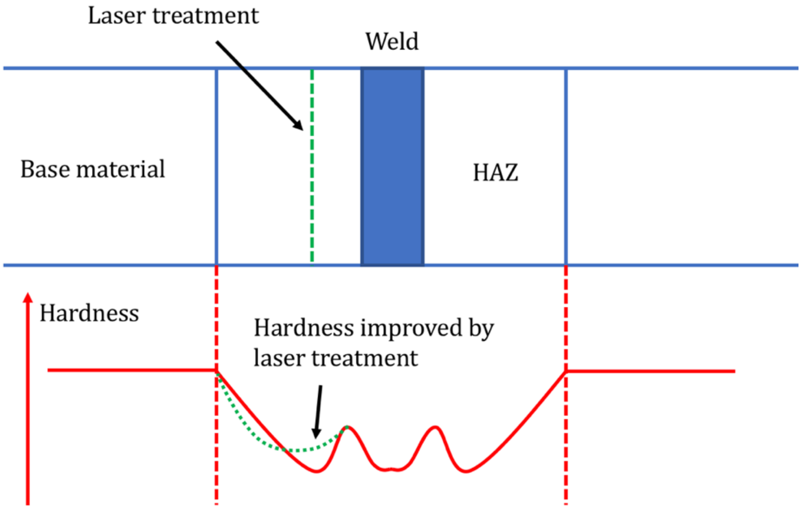

*Figure 6-7: Concept of using the laser for local solution treating to raise the minimum hardness. Laser treatment can be applied to improve the hardness profile.*

Laser treatment with optimized patterns should also be studied. Figure 6-10 shows a suggested laser treatment pattern.

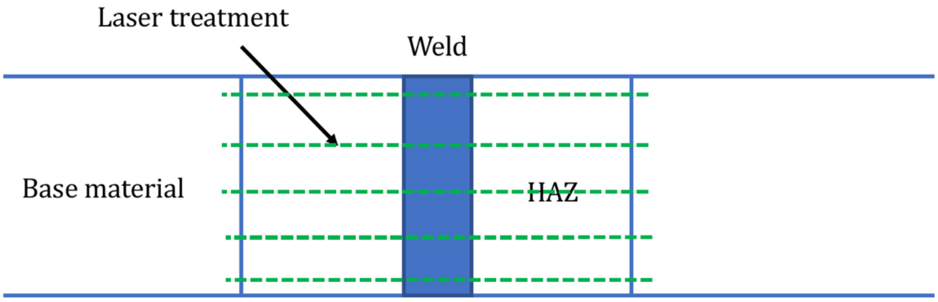

*Figure 6-8: Laser treatment pattern suggestion for further studies.*

# 7 CONCLUSION

The “medium thick plate solution” after Rosenthal [1] has been used to create a heat distribution model for a heat source moving at constant speed. This study has verified that the heat distribution model can be applied for both welding and laser treatment. The results show good predictions for laser thermal cycles measured by thermocouples. A dependency in laser moving speed ($v$) has been seen for $\eta$. Observations indicate that better predictions are made for positions further away from the heat source. Applying $\eta$ in a range between 0.15 and 0.175 gave the best predictions for $v$ between 2 mm/s and 10 mm/s. An increase in $\eta$ was observed if melting occurred. It has been shown that the model can be used to estimate the extent of heat affected zone (HAZ) from the predicted weld thermal cycle.

This study has failed to document the increase predicted by concept study conducted by Fjær. The strength of the specimens treated with laser was reduced compared to an untreated reference specimen. The study has shown that the test where less melting occurred gave most positive results; less strength reduction. It can be concluded that a too high laser heat input was applied which resulted in melting during the laser treatment. Melting has been adversely as it has degraded the weld HAZ further. Anyway, the laser treatment has improved the ductility of the laser treated specimens. The total elongation was increased by more than 50% compared to the Reference specimen when the highest laser speed was applied and minimum melting occurred. The straining before fracture was even more increased, which is an improvement for the fracture resistance of Al-Mg-Si weldments.

The evaluations indicate that a laser heat a laser heat treatment would be positive if adequate laser treatment parameters are applied; e.g. high velocity $v \geq 10$ mm/s and high laser effect. As well a wide laser spot diameter should be applied to avoid melting.

# 8 REFERENCES

[1] D. Rosenthal, The Theory of Moving Sources of Heat and Its Application of Metal Treatments, Transactions of ASME 68 (1946) 849-866.

[2] O. Myhr, Ø. Grong, Process modelling applied to 6082-T6 aluminium weldments—I. Reaction kinetics, Acta Metallurgica et Materialia 39(11) (1991) 2693-2702.

[3] O. Grong, Metallurgical Modelling of Welding, Cambridge: Cambridge University Press1994.

[4] T. Barnes, I. Pashby, Joining techniques for aluminium spaceframes used in automobiles: Part I—solid and liquid phase welding, Journal of materials processing technology 99(1-3) (2000) 62-71.

[5] N. Standard, EN1999-1-1:2007+A2:2013: Eurocode 9: Design of Aluminium structures - Part 1-1: General structural rules., 2007.

[6] H.G. Fjær, Improved strength of a welded aluminium structure by a modification of the HAZ geometry, IFE, Unpublished, 2017.

[7] J.K. Solberg, Teknologiske metaller og legeringer, NTNU, (2010).

[8] R. Lumley, Fundamentals of aluminium metallurgy: production, processing and applications, Elsevier2010.

[9] F. Fadaeifard, K.A. Matori, F. Garavi, M. Al-Falahi, G.V. Sarrigani, Effect of post weld heat treatment on microstructure and mechanical properties of gas tungsten arc welded AA6061-T6 alloy, Transactions of Nonferrous Metals Society of China 26(12) (2016) 3102-3114.

[10] J. Zehnder, R. Pritzlaff, S. Lundberg, B. Gilmont, Aluminium in Transport, Aluminium in Commercial Vehicles (2011) 7-13.

[11] Secrets of the floating tunnel. 2015 (accessed 15.05.2018.2018).

[12] O. Reiso, Extrusion of AlMgSi alloys, Materials Forum, 2004, pp. 32-46.

[13] B. Rinderer, The metallurgy of homogenisation, Materials Science Forum, Trans Tech Publ, 2011, pp. 264-275.

[14] W.D. Callister, D.G. Rethwisch, Materials science and engineering, John Wiley & Sons NY2011.

[15] A. Association, Aluminum: properties and physical metallurgy, ASM International1984.

[16] L. Lodgaard, N. Ryum, Precipitation of dispersoids containing Mn and/or Cr in Al–Mg–Si alloys, Materials Science and Engineering: A 283(1-2) (2000) 144-152.

[17] J. Zhang, Z. Fan, Y. Wang, B. Zhou, Equilibrium pseudobinary Al–Mg2Si phase diagram, Materials science and technology 17(5) (2001) 494-496.

[18] E. Brünger, O. Engler, J. Hirsch, Al-Mg-Si sheet alloys for autobody applications, Virtual fabrication of aluminum products: microstructural modeling in industrial aluminum production. Weinheim: Wiley-VCH Verlag (2006).

[19] G.E. Dieter, D.J. Bacon, Mechanical metallurgy, McGraw-hill New York1986.
[20] H. Vatne, T. Furu, R. Ørsund, E. Nes, Modelling recrystallization after hot deformation of aluminium, Acta materialia 44(11) (1996) 4463-4473.

[21] M. Bru, The Effect of Mn and Homogenisation Procedure on Mechanical Properties and Grain Structure in Extruded AA6082, Institutt for materialteknologi, 2014.

[22] V. Davydov, T. Rostova, V. Zakharov, Y.A. Filatov, V. Yelagin, Scientific principles of making an alloying addition of scandium to aluminium alloys, Materials Science and Engineering: A 280(1) (2000) 30-36.

[23] G. Edwards, K. Stiller, G. Dunlop, M. Couper, The precipitation sequence in Al–Mg–Si alloys, Acta materialia 46(11) (1998) 3893-3904.

[24] C. Marioara, S. Andersen, J. Jansen, H. Zandbergen, Atomic model for GP-zones in a 6082 Al–Mg–Si system, Acta materialia 49(2) (2001) 321-328.

[25] C. Marioara, S. Andersen, H. Zandbergen, R. Holmestad, The influence of alloy composition on precipitates of the Al-Mg-Si system, Metallurgical and Materials Transactions A 36(3) (2005) 691-702.

[26] O.R.a.Ø.G. Myhr, A Combined Precipitation, Yield Strength and Work Hardening Model for Al-Mg-Si Alloys, 11th International Summer School on Aluminium Alloy Technology, NTNU, Trondheim Norway, 2011.

[27] O.R. Myhr, Ø. Grong, K.O. Pedersen, A combined precipitation, yield strength, and work hardening model for Al-Mg-Si alloys, Metallurgical and Materials Transactions A 41(9) (2010) 2276-2289.

[28] G. Mathers, The welding of aluminium and its alloys, Woodhead publishing2002.

[29] O. Myhr, Ø. Grong, H. Fjær, C. Marioara, Modelling of the microstructure and strength evolution in Al–Mg–Si alloys during multistage thermal processing, Acta Materialia 52(17) (2004) 4997-5008.

[30] S. Kou, Welding metallurgy, John Wiley & Sons2003.

[31] O.R. Myhr, Doctoral dissertation: Process mpdelling applied to 6082-T6 aluminium weldments, NTH, 1990.

[32] E. Halmøy, Sveiseteknikk, NTNU, Institutt for produktutvikling og materialer2007.

[33] O. Myhr, Ø. Grong, Process modelling applied to 6082-T6 aluminium weldments—II. Applications of model, Acta Metallurgica et Materialia 39(11) (1991) 2703-2708.

[34] Ø. GRONG, Recent advances in solid-state joining of aluminum, Welding journal 91(1) (2012) 26-33.

[35] T. Udomphol, The weld microstrucutre, Lecture at Suranaree University of Technology, 2007.

[36] J. Hirsch, Virtual fabrication of aluminium products, Wiley-VCH, Weinheim, 2006.

[37] J.K. Holmen, T. Børvik, O.R. Myhr, H.G. Fjær, O.S. Hopperstad, Perforation of welded aluminum components: Microstructure-based modeling and experimental validation, International Journal of Impact Engineering 84 (2015) 96-107.

[38] A. Alisibramulisi, Through Process Modelling of Welded Aluminium Structures, (2013).

[39] B. Nyhus, S. Dumoulin, H. Nordhagen, O.T. Midling, O.R. Myhr, T. Furu, S. Lundberg, Cross-weld tensile strength of aluminum alloys EN AW 5083 and 6082, The 27th International Ocean and Polar Engineering Conference, International Society of Offshore and Polar Engineers, 2017.

[40] O. Myhr, Ø. Grong, Novel modelling approach to optimisation of welding conditions and heat treatment schedules for age hardening Al alloys, Science and Technology of Welding and Joining 14(4) (2009) 321-332.

[41] M. Merklein, W. Böhm, M. Lechner, Tailoring material properties of aluminum by local laser heat treatment, Physics Procedia 39 (2012) 232-239.

[42] M. Geiger, M. Merklein, U. Vogt, Aluminum tailored heat treated blanks, Production Engineering 3(4-5) (2009) 401.

[43] A.M. Rubenchik, S.S. Wu, V.K. Kanz, M.M. LeBlanc, W.H. Lowdermilk, M.D. Rotter, J.R. Stanley, Temperature-dependent 780-nm laser absorption by engineering grade aluminum, titanium, and steel alloy surfaces, Optical Engineering 53(12) (2014) 122506.

# APPENDIX 1:

# MATERIAL CERTIFICATE

This appendix contains one page.

# Hydro Aluminium

Shipped to/destination:
Hydal Aluminium Profiler AS
Raufoss Fabrikkveien
N-2830 RAUFOSS

Sold to:
Hydal Aluminium Profiler AS
Contract /Sales Order no. /Delivery note
70003044 /9347821-1 /82725058
Customer ref.no.
Ikke Homogenisert / Ikke homogenisert
Main carrier:
TRUCK DP 90665 - 350636

## Certificate of Analysis and Weight

Page
1/ 1

Product
Aluminium Extrusion Ingot
Certificate no.
1360513 KARMØY EI
HA Alloy
EI 608250 305mm 6740mm HO
Your spec.
608250

| Heat no. /Act.len | No.of bundles | No.of pieces | Net.weight (Kg) | Piece no. | Analysis in % of weight | | | | | | | | | |
|---|---|---|---|---|---|---|---|---|---|---|---|---|---|---|
| | | | | | Si | Fe | Cu | Mn | Mg | Cr | Zn | Ti | Cd | Al |
| 324305 | 1 | 3 | 3.960 | | 0,99 | 0,20 | 0,01 | 0,54 | 0,66 | 0,01 | 0,00 | 0,02 | 0,00 | 97,56 |
| TOTAL | 1 | 3 | 3.960 | | | | | | | | | | | |
| GROSS WEIGHT | | | 3.972 | | | | | | | | | | | |

Additional info :
NB: This bundle is NOT homogenised

The Al-content in unalloyed material is calculated as the difference between 100% and the sum of all other elements present in amounts of 0.010% or more each.

Marks : Standard marks
1 bundle(s) á 9347821 / 1
Remarks : 1 bundle(s) á 3 piece(s)
Testing according to EN 10204/3.1.B
NB: This bundle is NOT homogenised

Håvik, 21.09.2017

Quality Manager, Karmøy

# APPENDIX 2:

# MOVING LASER HEAT DISTRIBUTION TEST

---

This appendix contains six pages.

# Complete results from the moving laser heat distribution test

## *Q = 2400 W, $\phi$ = 4 mm, v = 10 mm/s*

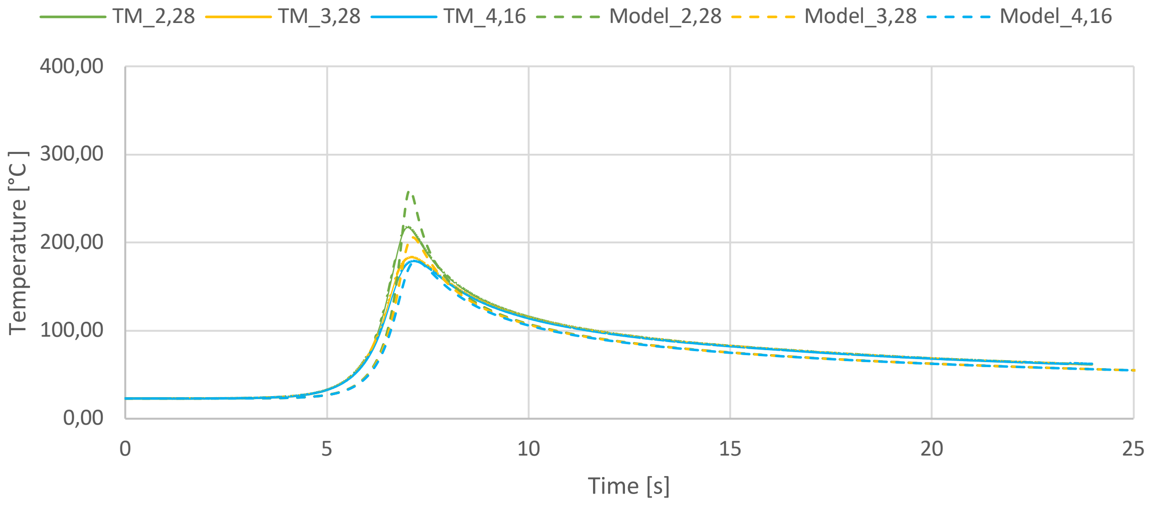

*Figure 1: The measured and modelled thermal cycle of run 1. $\eta$ = 0,1748*

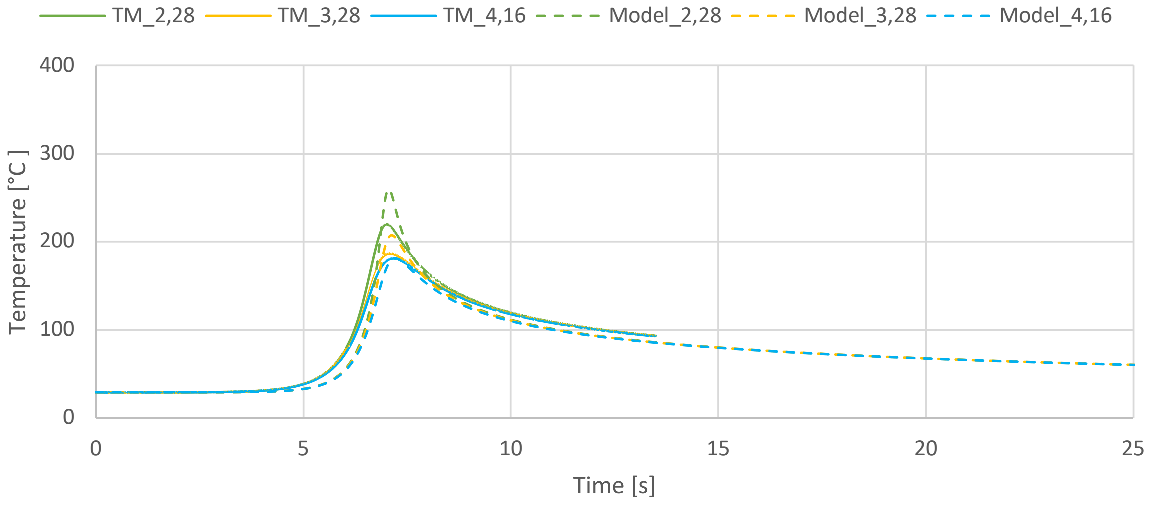

*Figure 2: The measured and modelled thermal cycle of run 2. $\eta$ = 0,1702*

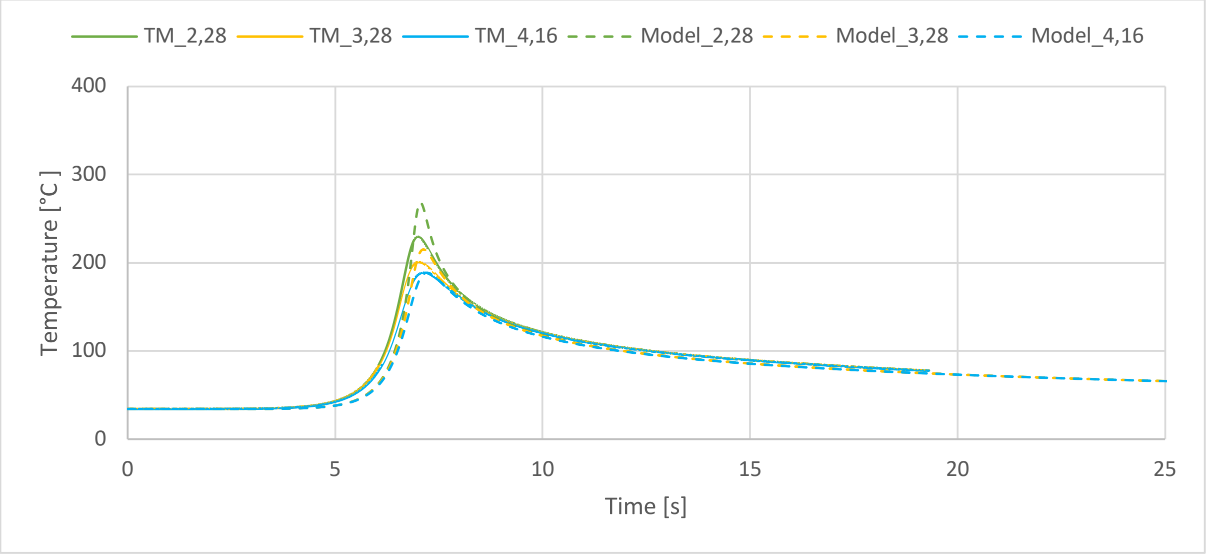

*Figure 3: The measured and modelled thermal cycle of run 8. $\eta = 0{,}1728$*

***$Q = 2400\ W$, $\phi = 4\ mm$, $v = 8\ mm/s$***

The thermocouple at located 4.16 mm from the laser center line was disconnected before the laser started and has been excluded in Figure 4-8.

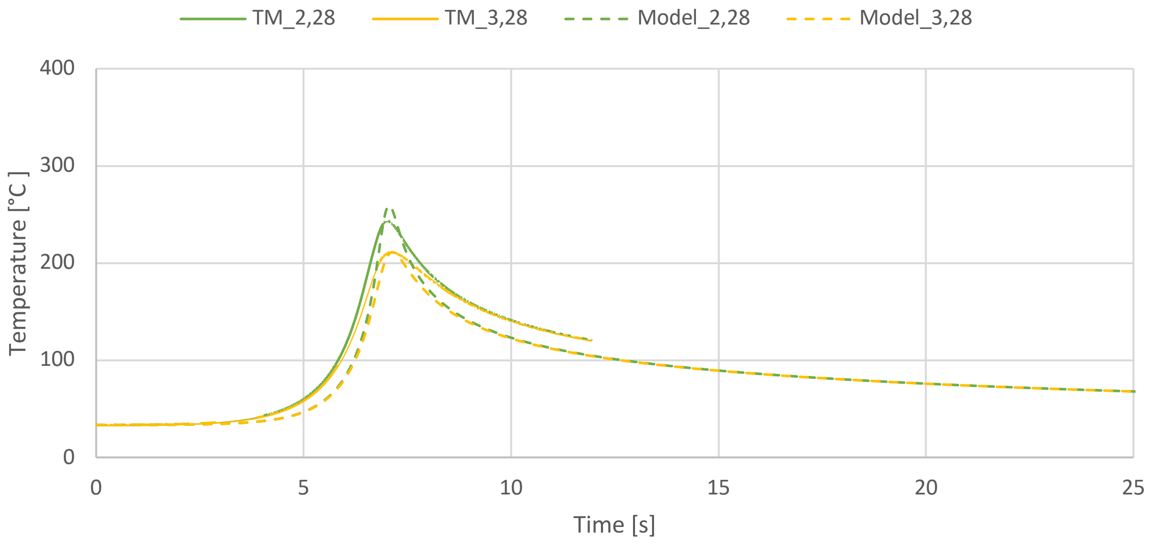

*Figure 4: The measured and modelled thermal cycle of run 3. $\eta = 0{,}1521$*

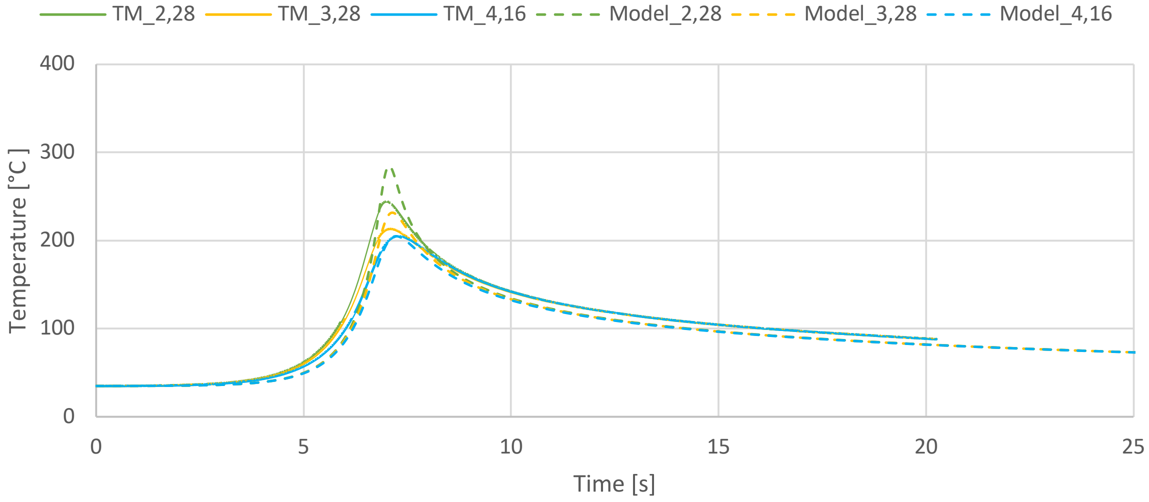

*Figure 5: The measured and modelled thermal cycle of run 4.* $\eta = 0{,}1682$

### $Q = 2400$ W, $\phi = 4$ mm, $v = 6$ mm/s

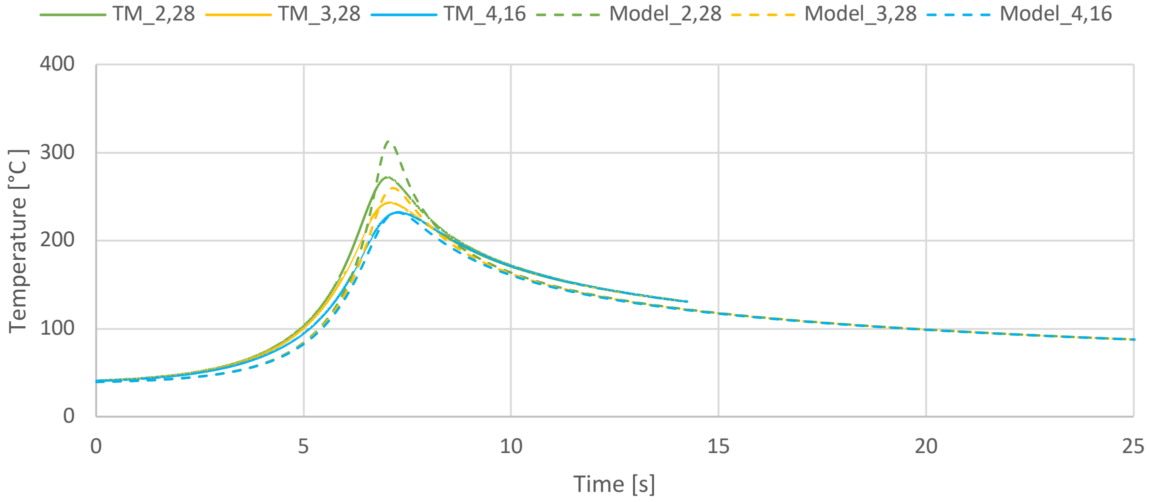

*Figure 6: The measured and modelled thermal cycle of run 5.* $\eta = 0{,}1664$

## *Q = 2400 W, $\phi$ = 4 mm, v = 4 mm/s*

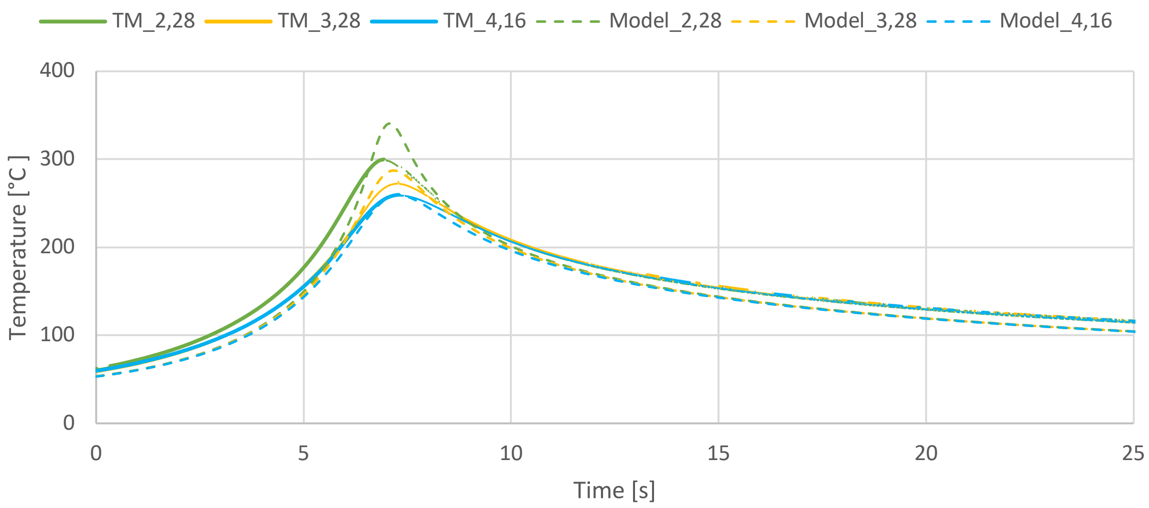

*Figure 7: The measured and modelled thermal cycle of run 6. $\eta$ = 0,1622*

## *Q = 2400 W, $\phi$ = 4 mm, v = 2 mm/s*

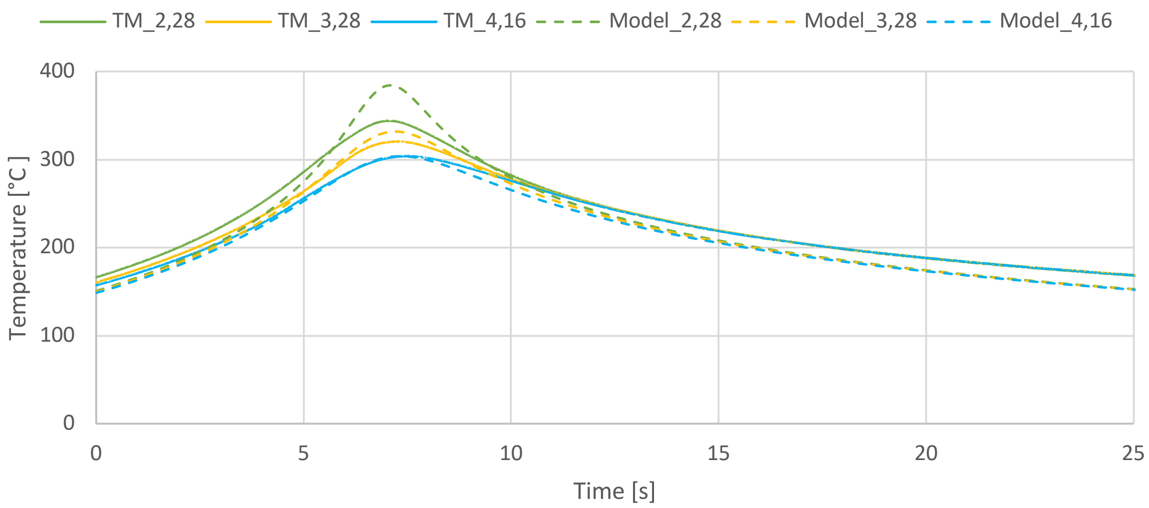

*Figure 8: The measured and modelled thermal cycle of run 7. $\eta$ = 0,1563*

***$Q = 1800$ W, $\phi = 3$ mm, $v = 10$ mm/s***

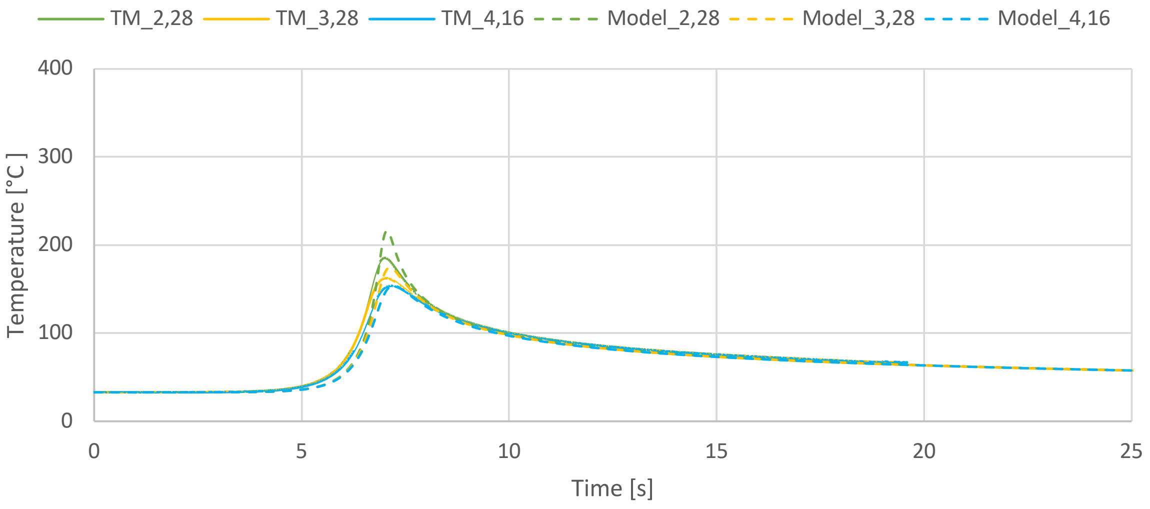

*Figure 9: The measured and modelled thermal cycle of run 9. $\eta = 0{,}1803$*

***$Q = 2400$ W, $\phi = 3$ mm, $v = 10$ mm/s***

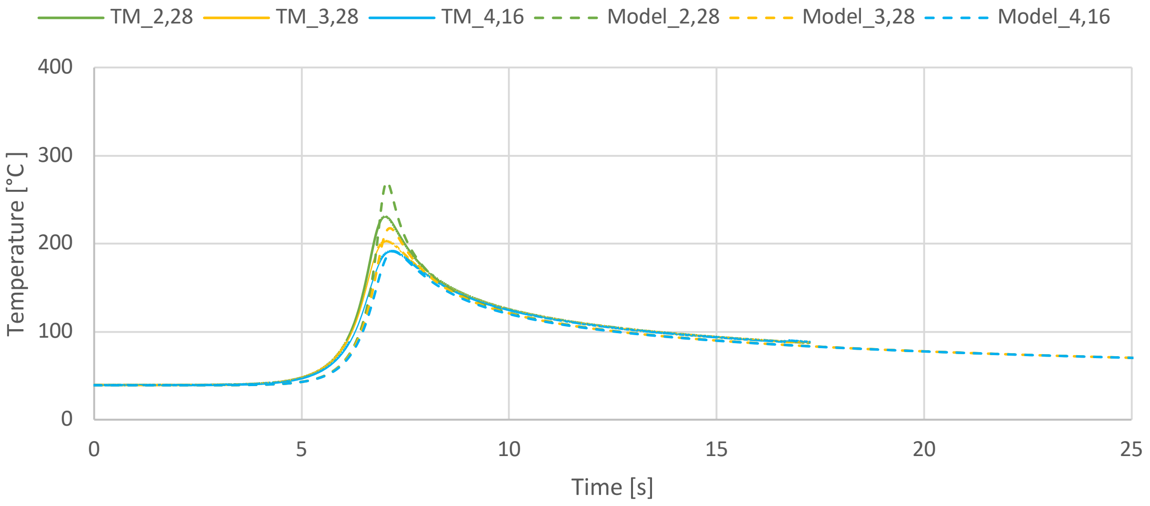

*Figure 10: The measured and modelled thermal cycle of run 10. $\eta = 0{,}1705$*

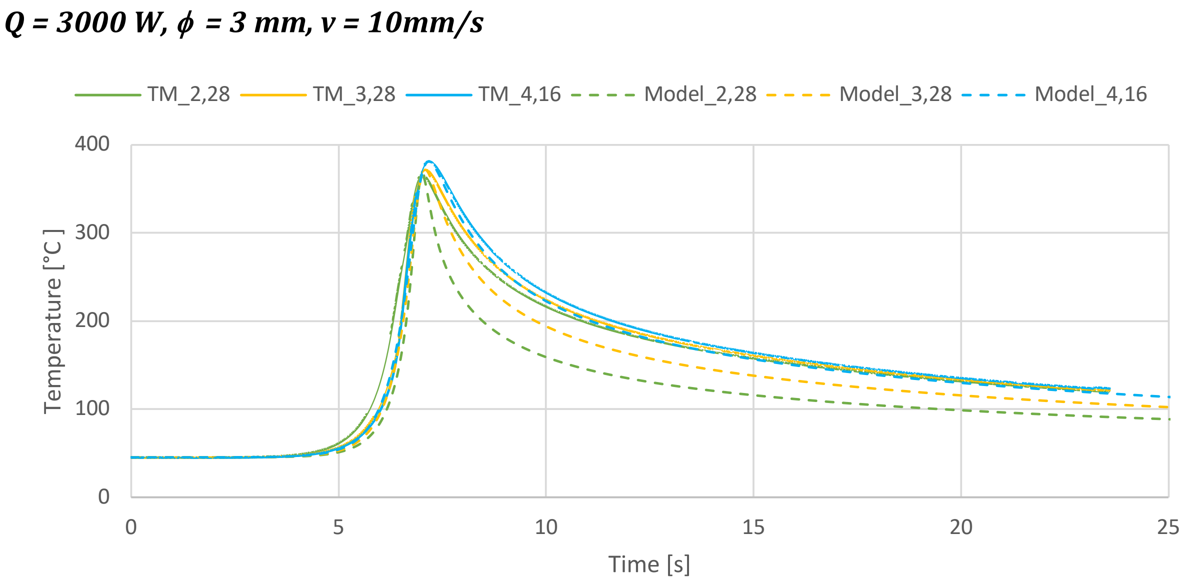

*Figure 11: The measured and modelled thermal cycle of run 11.* $\eta_{2,28} = 0{,}1892$ $\eta_{3,28} = 0{,}2495$ $\eta_{4,16} = 0{,}3005$*. In this run the laser melted through the oxide surface layer and melted the profile.*